

# **Modelling the evolution of small bipolar regions on the Sun**

Dissertation

zur Erlangung des mathematisch-naturwissenschaftlichen Doktorgrades

“Doctor rerum naturalium”

der Georg-August-Universität Göttingen

im Promotionsstudiengang Physik

der Georg-August University School of Science (GAUSS)

vorgelegt von

**Bernhard Hofer**

aus Graz, Österreich

Göttingen, 2022

## Betreuungsausschuss

Dr. Natalie Krivova

Max-Planck-Institut für Sonnensystemforschung, Göttingen, Germany

Prof. Dr. Sami K. Solanki

Max-Planck-Institut für Sonnensystemforschung, Göttingen, Germany

Prof. Dr. Stefan Dreizler

Institut für Astrophysik und Geophysik, Georg-August-Universität Göttingen, Göttingen, Germany

## Mitglieder der Prüfungskommission

Referent: Prof. Dr. Stefan Dreizler

Institut für Astrophysik und Geophysik, Georg-August-Universität Göttingen, Göttingen, Germany

Korreferent: Dr. Natalie Krivova

Max-Planck-Institut für Sonnensystemforschung, Göttingen, Germany

Weitere Mitglieder der Prüfungskommission:

Prof. Dr. Sami K. Solanki

Max-Planck-Institut für Sonnensystemforschung, Göttingen, Germany

Prof. Dr. Ariane Frey

II. Physikalisches Institut, Georg-August-Universität Göttingen, Göttingen, Germany

Prof. Dr. Wolfram Kollatschny

Institut für Astrophysik und Geophysik, Georg-August-Universität Göttingen, Göttingen, Germany

Prof. Dr. Hardi Peter

Max-Planck-Institut für Sonnensystemforschung, Göttingen, Germany

Tag der mündlichen Prüfung: 17.11.2022

© Bernhard Hofer



This work is distributed under a  
Creative Commons Attribution 4.0 License

Printed in Germany



# Contents

<b>Summary</b>	<b>11</b>
<b>Zusammenfassung</b>	<b>13</b>
<b>Abbreviations</b>	<b>15</b>
<b>1 Introduction</b>	<b>17</b>
1.1 Solar influence on Earth	17
1.2 The Sun	19
1.2.1 Solar structure	19
1.2.2 Surface features	21
1.2.3 Measurements of the magnetic field and activity proxies	25
1.2.3.1 Magnetic field measurements	25
1.2.3.2 Other quantities and proxies	27
1.2.4 Emergence patterns of magnetic features and the solar cycle	31
1.3 Generation and surface evolution of the solar magnetic field	34
1.3.1 Magnetic field generation	34
1.3.2 Surface evolution of the magnetic field	36
1.3.3 Modelling and reconstructions of magnetic activity	38
1.3.3.1 Coarse physical model	38
1.3.3.2 Surface flux transport models	39
1.4 Motivation & Outline	40
<b>2 Modelling the evolution of the Sun's open and total magnetic flux</b>	<b>43</b>
2.1 Abstract	43
2.2 Introduction	43
2.3 Data	45
2.4 Model	46
2.4.1 Magnetic flux emergence and evolution	46
2.4.2 Parameters of the model	49
2.5 Reconstruction of the total and open magnetic flux	53
2.6 Summary and discussion	55
<b>3 The influence of small bipolar magnetic regions on basic solar quantities</b>	<b>59</b>
3.1 Abstract	59
3.2 Introduction	60
3.3 Data	62

3.4	Emergence of magnetic regions . . . . .	63
3.4.1	Emergence rate . . . . .	63
3.4.2	Emergence patterns . . . . .	64
3.4.2.1	Emergence latitudes . . . . .	65
3.4.2.2	Tilt angles . . . . .	66
3.4.2.3	Nesting . . . . .	67
3.4.3	Cycle overlap . . . . .	68
3.4.4	Final synthetic input records . . . . .	72
3.5	Model . . . . .	72
3.5.1	Surface flux transport model . . . . .	72
3.5.2	Open flux calculation / CSSS . . . . .	75
3.5.3	Toroidal flux loss calculation . . . . .	75
3.5.4	Simulation setup . . . . .	76
3.6	Results . . . . .	76
3.6.1	Total magnetic flux . . . . .	76
3.6.2	Open magnetic flux . . . . .	78
3.6.3	Polar fields . . . . .	80
3.6.4	Toroidal flux loss . . . . .	81
3.7	Understanding the role of small BMRs . . . . .	82
3.7.1	Total flux . . . . .	82
3.7.2	Polar fields . . . . .	83
3.7.3	Toroidal flux loss . . . . .	85
3.8	Summary and conclusion . . . . .	87
<b>4</b>	<b>Summary &amp; Outlook</b>	<b>91</b>
4.1	Summary . . . . .	91
4.2	Outlook . . . . .	93
	<b>Bibliography</b>	<b>95</b>
	<b>Scientific contributions</b>	<b>117</b>
	<b>Acknowledgements</b>	<b>119</b>
	<b>Curriculum vitae</b>	<b>121</b>

# List of Figures

1.1	Schematic illustration the solar interior and atmosphere. . . . .	20
1.2	Density and temperature profile of the solar atmosphere . . . . .	21
1.3	Solar photospheric features. . . . .	22
1.4	Continuum and magnetogram of an active and ephemeral region . . . . .	24
1.5	Magnetic field measurements . . . . .	26
1.6	Solar irradiance measurements . . . . .	27
1.7	International sunspot number . . . . .	29
1.8	Butterfly diagram and sunspot areas . . . . .	32
1.9	Schematic illustration of the Babcock-Leighton dynamo process . . . . .	35
1.10	Sketch of the effects of surface flows on the magnetic field in surface flux transport simulations . . . . .	36
1.11	Observed differential rotation profile . . . . .	37
2.1	Emergence rate of BMRs from a power-law size distribution . . . . .	48
2.2	Sunspot number and power-law exponent of cycle 21 . . . . .	50
2.3	Evolution of the total magnetic flux (cycles 21-24) . . . . .	52
2.4	Open magnetic flux reconstruction . . . . .	53
3.1	Spatial distribution of emerging BMRs . . . . .	68
3.2	Power-law exponent in the overlap period between cycles . . . . .	71
3.3	Synthetic butterfly diagram . . . . .	73
3.4	Total magnetic flux simulation . . . . .	77
3.5	Open magnetic flux simulation . . . . .	78
3.6	Polar fields simulation . . . . .	80
3.7	Toroidal flux loss simulation . . . . .	81
3.8	Estimate of polar field noise . . . . .	84
3.9	Estimate toroidal flux loss and noise . . . . .	86



# List of Tables

1.1	Magnetic fluxes of bipolar magnetic regions . . . . .	24
2.1	Model parameters . . . . .	51
2.2	Comparison of modelled magnetic fluxes . . . . .	54
3.1	Different BMR populations considered in this work . . . . .	64
3.2	Modelled tilt angles of BMRs . . . . .	67
3.3	Observational constraints of BMR emergence. . . . .	70



# Summary

Solar activity affects life on Earth in various ways, from geomagnetic storms to the terrestrial climate. The driver of solar activity is the solar magnetic field, which manifests itself in the form of small and large-scale magnetic features emerging on the solar surface. The largest features are sunspots. Sunspots are bipolar magnetic regions (BMRs) bearing strong magnetic fields. They form in active regions (ARs) and have been observed since antiquity. Much less is known about the emergence and evolution of small, spotless BMRs. Due to their smaller sizes and weaker magnetic fields, they are difficult to observe. At the same time, due to being much more numerous, they have been proposed to influence the overall magnetic flux budget and the secular variability of the Sun's magnetic flux.

The aim of this thesis is to study the influence of small BMRs on the evolution of the solar magnetic field. Being the longest direct observation of solar activity, models of long-term solar variability typically rely on the sunspot number record. Such sunspot driven models however cannot realistically estimate the amount of small BMRs emerging on the solar surface at low activity. Particularly challenging are extended periods of sunspot absence, such as the Maunder minimum.

We start by developing a new description of emergence rates of the small BMRs in Chap. 2. The model describes the emergence of all BMRs by a single power-law size distribution, in agreement with modern observations. The power-law exponent varies with solar activity, quantified by the sunspot number. With this new description, we ensure that small magnetic regions continue emerging even in the total absence of sunspots. We validate the emergence model by reconstructing the solar magnetic flux since 1610 from the sunspot number with a simple model of the evolution of the global magnetic field quantities, including the total and open magnetic flux, and find good agreement with modern observations and independent reconstructions, including the Maunder minimum.

In Chap. 3, we then employ the proposed description of the BMR emergence to study the influence of small magnetic regions on the solar magnetic field in more detail. We simulate the evolution of the solar magnetic field with a surface flux transport model (SFTM), which allows modelling the evolution and decay of individual BMRs on the solar surface. Since the information on the spatial distribution of small regions is missing in the sunspot records, we derive empirical relationships describing the mean and the scatter of the emergence latitude and tilt angle of all BMRs. The scatter as well as the onset of emergence during the cycle depend on the size of the BMRs. From the sunspot number we then derive semi-synthetic BMR records since 1874, which we use as input to the surface flux transport simulation. We find a good agreement of the calculated magnetic flux, polar fields and toroidal flux loss since 1874 with modern observations and independent reconstructions. Small BMRs have a strong impact on the magnetic flux

during solar minima, comparable to that of large BMRs with sunspots. For the polar field strength and toroidal flux loss, we find that small BMRs are even comparable to the contribution of large BMRs during solar maxima. Due to their high number, small BMRs have a stabilizing effect on the simulation, while most of the noise comes from large BMRs. We also validate and analyse the results of the surface flux transport simulations with an analytical study estimating the influence of small and large BMRs on the solar magnetic field. The analytical results fully support those obtained from the surface flux transport simulation.

Our study highlights the importance of a realistic modelling of small BMRs in historic reconstructions of solar activity, especially during periods of low activity. The latter has important implications for estimates of the secular variability of solar irradiance. The impact of small BMRs on the polar fields and toroidal flux loss are crucial to understand the generation of poloidal magnetic field from the BMRs on the solar surface, which is important for solar dynamo studies.

# Zusammenfassung

Die Sonnenaktivität beeinflusst das Leben auf der Erde in vielfältiger Weise, von geomagnetischen Stürmen bis hin zum Erdklima. Angetrieben wird die Sonnenaktivität vom solaren Magnetfeld, das sich in Form von kleinen und großen magnetischen Strukturen manifestiert, die auf der Sonnenoberfläche entstehen. Die größten dieser Strukturen sind Sonnenflecken. Sonnenflecken sind bipolare magnetische Regionen (BMRs) mit starken Magnetfeldern. Sie bilden sich in aktiven Regionen (ARs) und werden seit der Antike beobachtet. Viel weniger ist über die Entstehung und Entwicklung von kleinen, fleckenlosen BMRs bekannt. Aufgrund ihrer geringeren Größe und schwächeren Magnetfeldern sind sie schwer zu beobachten. Gleichzeitig wurde vorgeschlagen, dass sie aufgrund ihrer viel größeren Anzahl das Gesamtbudget und die säkulare Variabilität des magnetischen Flusses der Sonne beeinflussen.

Das Ziel dieser Arbeit ist es, den Einfluss von kleinen BMRs auf die Entwicklung des solaren Magnetfeldes zu untersuchen. Da es sich um die längste direkte Beobachtung der Sonnenaktivität handelt, stützen sich Modelle, die die langfristige Sonnenvariabilität untersuchen, typischerweise auf Beobachtungen der Sonnenfleckenanzahl. Solche sonnenfleckengetriebenen Modelle können jedoch keine realistische Abschätzung der Anzahl an kleinen BMRs abgeben, die bei geringer Anktivität auf der Sonnenoberfläche entstehen. Besonders herausfordernd sind längere Phasen der Abwesenheit von Sonnenflecken, wie zum Beispiel das Maunder-Minimum.

Daher beginnen wir mit der Entwicklung einer neuen Beschreibung der Entstehungsrate kleiner BMRs in Kap. 2. Das Modell beschreibt die Entstehung aller BMRs durch eine einzige Potenzgesetz-Größenverteilung in Übereinstimmung mit modernen Beobachtungen. Der Exponent des Potenzgesetzes variiert mit der Sonnenaktivität, quantifiziert durch die Sonnenfleckenanzahl. Mit dieser neuen Beschreibung stellen wir sicher, dass auch bei völliger Abwesenheit von Sonnenflecken weiterhin kleine magnetische Regionen entstehen. Wir validieren das Entstehungsmodell, indem wir den magnetischen Fluss seit 1610 aus der Sonnenfleckenanzahl mit einem einfachen Modell der Entwicklung der globalen Magnetfeldgrößen, inklusive des gesamten und offenen magnetischen Flusses, rekonstruieren und finden eine gute Übereinstimmung mit modernen Beobachtungen und unabhängigen Rekonstruktionen.

In Kap. 3, verwenden wir dann die vorgeschlagene Beschreibung der BMR-Entstehung, um den Einfluss kleiner Regionen auf das solare Magnetfeld genauer zu untersuchen. Wir simulieren die Entwicklung des solaren magnetischen Feldes mit einem Oberflächenflustransportmodell (SFTM), das die Modellierung der Entstehung, Entwicklung und des Zerfalls einzelner BMRs auf der Sonnenoberfläche ermöglicht. Da die Informationen über die räumliche Verteilung kleiner Regionen in den Sonnenfleckenzeichnungen fehlen, leiten wir empirische Beziehungen ab, die den Mittelwert und die Streuung des Entste-

hungsbreitengrads und des Neigungswinkels aller BMRs beschreiben. Die Streuung sowie der Beginn des Auftretens während des Zyklus hängen von der Größe der BMRs ab. Aus der Sonnenfleckenanzahl leiten wir dann halbsynthetische BMR-Aufzeichnungen seit 1874 ab, die wir dann als Input für die Oberflächenflusstransportsimulationen verwenden. Wir finden eine gute Übereinstimmung des berechneten magnetischen Flusses, der Polarfelder und der toroidalen Flussverluste seit 1874 mit modernen Beobachtungen und unabhängigen Rekonstruktionen. Kleine BMRs haben einen starken Einfluss auf den magnetischen Fluss während der Sonnenminima, vergleichbar mit dem von großen BMRs mit Sonnenflecken. Für die polare Feldstärke und den toroidalen Flussverlust stellen wir fest, dass kleine BMRs sogar mit dem Beitrag großer BMRs während der Sonnenmaxima vergleichbar sind. Aufgrund ihrer hohen Anzahl wirken sich kleine BMRs stabilisierend auf die Simulation aus, während das meiste Rauschen von großen BMRs kommt. Wir validieren und analysieren auch die Ergebnisse der Oberflächenflusstransportsimulationen mit einer analytischen Studie, die den Einfluss kleiner und großer BMRs auf das solare Magnetfeld abschätzt. Die analytischen Ergebnisse unterstützen vollständig die aus der Oberflächenflusstransportsimulation erhaltenen Ergebnisse.

Unsere Studie unterstreicht die Bedeutung einer realistischen Modellierung kleiner BMRs in historischen Rekonstruktionen der Sonnenaktivität, insbesondere in Zeiten geringer Aktivität. Letzteres hat wichtige Implikationen für Schätzungen der säkularen Variabilität der Sonneneinstrahlung. Der Einfluss kleiner BMRs auf die Polarfelder und den toroidalen Flussverlust sind entscheidend, um die Erzeugung eines poloidalen Magnetfelds von den BMRs auf der Sonnenoberfläche zu verstehen, was für Studien zum Sonnendynamo wichtig ist.

# Abbreviations

<b>ACRIM</b>	Active Cavity Radiometer Irradiance Monitor
<b>AMR</b>	All Magnetic Regions ( $2 \times 10^{20} - 1 \times 10^{23}$ Mx)
<b>AR</b>	Active Region
<b>BMR</b>	Bipolar Magnetic Region
<b>CERN</b>	European Organization for Nuclear Research
<b>CLOUD</b>	Cosmic Leaving Outdoor Droplets
<b>CNO</b>	Carbon-Nitrogen-Oxygen
<b>CME</b>	Coronal Mass Ejection
<b>CSSS</b>	Current Sheet Source Surface model
<b>ER</b>	Ephemeral Region
<b>ESA</b>	European Space Agency
<b>GCR</b>	Galactic Cosmic Ray
<b>GONG</b>	Global Oscillation Network Group
<b>GSN</b>	Group Sunspot Number
<b>H93</b>	<a href="#">Harvey (1993)</a>
<b>HMI</b>	Helioseismic and Magnetic Imager
<b>IN</b>	Internetwork
<b>INTCAL13</b>	$^{14}\text{C}$ data by <a href="#">Reimer et al. (2013)</a>
<b>ISN</b>	International Sunspot Number
<b>ISN2.0</b>	International Sunspot Number, version 2 ( <a href="#">Clette and Lefèvre 2016</a> )
<b>J11</b>	<a href="#">Jiang et al. (2011a)</a>
<b>J20</b>	<a href="#">Jiang (2020)</a>
<b>JAXA</b>	Japan Aerospace Exploration Agency
<b>KPVT</b>	Kitt Peak Vacuum Telescope
<b>LMR</b>	Large Magnetic Regions ( $3 \times 10^{21} - 1 \times 10^{23}$ Mx)
<b>MDI</b>	Michelson Doppler Imager
<b>MWO</b>	Mount Wilson solar Observatory
<b>NASA</b>	National Aeronautics and Space Administration
<b>NSO</b>	National Solar Observatory at Kitt Peak
<b>ODE model</b>	Magnetic flux model by <a href="#">Solanki et al. (2000, 2002)</a> , <a href="#">Vieira and Solanki (2010)</a>
<b>p-p</b>	proton-proton reaction
<b>PFSS</b>	Potential Field Source Surface model
<b>PIKAIA</b>	Genetic fitting algorithm, see <a href="#">Charbonneau (1995)</a>
<b>PMOD</b>	Physikalisch - Meteorologisches Observatorium Davos
<b>RGO</b>	Royal Greenwich Observatory
<b>RGO/SOON</b>	Sunspot group data from RGO and SOON ( <a href="#">Hathaway et al. 2002</a> )

<b>RMIB</b>	Royal Meteorological Institute of Belgium
<b>SATIRE</b>	Spectral And Total Irradiance REconstruction model
<b>SDO</b>	Solar Dynamics Observatory
<b>SEPs</b>	Solar Energetic Particles
<b>SFTM</b>	Surface Flux Transport Model
<b>SILSO</b>	Sunspot Index and Long-term Solar Observations
<b>SMR</b>	Small Magnetic regions ( $2 \times 10^{20} - 3 \times 10^{21}$ Mx)
<b>SN</b>	Sunspot Number
<b>SoHO</b>	Solar and Heliospheric Observatory
<b>SOON</b>	Solar Optical Observing Network
<b>SOT/NFI</b>	Solar Optical Telescope/Narrow-band Filter Imager, onboard Hinode
<b>SSEs</b>	Small-Scale-Emergences
<b>SSI</b>	Spectral Solar Irradiance
<b>TSI</b>	Total Solar Irradiance
<b>VS2010</b>	<a href="#">Vieira and Solanki (2010)</a>
<b>W18</b>	<a href="#">Wu et al. (2018a)</a>
<b>WSN</b>	Wolf Sunspot Number
<b>WSO</b>	Wilcox Solar Observatory

# 1 Introduction

"The Sun is a wondrous body. Like a magnificent father. If only I can be so grossly incandescent."

---

*Solaire of Astora*  
'Dark Souls'

## 1.1 Solar influence on Earth

The Sun is the center of our solar system and the source of the light and energy needed for life on Earth to exist (see e.g. [Kren et al. 2017](#)). As such, the Sun has been revered as a deity by countless cultures throughout the centuries. Early observations of the Sun from ancient China first mention the appearance of dark stains on the solar surface. Millennia later, the invention of the first telescopes in the early 17th century enabled solar observations with for its time unprecedented resolution, confirming that those dark spots were indeed features on the solar surface. They were named sunspots. Astronomers Galileo Galilei and Christoph Scheiner were the first to start systematic observations of the Sun and they began recording the number of sunspots – a record that has been continued up to the present day. Two centuries later, it was discovered that the number of sunspots on the solar surface exhibits a periodicity of approximately 11 years, which was named after the amateur astronomer Samuel Heinrich Schwabe, who published his observations ([Schwabe 1844](#)). In 1801, William Herschel argued on a connection between solar activity and climate on Earth by comparing London wheat prices with the amount of sunspots on the solar surface ([Herschel 1801](#)).

Today we know that the Sun and its activity affects life on Earth in many different ways. On short timescales, eruptive events on the Sun such as flares and coronal mass ejections lead to the ejection and acceleration of highly energetic particles towards Earth's magnetosphere where they can cause beautiful aurorae but also harmful geomagnetic storms (see the review by [Temmer 2021](#)). The latter may lead to severe damage to all kinds of electronic devices by inducing electric currents which can cause failures of power stations and satellites (e.g. [Carrington 1859](#)). Associated radio bursts may further disturb communication systems and the radiation is hazardous for astronauts and aircraft passengers. All these phenomena are caused by the solar magnetic activity.

On longer timescales, solar variability has influence on terrestrial climate (see eg. the review by [Gray et al. 2010](#)). The most direct effect comes in the form of variations in the total (TSI) and spectral solar irradiance (SSI) which are defined as the total

wavelength-integrated and wavelength-resolved solar radiative energy flux that reaches the top of Earth's atmosphere at the mean Sun-Earth distance of one astronomical unit (1AU =  $1.496 \times 10^8$  km). Variations in the solar irradiance can have either extrinsic or intrinsic causes. Extrinsic, the TSI and SSI are modulated by changes in Earth's orbital parameters affecting its precession, obliquity and eccentricity. Those effects have long periodicities of  $\sim 25.000$ ,  $\sim 41.000$  and  $\sim 110.000$  years among others, also known as Milankovich cycles (Paillard 2001, Crucifix et al. 2006) and are thought to be the primary driver of the glacial and interglacial periods throughout Earth's history.

Intrinsic changes of the large scale solar activity show both irregular and periodic variations on timescales from decades to millenia. Cyclic variations besides the 11-year Schwabe cycle and Hale's 22-year magnetic cycle (Babcock 1959, Hale and Nicholson 1925) are the  $\sim 85$  yrs Gleissberg cycle (Gleissberg 1939, Garcia and Mouradian 1998, Feynman and Ruzmaikin 2014, Vázquez et al. 2016, Le Mouél et al. 2017), the  $\sim 210$  yrs Suess (or "de Vries") cycle (Suess 1980, Wagner et al. 2001, Usoskin et al. 2004, Vonmoos et al. 2006, Steinhilber et al. 2012) and various other periodic variations (see eg. the reviews by Hathaway 2015, Usoskin 2017). Sometimes, the Sun falls into a state of greatly lowered activity called a grand solar minimum. During such a grand minimum sunspots almost entirely disappear from the solar surface as has been observed during the Maunder minimum (1645-1715) (Eddy 1976, Sokoloff 2004). Other examples of grand minima include the Spörer minimum (1409 - 1551) and the Wolf minimum (1280-1340). The opposite of grand minima are grand solar maxima, which are periods with unusually high sunspot numbers such as during the grand maxima in the middle ages (1100-1250) and the modern maximum in second half of the 20th century.

It has further been proposed that the terrestrial climate is influenced by solar energetic particles (SEPs) and galactic cosmic rays (GCR). As mentioned earlier, SEPs are released in eruptive events on the solar surface which occur more often at high solar activity. In Earth's atmosphere they lead to ionisation and the destruction of ozone molecules. The GCR flux is anti-correlated to the strength of the solar magnetic field that acts as a shield to our solar system. GCRs also lead to destruction of ozone molecules and the ions produced by them in the Earth's atmosphere have been suggested to form condensation nuclei for cloud formation (Svensmark and Friis-Christensen 1997, Marsh and Svensmark 2000, Svensmark et al. 2016, 2017), although the latter has been subject to criticism and debate (e.g. Pierce and Adams 2009, Calogovic et al. 2010, Kulmala et al. 2010, Laken et al. 2009, 2012, Laken and Čalogović 2013). The Cosmic Leaving Outdoor Droplets (CLOUD) experiments by CERN (European Organization for Nuclear Research), found a possible weak influence of GCRs to cloud formation, although the effect is likely too small to have significant effect on global temperatures (Kirkby et al. 2011, Dunne et al. 2016, Gordon et al. 2017).

Studying the Sun's long-term variations requires historic records of solar activity. However, high precision space-based measurements of the solar magnetic field only exist since 1974 (see Sect. 1.2.3.1). Space-based observatories are also the only way to directly measure solar irradiance, because the terrestrial atmosphere absorbs part of the radiation before it reaches the ground. Therefore, the only way to estimate historic solar activity is by the means of proxies such as the sunspot number or abundances of cosmogenic isotopes (Sect. 1.2.3.2). A multitude of models have been developed to reconstruct historic solar activity (Sect. 1.3.3). However, as will be shown in Chap. 2 and 3, many uncertain-

ties remain that call for further improvements to advance our understanding of the Sun and its influence on Earth. We summarize our results and discuss future applications in Chap 4.

## 1.2 The Sun

The Sun is the star in the center of our solar system. It is a middle aged (4.6 Gyrs) main-sequence star of spectral type G2V with a surface temperature of  $T_{\odot} = 5778$  K and a luminosity (that is the total radiated power from the entire surface) of  $L_{\odot} = 3.8 \times 10^{26}$  W. At  $M_{\odot} = 2 \times 10^{30}$  kg it holds 99.86% of the total mass of the solar system and its radius of  $R_{\odot} = 696$  Mm is 110-times larger than that of Earth, (see also the review by [Christensen-Dalsgaard 2021](#)). It consists of mainly hydrogen ( $\sim 75\%$ ) and helium ( $\sim 24\%$ ) while heavier elements make up the remaining  $\sim 1\%$  ([Anders and Grevesse 1989](#), [Grevesse and Sauval 1998](#), [Lodders 2003](#), [Asplund et al. 2009](#), [2021](#)).

### 1.2.1 Solar structure

The Sun can be divided into several layers, each with its own distinct physical conditions; see Fig. 1.1. At the very center is the solar core. Although its radius is only  $0.2-0.25R_{\odot}$ , it contains about half of the entire solar mass. This leads to very high pressure ( $150$  g/cm<sup>3</sup>) and temperature ( $1.57 \times 10^7$  K), enough to enable nuclear fusion. More than 99% of the energy in the solar core is generated from the proton-proton (p-p) reaction, while the remaining  $\sim 1\%$  come mostly from the Carbon-Nitrogen-Oxygen (CNO) cycle ([Adelberger et al. 2011](#), [Agostini et al. 2020](#)) Above the core is the radiation zone ( $< 0.7R_{\odot}$ ) where the energy from the core travels outward through thermal radiation. The temperature drops from  $7$  to  $2 \times 10^6$  K and the pressure from  $20$  to  $0.2$  g/cm<sup>3</sup> within the layer. From  $> 0.7R_{\odot}$  onward to the solar surface the plasma has cooled so much that radiative transport becomes inefficient and energy is transported by convective plasma motions, thus this layer is called the convection zone. Between the radiative and the convection zones at  $0.7R_{\odot}$  is the tachocline, a thin transition layer where the rigid rotation of the radiative zone meets the differential rotation (faster rotation at the equator than at the poles) of the convective zone. This results in a large shear in the tachocline that has been speculated to be origin of the solar magnetic field; see Sect. 1.3.1.

The solar atmosphere can be divided into the photosphere, the chromosphere, a thin transition layer and the corona. Both density and temperature vary greatly throughout the atmosphere, shown in Fig. 1.2. The photosphere is the visible surface of the Sun. This corresponds to an optical depth of  $\tau_{5000} = 2/3$  for green light ( $5000$  Å), which means that the plasma is opaque in visible wavelengths. The temperature at the surface is  $5778$  K and decreases to a minimum of about  $4000$  K at a height of  $500$  km. The density decreases to  $3 \times 10^{-7}$  g/cm<sup>3</sup> – four orders of magnitude lower than the atmospheric pressure on Earth. In the photosphere a multitude of physical phenomena can be observed, such as granulation and supergranulation cells caused by the convective plasma motions, the emergence of sunspots and other magnetic features. We will take a closer look at those phenomena in Sect. 1.2.2. In the lower and middle chromosphere, the density further decreases while the temperature slowly rises. Then in the thin transition layer and the upper chromo-

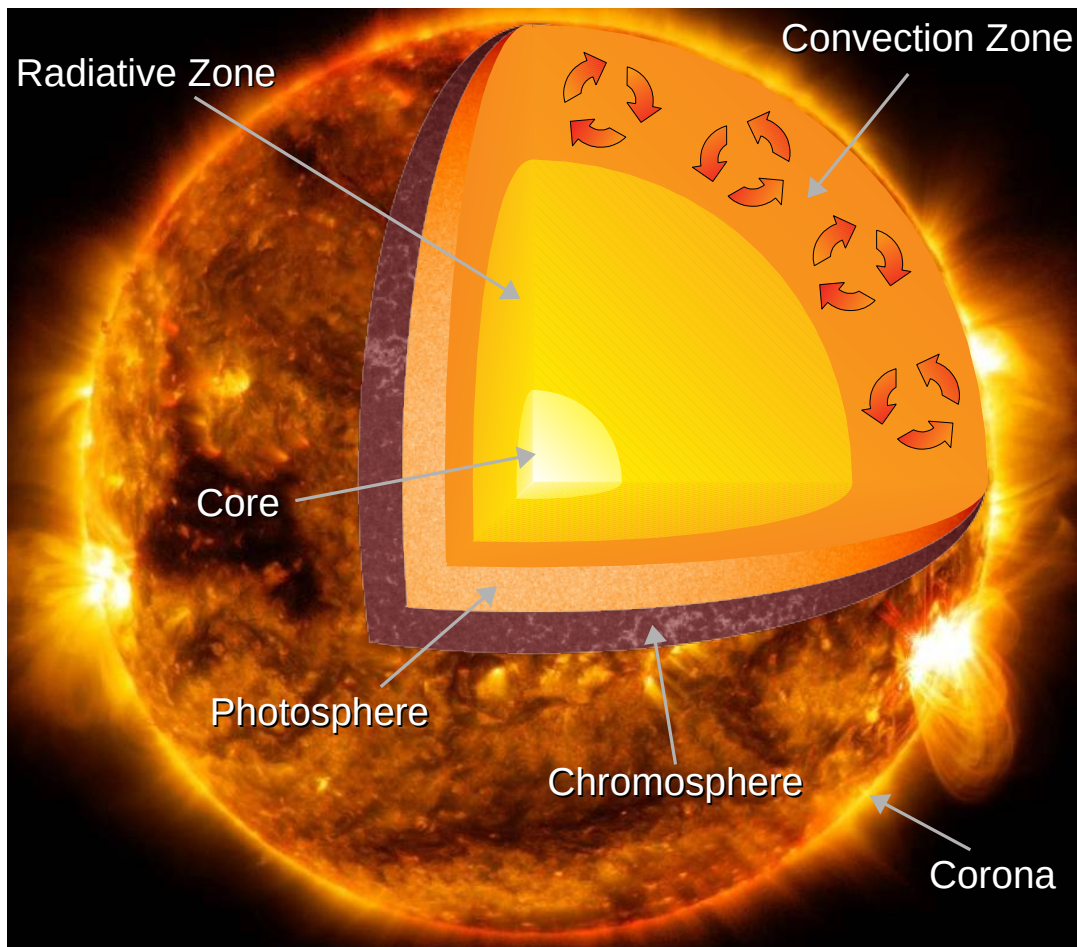


Figure 1.1: Schematic illustration of the solar interior and atmosphere. From the inside outwards: The solar core, radiative zone, convection zone, photosphere, chromosphere and corona. See main text for details. The images are courtesy of NASA and taken from [www.nasa.gov](http://www.nasa.gov) (corona), [svs.gsfc.nasa.gov](http://svs.gsfc.nasa.gov) (photosphere) and [helioviewer.org](http://helioviewer.org) (chromosphere)

sphere, the temperature rises abruptly to several million Kelvin while the density drops to only  $10^{10}$  particles per cubic centimetre. The cause for the extremely high coronal temperatures is one of the most discussed "hot" topics in solar physics. Possible heating mechanisms include "nanoflares" (small-scale reconnection events of braided field lines, [Parker 1972, 1983](#)) or magnetohydrodynamic waves (dissipation of Alfvén waves, [van Ballegoijen et al. 2011](#)). For a review of coronal heating models see e.g. [De Moortel and Browning \(2015\)](#), [Pontin and Hornig \(2020\)](#), [Van Doorselaere et al. \(2020\)](#). Due to the low plasma density in the corona, its evolution is dominated by strong magnetic fields. The corona stretches for several solar radii and dynamically transitions into the solar wind, a continuous stream of charged particles ejected from the solar corona into the interplanetary space. Finally, the heliosphere is the outermost range of influence of the Sun, in which the solar wind and the magnetosphere reach out for more than 120 AU (the heliopause). The solar magnetosphere acts as a shield that protects Earth from GCRs and highly energetic interstellar particles.

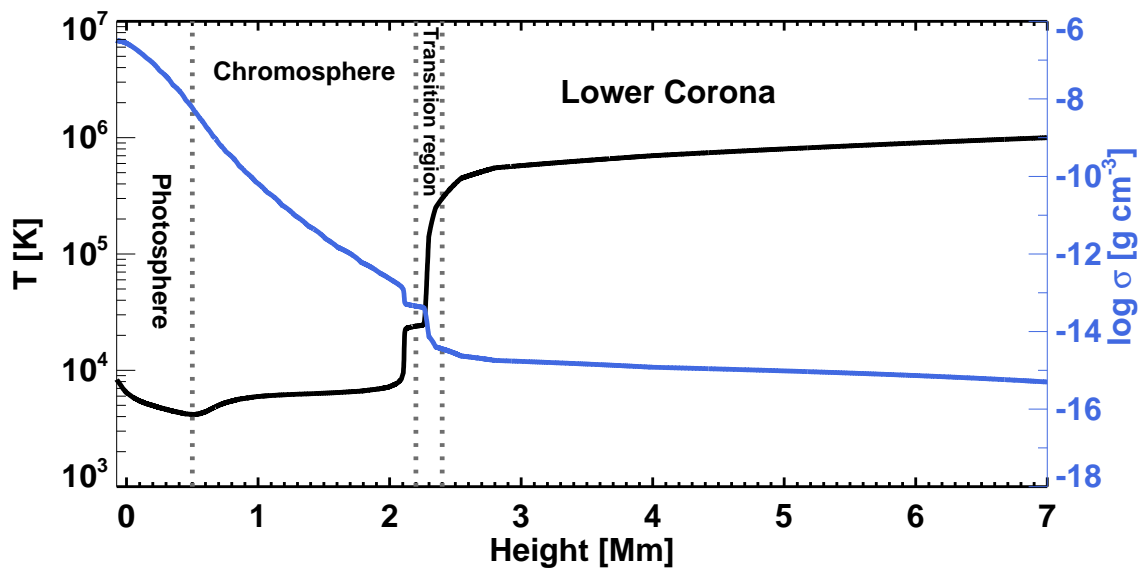


Figure 1.2: The one dimensional temperature (black) and density (blue) profiles in the solar atmosphere depending on their height above the solar surface. The profiles are reproduced from the data from [Vernazza et al. \(1981\)](#).

### 1.2.2 Surface features

The surface of the Sun is not homogeneous. Even with the naked eye ancient civilizations were able to see spots on the solar surface. Later, observations with telescopes revealed that sunspots are not the only features that form on the solar disc and even more features were discovered as the resolution and instrumentation of observatories improved. These various surface phenomena vary greatly in size, shape and lifetime, shaping the inhomogeneous, ever-changing face of the Sun. In this section we briefly describe the most prominent structures observed on the solar surface. For this, we categorize the solar surface into three different classes: The part of the solar surface that is free of or only features weak magnetic fields is called the *quiet Sun*. Regions with strong magnetic fields are called *active regions*. Their smaller counterparts are known as *ephemeral regions*.

- *Quiet Sun*: The quiet Sun is the solar surface which is free of measurable magnetic fields. Due to the convective plasma flows from the solar interior, most of the quiet Sun's surface is covered by convective cells called granules. They appear brighter at the center where the hot plasma rises from the convection zone and darker at the edges where the cooled down plasma descends, see Fig. 1.3. Granular cells evolve dynamically on timescales of just several minutes and range in diameter between hundreds and thousands of kilometers. Doppler velocity measurements revealed another large scale flow pattern called supergranulation which consists of cells with 30 – 35 Mm diameter and evolves on timescales of 1-2 days (see also [Rincon and Rieutord 2018](#)). Most of the observable magnetic elements in the quiet Sun are concentrated in the downflow areas of granular and supergranular cells forming the so-called magnetic network.

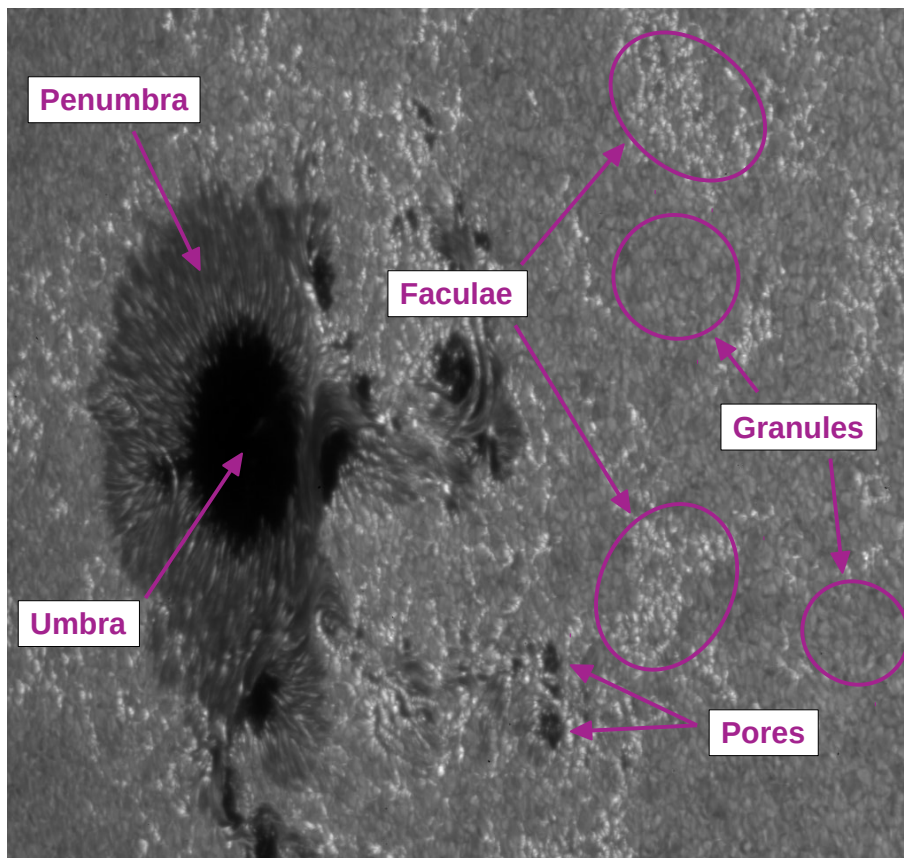


Figure 1.3: High resolution image of the solar surface with several magnetic features including a sunspot by the optical telescope on board the Hinode spacecraft. Courtesy of JAXA/ESA (adapted)

- *Active regions:* The most prominent solar surface features are sunspots that form in regions with very strong magnetic fields called active regions (ARs). They emerge within the so-called "active belts" located at high latitudes ( $25 - 35^\circ$ ) at the start of a solar cycle, but migrate closer towards the equator ( $5 - 10^\circ$ ) throughout the duration of the solar cycle (see Sect. 1.2.4). ARs form as a result of the solar dynamo process described in Sect. 1.3.1, by magnetic flux tubes rising from the bottom of the convection zone until they penetrate the solar surface in an  $\Omega$ -like shape, where they form bipolar magnetic regions (BMRs) (Parker 1979). The preceding polarity is usually more compact than the following polarity which tends to be more diffuse and is often split up into smaller polarity patches (Bray and Loughhead 1979, McIntosh 1981). The magnetic fields in the footpoints of ARs are so strong ( $\approx 2000 - 4000$  G, Livingston 2002), that they inhibit the convective plasma flows, leading to cooling and the resulting darkening of the plasma at the solar surface, observed as sunspots. Sunspots themselves can be further separated into umbra and penumbra, see Fig. 1.3. Umbra is the dark center of the sunspot where the magnetic fields penetrate the surface almost vertically. Umbrae have typical surface temperatures of  $\sim 4300$  K compared to the typical solar surface temperature of  $\sim 5800$  K and their brightness is about 10 – 30% of the quiet Sun (Solanki 2003, Mathew et al. 2007). The dark umbra is surrounded by a brighter region (65 – 85% of the

quiet Sun) that is called penumbra. Here the magnetic fields have a more horizontal orientation and are not quite as strong as in the umbra (1000 – 2000 G) and the typical temperatures are  $\sim 5400$  K (Solanki 2003). Fully developed sunspots have typical diameters of up to 50 – 60 Mm, magnetic fluxes  $> 5 \times 10^{21}$  Mx and lifetimes between days and weeks (van Driel-Gesztelyi and Green 2015). Some magnetic fields are not strong enough to develop into full bipolar sunspots, but are observed as smaller dark regions called pores that feature only an umbra and have sizes of a few hundred to a few thousand kilometers.

Weaker magnetic fields form bolometrically bright features called faculae. They are observed as ensembles of bright but small (tens to hundreds of kilometers diameter) magnetic features which tend to form in the proximity of sunspots and cover large areas of several tens of Mm. When observed in the chromosphere (e.g. in the Ca II K line) they are seen as extended bright regions called plage. Areas with faculae are typically observed for several weeks although the individual features disappear within minutes to hours. The reason for faculae being brighter than the surrounding plasma lies in their smaller diameter. While the bottom of the flux tube appears dark, due to the inhibition of convective plasma flows, the walls experience radiative heating by the surrounding plasma ("hot wall" effect, see e.g. Spruit 1976, Zwaan 1978). As the faculae are not large enough to inhibit the convection (as is the case for the dark pores and sunspots) the inflowing energy heats up the walls so that they appear bright, which can best be observed near the solar limb (Carlsson et al. 2004, Keller et al. 2004). It is believed that the transition between bright and dark features lies between 400 – 700 km in diameter (Knoelker and Schuessler 1988, Grossmann-Doerth et al. 1994).

- *Ephemeral regions*: Besides the large-scale ARs, a huge number of small-scale BMRs constantly emerge all over the solar surface. Due to their typically short lifetimes of hours up to a day, they are called ephemeral regions (ERs). ERs are too small in size and magnetic flux to form sunspots or pores, but they can be observed in magnetograms, see Fig. 1.4. The properties of ERs have been studied in detail by (Harvey 1993, H93), who found typical sizes between a few and up to  $\sim 20$  Mm and magnetic fluxes between  $3 \times 10^{18}$  to a few times  $10^{20}$  Mx, although the lower flux limit was attributed to the resolution limit of the available data. The number of emerging regions is however orders of magnitude higher than that of ARs, so that they have an important contribution to the solar magnetic flux budget (e.g. Thornton and Parnell 2011). Although the spatial distribution and orientation of the smallest ERs are almost random, H93 found that there is a smooth transition between the emergence patterns of large ERs and small ARs concluding that ERs are actually the small-scale end of ARs, see also Sect. 1.2.4. From observations we know that the cyclic emergence of ERs is more extended in time than that of ARs, overlapping several years with neighboring solar cycles (see e.g. Legrand and Simon 1981, Wilson et al. 1988, H93, Tlatov et al. 2010, Hathaway 2015 and references therein). The number of ERs thereby varies much less than that of ARs between high and low solar activity (e.g. H93, Thornton and Parnell 2011). This makes ERs especially important for the secular variability of the solar magnetic field (Solanki et al. 2000, 2002) and solar irradiance (Krivova et al. 2007).

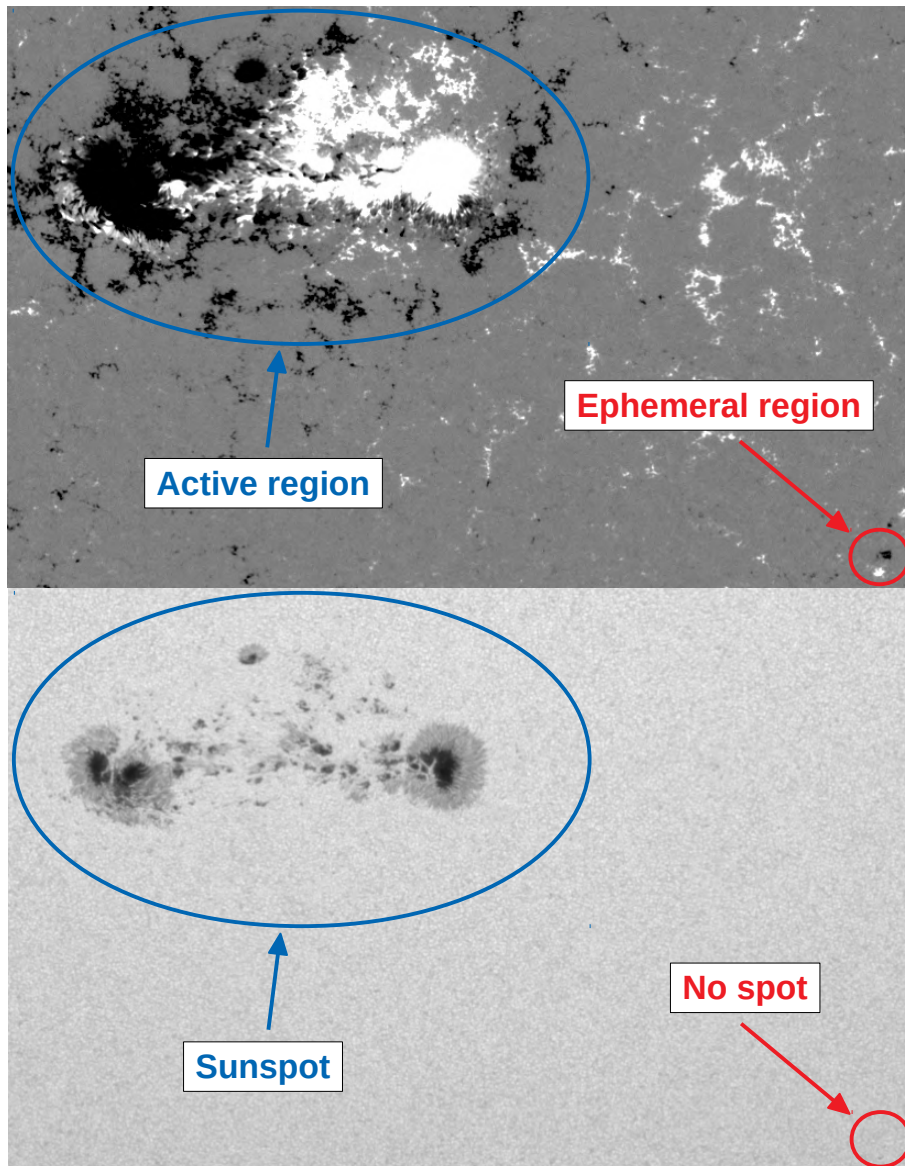


Figure 1.4: Picture of an AR and an ER in a magnetogram (top) and a continuum image (bottom). The AR is much larger and harbours a sunspot, whereas the ER is only visible in the magnetogram. Adapted from [www.helioviewer.org](http://www.helioviewer.org) (SDO/HMI data).

The magnetic flux limit between ARs and ERs is only loosely defined and varies from study to study. Therefore, in Tab. 1.1 we summarize our definition ARs and ERs that we use throughout the thesis. For more details how we derive the magnetic flux limits see Sects. 2.4.2 and 3.4.1.

Table 1.1: Magnetic flux content of BMRs as used in this study.

Magnetic feature	Magnetic flux range [Mx]
ARs (with sunspots)	$3 \times 10^{21} - 1 \times 10^{23}$
ARs (only pores)	$4 \times 10^{20} - 3 \times 10^{21}$
ERs (no spots at all)	$3 \times 10^{18} - 4 \times 10^{20}$

### 1.2.3 Measurements of the magnetic field and activity proxies

The magnetic field produced in the interior and emerged through the solar surface into the atmosphere has numerous partly spectacular manifestations. We have already mentioned sunspots, faculae and ERs in Sect. 1.2.2. There are also coronal loops and eruptive phenomena such as coronal mass ejections and flares, that can cause geomagnetic disturbances in the terrestrial atmosphere (e.g. Sect. 1.1). The various observables on the Sun can be used to describe solar magnetic activity and are called indices and proxies of solar activity. In this Section, we will present several of those solar indices and proxies that are directly relevant to our work. However, we stress that this is by no means a complete list of all the known quantities related to solar activity.

Some quantities can be measured directly through a real physical observable (e.g. the total and open magnetic flux, see Sect. 1.2.3.1). Such "physical" indices can be used to directly quantify solar magnetic activity and its physical effects. Although not a measurement of the solar magnetic field itself, the total solar irradiance is another directly measurable quantity that is strongly related to the solar magnetic field (see Sect. 1.2.3.2). This is due to the different bolometric brightness of the various magnetic features on the solar surface. However, direct measurements of the magnetic field and solar irradiance exist only since a few decades. On longer timescales (up to centuries or millennia) one needs to rely on proxies of solar activity, see Sect. 1.2.3.2. The longest running direct proxy of solar activity is the sunspot number that has been recorded since the early 17th century. To quantify solar activity on timescales of millennia, the only option is to use indirect proxies such as concentrations of cosmogenic isotopes stored in natural archives. Although isotope records have a higher uncertainty and lower temporal resolution (mostly decadal) than sunspot records (daily, monthly or annual), they can be used to study the long-term trends in solar activity (see e.g. the review by Usoskin 2017), which is useful for example for climate studies.

Solar activity and its various manifestations are not constant, but show periodic and non-periodic variations on various timescales. The most prominent variation is the 11-year sunspot cycle (Schwabe 1844) whose most evident manifestation is a cyclic variation in the number and spatial distribution of the magnetic features on the solar surface (Sect. 1.2.2). The evolution and the distribution of those magnetic features throughout the solar cycle are described in the next section (Sect. 1.2.4).

#### 1.2.3.1 Magnetic field measurements

Solar variability on timescales longer than a day is driven mainly by its magnetic field. A straightforward way to quantify the global solar magnetic field is the unsigned solar total magnetic flux derived from synoptic maps of the line-of-sight photospheric magnetic field. Synoptic maps are created by combining individual magnetograms taken throughout one Carrington rotation, which is the mean rotation period of the solar surface at low latitudes (27,2753 days, by Richard Carrington). The calculated total magnetic flux varies between observatories, due to e.g. magnetograph saturation (Svalgaard et al. 1978), observation in different wavelengths or different spatial resolution of the instruments (for an overview see e.g. Riley et al. 2014). The longest running full-disc magnetographic measurements are made by ground-based observatories: Wilcox Solar Observatory (WSO, since 1976), Mount Wilson solar Observatory (MWO, since 1967) and National Solar

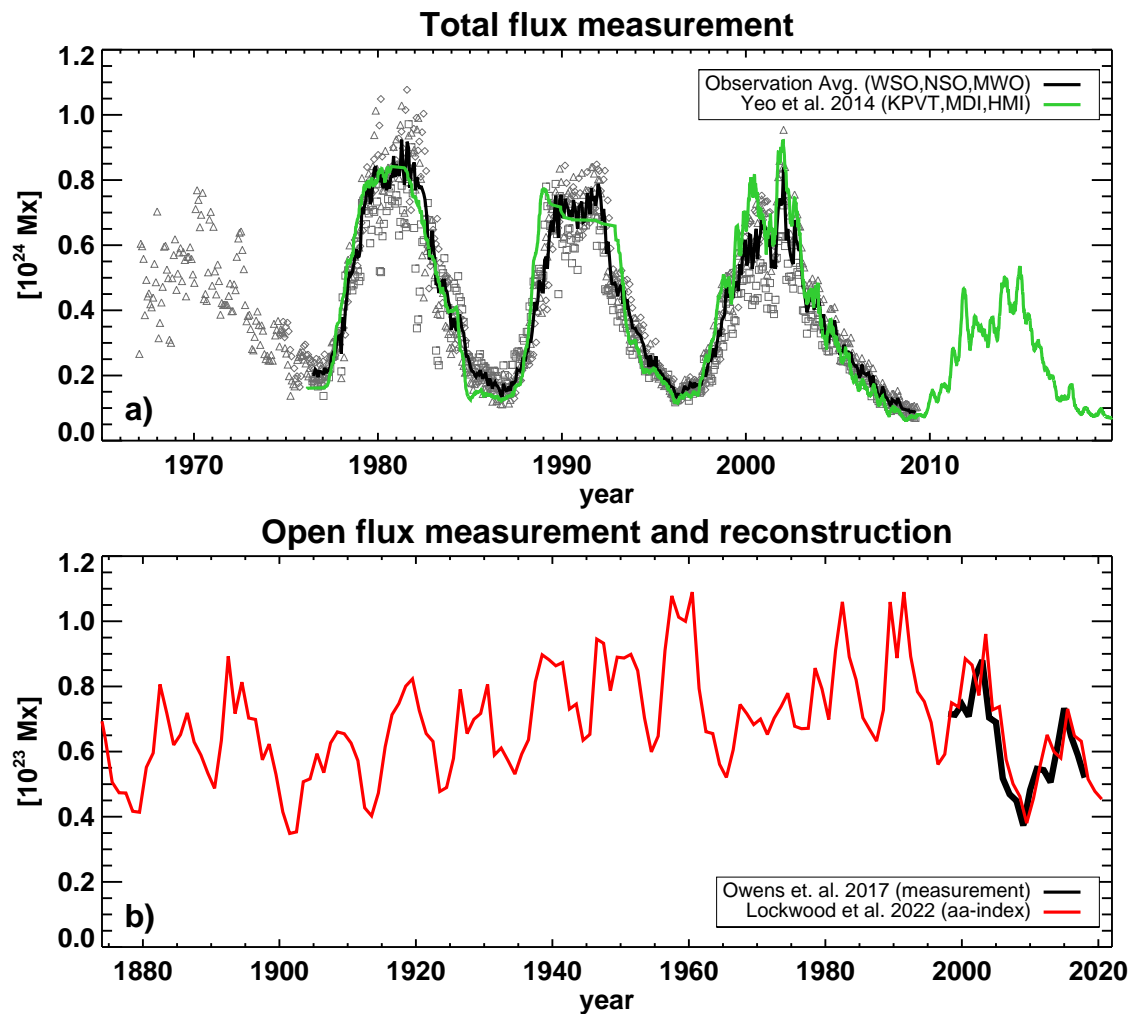


Figure 1.5: a) Measurements of the total magnetic flux. The gray symbols are individual measurements by three ground-based observatories (WSO, NSO and MWO, see main text for details). The black line is the average of all three observatories. The composite by [Yeo et al. \(2014\)](#) from the Kitt Peak Vacuum Telescope (KPVT) at NSO, SoHO/MDI and SDO/HMI (see main text for details) is shown in green. The composite was corrected to the WSO scale. b) Measurement of the open magnetic flux by [Owens et al. \(2017\)](#) (black) and a reconstruction from the geomagnetic *aa*-index by [Lockwood et al. \(2022\)](#).

Observatory at Kitt Peak (NSO, since 1974), see [Arge et al. \(2002\)](#), [Wenzler et al. \(2006\)](#). Later, high resolution full-disc measurements were made by space-based observatories such as the Michelson Doppler Imager on board of Solar and Heliospheric Observatory (SoHO/MDI, since 1996, see [Scherrer et al. 1995](#)) and the Helioseismic and Magnetic Imager onboard Solar Dynamics Observatory (SDO/HMI, since 2010, see [Schou et al. 2012](#)). Measurements of the total magnetic flux by different observatories are shown in Fig 1.5a.

The component of the total flux that reaches into the heliosphere is called the open magnetic flux and as such can directly influence geomagnetic activity on Earth. The strength of the open flux is further related to the strength of the solar interplanetary magnetic field that modulates the amount of GCRs reaching Earth. The GCRs interact with the

molecules in the terrestrial atmosphere and produce cosmogenic isotopes which are then stored in natural archives (see Sect. 1.2.3.2). Measurement of the open flux can be done in-situ, but it is difficult due local distortions by waves, turbulences or reconnection events that can twist and invert the heliospheric magnetic field and lead to an overestimate of the open flux (Owens et al. 2017). Hence, the open flux is often extrapolated from photospheric magnetograms using for example the potential field source surface model (PFSS, Schatten et al. 1969) or the current sheet source surface model (CSSS, Zhao and Hoeksema 1995a,b). The open flux can further be reconstructed from proxies of solar activity such as the abundance of cosmogenic isotopes in natural archives or from geomagnetic activity indices, see Sect.1.3.3. In Fig. 1.5b, we show the open flux measurement by Owens et al. (2017) and a reconstruction from the geomagnetic *aa*-index by Lockwood et al. (2022).

### 1.2.3.2 Other quantities and proxies

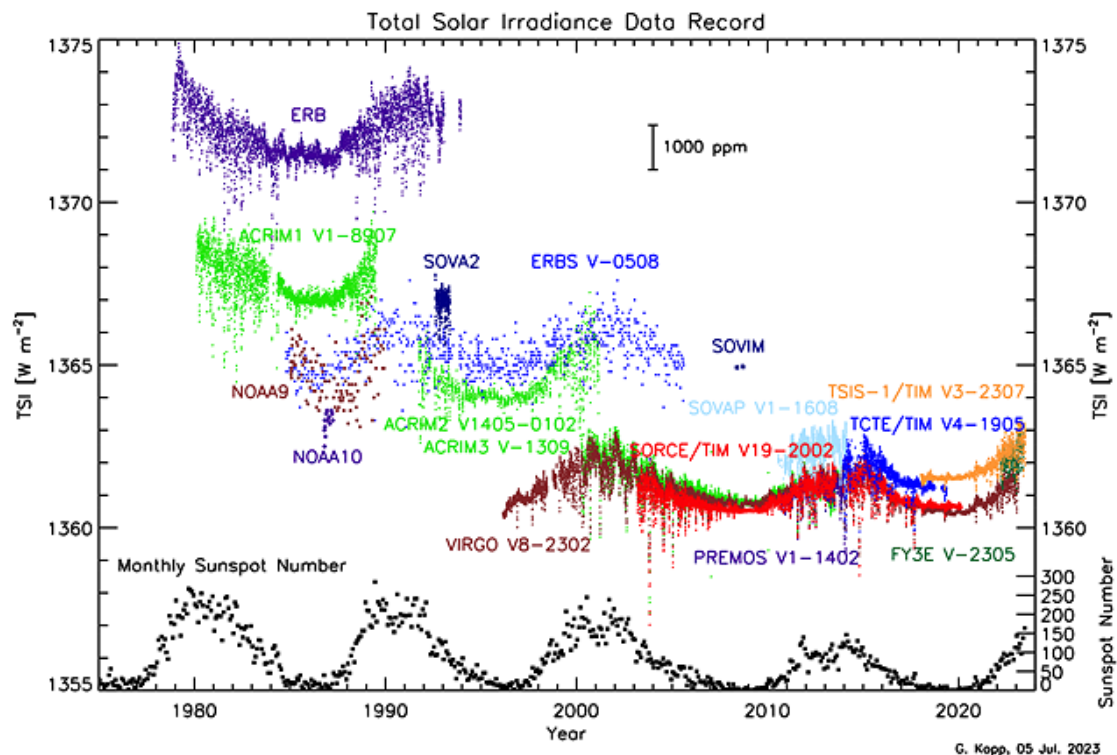


Figure 1.6: Measurements of TSI by various instruments since 1978. Figure is courtesy of Greg Kopp (<https://spot.colorado.edu/~koppg/TSI/>).

The solar magnetic activity cycle also manifests itself in a cyclic variation of the solar irradiance. As the main external energy source into Earth's atmosphere, these variations in the TSI and SSI – especially on longer timescales – may have influence on terrestrial climate. Early ground-based measurements before the 1970s were so inaccurate that they were unable to detect the small variations in the solar irradiance, hence it was called the "solar constant". Ground-based measurements are imprecise for several reasons. Firstly, a part of the solar irradiance spectrum is filtered out by Earth's atmosphere, for example

most of the UV radiation. Secondly, atmospheric and weather effects can lead to variations in the measured TSI which are much stronger than the intrinsic TSI variation itself. Therefore, precise measurements are only available since 1978, with the start of space-based observations (e.g. [Hickey et al. 1980](#), [Willson et al. 1981](#), [Floyd et al. 2003](#), [Kopp et al. 2005](#), [Fröhlich 2012](#), [Schmutz et al. 2013](#)). Multiple different satellite missions have since made TSI measurements (see Fig. 1.6), however the lifetime of the instruments allowed observations only for typically years to a decade. The exception is SoHO/VIRGO<sup>1</sup> that remained operational since 1996. Due to differences in the aperture designs the absolute level of the TSI varies between missions. Instrumental degradation over time further influences the measurements. To assess the long-term variation of TSI, the individual measurements need to be combined and corrected in order to obtain a homogenous and continuous timeseries ([Fröhlich 2012](#), [Kopp 2014](#)).

Three major TSI composites have been produced by different instrumental teams: a) PMOD (Physikalisch - Meteorologisches Observatorium Davos, [Fröhlich 2006](#)), b) ACRIM (Active Cavity Radiometer Irradiance Monitor, [Willson and Mordvinov 2003](#)) and c) RMIB (Royal Meteorological Institute of Belgium or IRMB in french, [Dewitte et al. 2004](#)). The composites rely on "daisy-chainig" (a data series where each new dataset is calibrated to the level of the reference dataset) and taking only data from one instrument at any given time. This method lead to differences between the composites in the long-term trend due to the different calibrations (biased towards the primary instrument) and corrections applied to the data (see e.g. [Solanki et al. 2013](#), [Zacharias 2014](#), [Kopp 2016](#)). Recently, [Dudok de Wit et al. \(2017\)](#) introduced a new methodology to create a single, "community-consensus" TSI composite. Instead of relying on daisy-chaining, the new composite follows a statistical approach that takes the measurements of all available instruments into account. This allows estimating time-dependent uncertainties.

As discussed in Sect. 1.2.3.1, direct measurements of the global solar magnetic field are only available since a few decades. Thus, reconstruction of solar activity on timescales of centuries to even millennia rely on either direct or indirect proxies. The longest and hence most commonly used direct proxy of solar activity is the sunspot number. It is not a "real" physical observable since it is synthetically derived by observers from visual solar disc observations following certain conventions. There are two commonly used versions of the sunspot number: a) the international sunspot number (ISN) since 1700 and b) the group sunspot number (GSN) since 1610, (see also [Usoskin 2017](#)). Since 1874, also information on individual sunspot groups, inclusively areas and positions, is available.

- *International sunspot number*: The first sunspot number series was made by Rudolph Wolf at the Zürich Observatory in 1848, combining his own observations with those by past observers ([Wolf 1850](#)). It is also called the Wolf sunspot number (WSN) or the Zürich sunspot number. The relative sunspot number is defined as:

$$R_Z = k (10G + S), \quad (1.1)$$

where  $k$  is a constant scaling factor used to compensate the differences of observation techniques and instruments of individual observers,  $G$  is the number of sunspot

---

<sup>1</sup>Variability of SOLar Irradiance and Gravity Oscillations onboard the Solar Heliospheric Observatory.

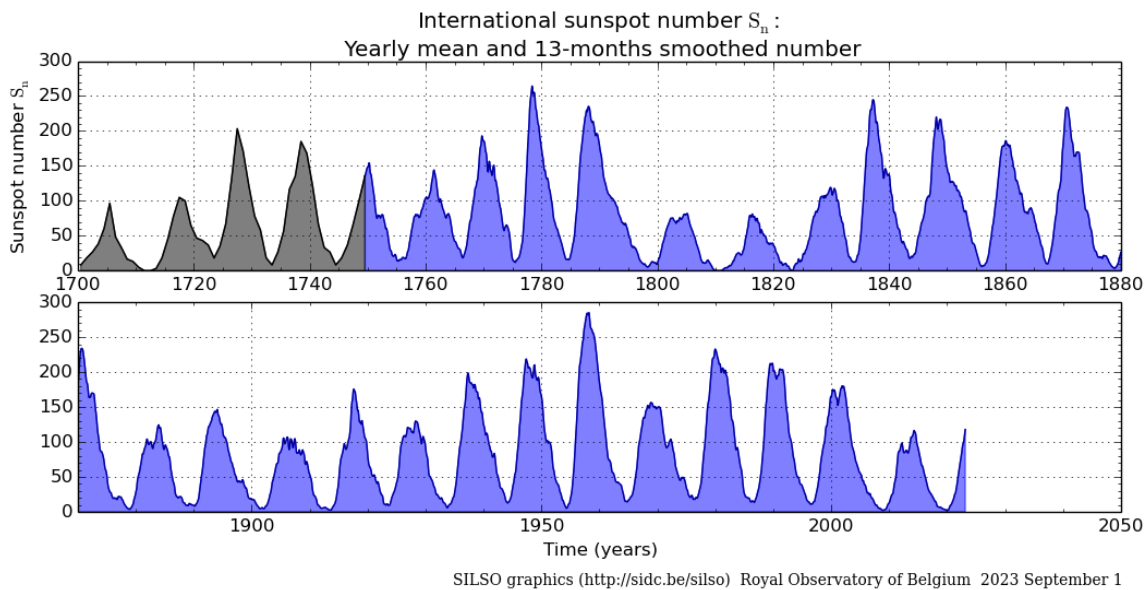


Figure 1.7: Top: International sunspot number (version 2.0) since 1700. The sunspot number in the gray area is given as yearly values, while the blue area shows the 13-month averaged sunspot number since 1749 (from monthly or daily values). Taken from [www.sidc.be/silso](http://www.sidc.be/silso) (SILSO data/image, Royal Observatory of Belgium, Brussels)

groups and  $S$  is the number of individual spots. To make the series more homogeneous he took only the observations of one "primary" observer each day, without taking other observations into account. After 1882, Wolfer became the new primary observer and changed the observation criteria, now counting also small spots and multiple spots within the same penumbra (Clette et al. 2014). To compensate for this change in the observation technique, the data after 1882 were multiplied with a factor of 0.6. The WSN was synthesized until 1981, when it was replaced with the ISN provided by the Royal Observatory of Belgium (Clette et al. 2007). The ISN adopts the same definition as Wolf (Eq. 1.1) but takes all observations into account rather than just the "primary" observer. A second version of the ISN (ISN2.0) was released in 2015, taking Wolfer as a reference (hence this time the data before 1882 had to be multiplied by a factor 1.67) and correcting for inhomogeneities in the data (Clette and Lefèvre 2016). The WSN/ISN is available yearly since 1700, monthly since 1749 and daily since 1818.

- *Group sunspot number*: A new sunspot number series was introduced by Hoyt and Schatten (1998) that neglects individual spots and instead only counts entire sunspot groups, called the group sunspot number. By only considering entire sunspot groups, the GSN reduces the ambiguity in the determination of individual spots by different observers present in the ISN. The GSN uses the averaged sunspot number reported by all observers available on each day. Each observer is thereby given a fixed correction factor to normalize the observations to a similar level. There are also more raw data available than for the ISN, enabling the record

to be extended back to 1610. The GSN is defined as follows:

$$R_g = \frac{12.08}{N} \sum_i k_i G_i, \quad (1.2)$$

where  $N$  is the number of observers on each day,  $k_i$  is the respective correction factor for each observer and  $G_i$  is the reported sunspot number. The factor 12.08 was chosen to adjust the GSN to the level of the ISN in the period between 1874-1976, hence ISN and GSN are rather similar after the 1870s. Although the GSN is considered to be more reliable than the ISN before 1849, inhomogeneities and errors have been reported leading to several revisions of the series (see e.g. [Lockwood et al. 2014b](#), [Cliver and Ling 2016](#), [Svalgaard and Schatten 2016](#), [Usoskin et al. 2016c, 2021a](#), [Chatzistergos et al. 2017](#), [Willamo et al. 2017](#)).

- *Sunspot areas*: Even more information can be obtained from observations of sunspot areas. Sunspot areas are a physical index of solar activity as they are directly measured from solar images and hence it is a direct indicator of the magnetic flux emerging on the solar surface. The longest record of sunspot areas and locations was compiled by the Royal Greenwich Observatory (RGO) since 1874. The series was concluded in 1976 when the US Air Force began recording their own data from the Solar Optical Observing Network (SOON). The two series have later been combined into a continuous record since 1874 by [Hathaway et al. \(2002\)](#), [Hathaway \(2015\)](#) ("RGO/SOON record"). Cross-calibration between the two datasets however is difficult, as there is no temporal overlap, and hence other observatories have been used to cover the transition period. For example [Balmaceda et al. \(2009\)](#) used the Russian dataset by the Pulkovo Astronomical Observatory ([Mikhailov 1955](#)) from 1932 to 1991 that overlaps with both RGO and SOON datasets for the cross-calibration. Recently, [Mandal et al. \(2020\)](#) have derived more consistent sunspot area record, that includes data from multiple additional observatories. The primary observatories are RGO, Pulkovo, Kislovodsk (1952-2018, [Nagovitsyn et al. 2007](#)) and the Debrecen Observatory (since 1977, [Baranyi et al. 2016](#)).

Note that the sunspot area records do not include the tilt angles of the sunspots. The tilt angles can be obtained for example from the observations by Mount Wilson Observatory and Kodaikanal ([Howard et al. 1984, 1999](#), [Sivaraman et al. 1993](#)) covering the period between 1906 to 1987 and the Debrecen Observatory since 1977 ([Baranyi 2015](#)).

The sunspot number records cover the period from 1610 to the present. However, to reconstruct solar activity on even longer timescales, one needs to rely on indirect proxies of solar activity, which are related to effects caused by solar activity rather than being a direct observable. This includes for example the geomagnetic indices (e.g. the *aa*-index), the flux of galactic cosmic rays reaching Earth and the concentrations of cosmogenic isotopes from terrestrial archives. Although we do not directly use indirect proxies as input to our work, we use other studies based on indirect proxies as independent reference cases to our sunspot-based reconstruction of the solar magnetic field (see Chap. 2 and 3).

The *aa*-index is a measurement of geomagnetic activity, conducted by two antipodal stations in Australia and the UK ([Mayaud 1972](#)). Geomagnetic disturbances are caused by

the open field lines of the solar magnetic field interacting with the geomagnetic field and inducing currents. For a review of the relationship between solar and geomagnetic activity see e.g. the review by [Pulkkinen \(2007\)](#). The *aa*-index is calculated as the three hours weighted average of the k-index of both stations, where the k-index is a measurement of the geomagnetic activity relative to an undisturbed geomagnetic field.

The GCR flux in the vicinity of the heliosphere is considered to be almost constant on timescales less than some 100.000 years. However, the GCR flux is modulated before reaching Earth by the heliospheric magnetic field whose strength depends on the solar open magnetic flux. The heliospheric magnetic field acts as a shield from GCRs to the solar system, hence the GCR flux is in anticorrelation with solar activity. The GCR flux has been measured by neutron monitors all around the globe since 1951 (see e.g. [Belov 2000](#), [Simpson 2000](#), [Moraal and Stoker 2010](#), [Jung et al. 2016](#), [Usoskin 2017](#), [Väisänen et al. 2021](#)).

The GCRs that reach Earth's atmosphere interact with nuclei of atmospheric atoms to form cosmogenic isotopes such as  $^{14}\text{C}$  and  $^{10}\text{Be}$  ([Stuiver and Quay 1980](#), [Beer et al. 1990](#), [Bard et al. 1997](#), [Beer et al. 2012](#)). Since these isotopes are mainly produced by GCRs, their production rate is tied to the modulations of the GCR flux, which is in anti-phase with the solar open magnetic flux and solar activity. The cosmogenic isotopes are then deposited in natural archives such as plants ( $^{14}\text{C}$ ) or antarctic ice layers ( $^{10}\text{Be}$ ) ([Lal and Peters 1967](#), [Beer et al. 2012](#)). The isotopes are radioactive with long half-lives of 5730 yr for  $^{14}\text{C}$  and  $\sim 1.5 \times 10^6$  yr for  $^{10}\text{Be}$ . Hence their remaining abundances in terrestrial archives can be used to reconstruct solar activity back for very long time periods from millenia to millions of years (see the review by [Usoskin 2017](#), and Sect. 1.3.3). Dating of  $^{14}\text{C}$  data after the end of the 19th century is however difficult: The production rates of  $^{14}\text{C}$  are diluted by anthropogenic burning of coal and fossil oils also known as the Suess-effect ([Suess 1955](#)). Additionally, nuclear bomb tests in the 1960s have temporarily increased the radiocarbon production rates (see also [Damon et al. 1978](#)).

#### 1.2.4 Emergence patterns of magnetic features and the solar cycle

All the various solar indices described in Sect. 1.2.3 (but also many others) show periodic variations throughout the 11-year solar cycle and, more generally, the 22-year magnetic activity cycle. In this Section, we focus specifically on the emergence of bipolar magnetic regions (ARs, ERs, see Sect. 1.2.2) that have been observed to follow recurrent emergence patterns. These patterns include the number of emerging features, as well as their spatial distribution on the solar surface and the sign of the leading and following magnetic polarity of the BMRs. Here we describe the emergence patterns of sunspot-bearing ARs and discuss how the distribution changes for ERs.

- *Number of regions:* The sunspot number varies greatly with the solar cycle. While few (or zero) sunspots emerge at solar minimum, they cover up to a few percent of the solar surface at activity maximum a few years later (see Fig 1.8). After the polar field reversal near activity maximum (see Sect. 1.3.1) the number of emerging sunspots starts decreasing again. The mean duration of a solar cycle is 11 years since the start of recordings in 1610, but can vary in length by up to a few years. The most extreme cases recorded since 1610 are 8 and 15 years. It has further

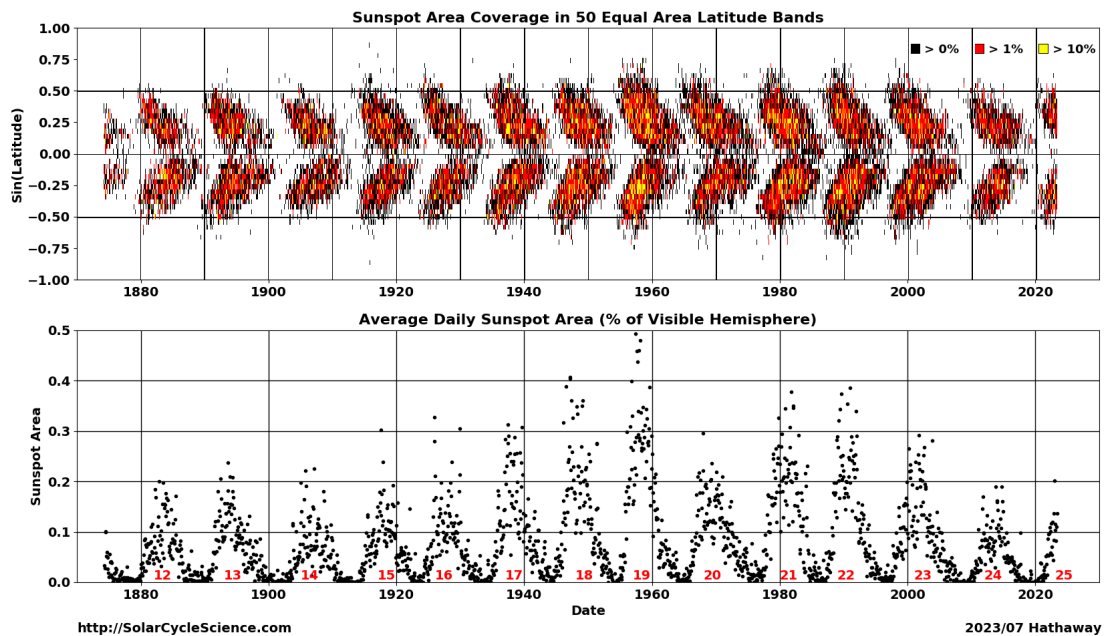


Figure 1.8: Top: Butterfly diagram. The colors represent the solar disc coverage with sunspots. Bottom: Average daily sunspot area. Taken from D. Hathaway (<http://solarcyclescience.com/>)

been observed that the "ascending" or "rising phase" from solar minimum to solar maximum tends to be shorter than the "declining phase" from maximum to the next minimum. The length of the rising phase seems to be anti-correlated with the cycle amplitude, called the "Waldmeier effect" (Waldmeier 1935, 1939).

The number of emerging small, spotless BMRs is up to several orders of magnitude higher than that of large spot-bearing ARs (Harvey 1993, Parnell et al. 2009, Thornton and Parnell 2011). In particular it was discovered that the instantaneous number (Parnell et al. 2009, exponent  $-1.85$ ) as well as the emergence rate (Thornton and Parnell 2011, exponent  $-2.69$ ) of all BMRs can be described by a single power-law size distribution. At the same time, the number of emerging ERs varies less with solar activity than the number of ARs: In a comprehensive study of both small and large scale BMRs in cycle 21 (1976 to 1986), H93 observed that the number of ARs varied by roughly a factor of 8 between solar maximum and minimum, while ERs varied by only a factor of 2. Based on H93's observations, Krivova et al. (2021) have argued that the emergence rate of BMRs throughout the solar cycle can be described by a power-law size distribution with a varying power-law exponent dependent on solar activity (expressed by the sunspot number); see also Chap. 2 and 3 of this thesis.

- *Latitude distribution*: ARs with sunspots typically emerge within certain latitude ranges depending on the phase within the cycle – the so-called "activity bands" or "active latitudes" (e.g. Carrington 1858, Spörer 1879). At the start of the cycle, those activity bands are located between  $\pm 30^\circ$  and  $\pm 40^\circ$ . As the cycle progresses the active latitudes move progressively closer to the equator being at about  $\sim \pm 8^\circ$

at the end of the cycle. A plot of the emergence latitudes of sunspots over time resembles the shape of butterfly wings and is hence called the "butterfly diagram" (see Fig 1.8).

ERs also show the tendency to emerge roughly following the activity bands, however they have a larger spread around the mean than ARs. The smaller the regions are, the wider the spread around the mean, so that the smallest ERs are essentially randomly distributed across the solar surface (Harvey and Martin 1973, H93, Hagenaar et al. 2003).

- *Tilt angles:* As mentioned in Sect. 1.2.2, sunspots emerge in ARs with a positive and negative polarity. The leading polarity of an AR is closer to the equator and the tilt angle between the two polarities with respect to the equatorial plane depends on the emergence latitude (higher tilt angle at higher emergence latitudes). This is also known as "*Joy's law*" (Hale et al. 1919). It has been shown by Dasi-Espuig et al. (2010) that there is a cycle-to-cycle variation in the average tilt angle depending on the maximum sunspot number (i.e. stronger cycles have lower average tilt angles).

Smaller BMRs also tend to obey to Joy's law, but show a much wider scatter around the mean tilt angle which increases with decreasing region size. The smallest ERs appear to be almost randomly orientated (H93, Hagenaar 2001).

- *Polarity:* The leading polarity of a spot-bearing AR shares the same polarity as the polar magnetic field of the respective hemisphere at the beginning of the cycle. This is known as "*Hale's polarity law*" (Hale and Nicholson 1925). However, a small fraction of sunspots violate Hale's law and have the opposite polarity. The fraction of "anti-Hale" regions is small for sunspots ( $\sim 1\%$ ), but increases for smaller BMRs. About 40% of the smallest ERs emerge with anti-Hale orientation (H93, Hagenaar 2001).
- *Cycle overlap:* As can be seen in the butterfly diagram in Fig 1.8 the "wings" of each cycle temporally overlap with those of neighboring cycles, so that higher latitude regions of a new cycle coexist with lower latitude regions of the old cycle. This overlap is about 1 – 2 years for sunspots but can be several years for ERs. Observations suggest that a new solar cycle starts with the emergence of small-scale magnetic regions at high latitudes ( $\sim 50^\circ$ ) immediately after the polar field reversal at maximum of the ongoing cycle. BMRs continue to emerge at low latitudes ( $\sim 5^\circ$ ) for about 2 years after the nominal end of the cycle before the activity bands terminate at the equator (see, e.g. Legrand and Simon 1981, Wilson et al. 1988, H93, Tlatov et al. 2010, Hathaway 2015 and references therein).
- *Activity nests:* The distribution of sunspots and ERs is not entirely random. It has been observed that new BMRs are more likely to form near existing sunspot regions. Such clusters of BMRs are commonly referred to as "activity nests" (see, e.g., Bumba and Howard 1965, Gaizauskas et al. 1983, Castenmiller et al. 1986, Bai 1988). Additionally, it has been proposed that such activity nests might preferably appear at two persistent longitudes in opposite hemispheres separated by  $180^\circ$ , the so called "active longitudes" (Berdyugina and Usoskin 2003, Zhang et al. 2007).

## 1.3 Generation and surface evolution of the solar magnetic field

The variations in solar activity described in Sect. 1.2.3 are driven by the global solar magnetic field. It is generated by a large-scale organized mechanism in the solar interior, called the solar dynamo. The magnetic field then emerges on the solar surface in the form of BMRs (see Sect. 1.2.2). On the solar surface, BMRs are redistributed by a combination of surface plasma flows while also being subjected to decay incited by convective plasma flows. We describe the magnetic field generation by the solar dynamo in Sect. 1.3.1. The evolution of the magnetic field and models used to simulate it are briefly introduced in Sect. 1.3.3.

### 1.3.1 Magnetic field generation

It is generally believed that the solar magnetic field is generated in its interior by rotating motions of the electrically conducting plasma (e.g. Parker 1955, Dikpati and Gilman 2009, Charbonneau 2020). One can describe the time evolution of the magnetic field  $\mathbf{B}$  with the induction equation:

$$\frac{\delta \mathbf{B}}{\delta t} = \eta \nabla^2 \mathbf{B} + \nabla \times (\mathbf{v} \times \mathbf{B}), \quad (1.3)$$

where  $\eta = 1/\mu_0\sigma$  is the magnetic diffusivity,  $\mu_0$  is the vacuum permeability,  $\sigma$  is the electrical conductivity of the plasma and  $\mathbf{v}$  is the plasma velocity. The first term on the right hand side describes magnetic diffusion of the magnetic field while second term describes magnetic induction by plasma flows. The ratio of induction to diffusion is called the Reynolds number  $R_m$  and is of great importance to the understanding of the evolution of the magnetic field:

$$R_m = \mu_0\sigma VL, \quad (1.4)$$

where  $V$  is the typical velocity of the plasma flow and  $L$  is the typical length scale. A low Reynolds number  $\ll 1$  would mean that almost no advection takes place and the magnetic field will tend to diffuse over time. However, when the conductivity of the medium is very high, as is the case in the solar plasma, the diffusion term vanishes and the Reynolds number becomes  $\gg 1$ . In such a case, the motions of the magnetic field and the plasma are no longer independent of each other and are linked together. This phenomenon is known as Alfvén's theorem or the frozen-in magnetic field (see e.g. Priest 2003). Now to understand what will happen in a system with high electric conductivity, we consider the ratio of the gas pressure to the magnetic pressure, called the plasma- $\beta$ . If  $\beta \ll 1$  then the magnetic field pushes the plasma so that it can only move along the magnetic field lines but not cross it. This case is observed in the solar corona due to the low plasma density and the strong magnetic fields. At the photosphere and in the solar interior, the gas (plasma) pressure is much greater so the magnetic field is pushed along with the plasma flows. This way, magnetic field can be generated and amplified by the plasma flows in the solar interior.

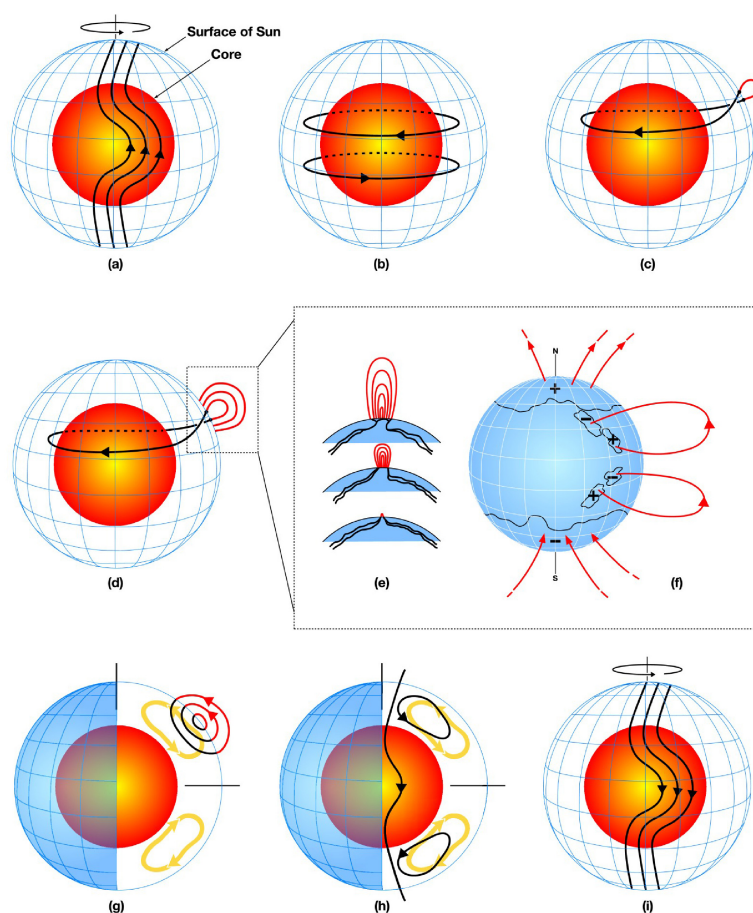


Figure 1.9: Schematic illustration of the Babcock-Leighton dynamo process, see main text for details. Taken from [Dikpati and Gilman \(2009\)](#) with permission (published by Springer Nature<sup>2</sup>, licence number 5600670521274).

Different dynamo models have been proposed that explain the generation of the solar magnetic field and its 22-year magnetic cycle (see the review by [Charbonneau 2020](#)). Here we will focus on the Babcock-Leighton mechanism ([Babcock 1961](#), [Leighton 1964](#)) which has proven great success in explaining the observed patterns of sunspot emergence throughout the solar cycle (see Fig. 1.9, taken from [Dikpati and Gilman 2009](#)). The solar dynamo action can be represented as a two-step process: (1) the generation of toroidal magnetic field from an existing poloidal field configuration and (2) the generation of a new, reversed poloidal field component from the toroidal field. The generation of toroidal magnetic field is thought to happen in the tachocline, the thin transition layer between the radiative zone and the convection zone. While the radiative zone rotates rigidly, the convective zone shows differential rotation, rotating faster at the equatorial regions than at the poles. The resulting shear wraps the poloidal field lines around the rotation axis where it forms a new toroidal field at the bottom of the convection zone; see Figs. 1.9a–1.9b. Once the toroidal field becomes strong enough, it rises through buoyancy until it penetrates the solar surface in the form of  $\Omega$ -shaped loops, accordingly naming this process the  $\Omega$ -effect. The two footpoints of the so-called flux tube stay connected to the

<sup>2</sup><https://doi.org/10.1007/s11214-008-9484-3>

solar surface, where they form the opposite polarity patches of BMRs, the largest of which are active regions that harbour sunspots (see also Sect. 1.2.2). Due to the Coriolis force the flux tubes are twisted into an  $\alpha$ -like shape and the axis between the polarities is tilted so that the leading polarity is closer to the equator, creating a poloidal field component opposite to the existing configuration at the poles, shown in Figs. 1.9c–1.9f. The field in the BMRs is then transported to the poles by a meridional circulation, which flows from the equator to the poles on the surface where it leads to the polar field reversal (e.g. DeVore et al. 1984, Wang et al. 1989). At the bottom of the convection zone the meridional circulation transports the poloidal field back to the equator. Here the new poloidal field is again wrapped up by the differential rotation, starting the dynamo process anew (Figs. 1.9g–1.9i).

### 1.3.2 Surface evolution of the magnetic field

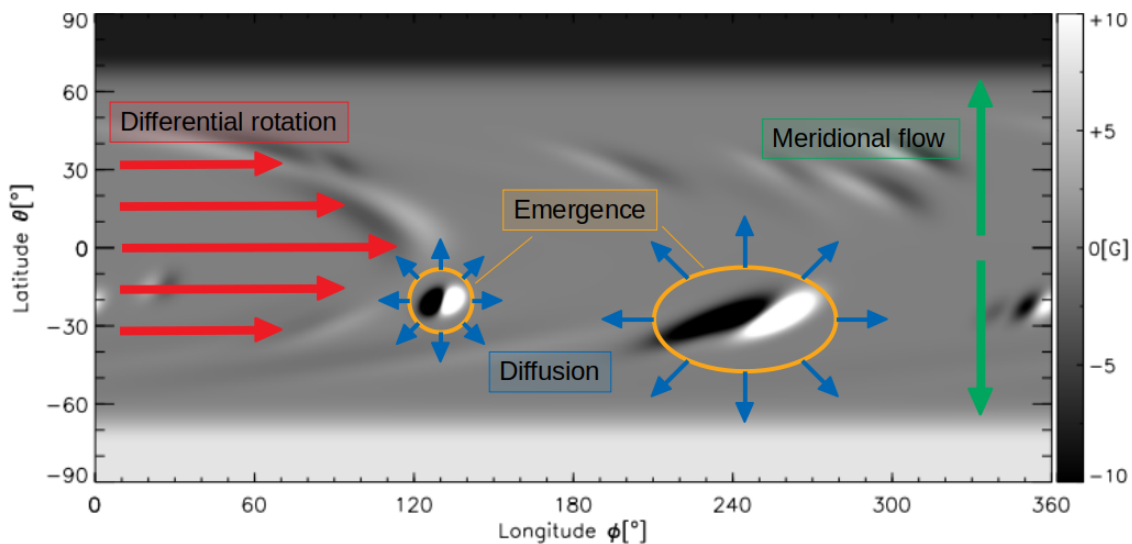


Figure 1.10: Sketch of the effects of surface flows on the magnetic field in a surface flux transport model (see Sect. 1.3.3.2). New emerging BMRs are marked by orange circles. The magnetic field is transported in longitudinal direction by differential rotation (red), toward the poles by meridional flows (green) and diffuses due to supergranular motions (blue).

Upon emergence in the form of BMRs, the magnetic field is subjected to various plasma flows, that morph, transport and diffuse the magnetic surface features (see Fig. 1.10). We briefly introduce the three primary surface flows that play a key role in the evolution of the global magnetic field: (a) Differential rotation, (b) meridional circulation and (c) convective motions.

- *Differential rotation*: Other than the solar radiative zone the solar convection zone does not rotate like a rigid body and instead exhibits differential rotation (see the review by Howe 2009). On the solar surface, its rotation period is about 25 days at the equator, but decreases toward the poles where a full rotation takes around 35 days. A "mean" rotation period of 27.2753 days ("Carrington rotation") was

defined by Richard Carrington who measured the rotation period of low latitude sunspots. Although the definition is somewhat arbitrary, the Carrington longitude is still commonly used to define a solar rotation. The differential rotation also varies with depth, as can be seen in the meridional cut through the Sun in the left panel of Fig. 1.11. In the right panel of Fig 1.11 we see the rotation speed for several latitudes as a function of the distance from the center. One can see how the rigid rotation of the radiative zone transitions into a differential rotation at the tachocline at around  $0.7R_{\odot}$ .

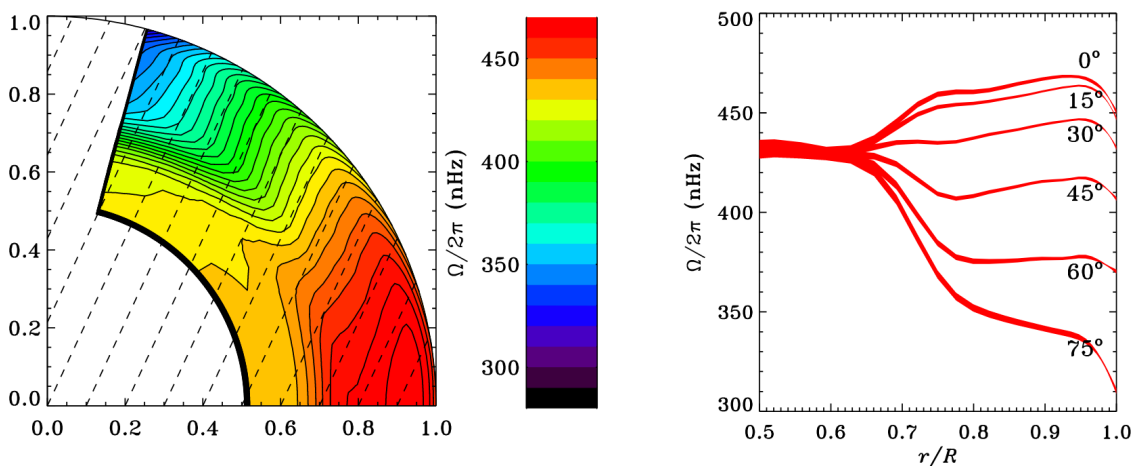


Figure 1.11: Differential rotation profile observed by GONG (Global Oscillation Network Group, Harvey et al. 1996). Left: Cut through the solar convection zone (y-axis is aligned with the rotation axis). The contours depict the solar rotation speed. Right: Solar rotation speed at fixed latitudes by distance from the solar center. Taken from Howe (2009) with permission<sup>3</sup>.

- *Meridional circulation*: The meridional circulation is an axisymmetric system of flows from the equator to the poles on the solar surface. Since the total mass needs to be conserved during the circulation, the plasma at the poles sinks into the interior where it flows back to the equatorial regions where it emerges to the surface again (see the review by Hanasoge 2022). The peak surface flow speed is estimated to  $10 - 20 \text{ m s}^{-1}$  (about 1% of the differential rotation) and decreases towards the equator (where it reverses direction) and towards the poles, as inferred from Doppler measurements (e.g. Duvall 1979, Hathaway 1996, Ulrich 2010), magnetic feature tracking (e.g. Komm et al. 1993, Rightmire-Upton et al. 2012) and helioseismology (e.g. Haber et al. 2002, González Hernández et al. 2008, Komm et al. 2015, 2020). Despite the low flow speed, the meridional circulation is thought to play a crucial role in the solar dynamo (especially for the reversal of the polar fields) as outlined in Sect. 1.3.1.

<sup>3</sup>Published under the *Creative Commons Attribution-Non-Commercial-NoDerivs 3.0 Germany License* (<http://creativecommons.org/licenses/by-nc-nd/3.0/de/>)

- *Convective motions*: As has been described in Sect. 1.2.2, convective plasma motions give rise to a pattern of overturning convection cells at the solar surface. This effect is called granulation for small ( $\sim 1$  Mm) or supergranulation for large scale ( $\sim 30$  Mm) convection cells. Granulation and supergranulation play an important role in the surface flux transport as the plasma motions lead to random walk motions of the surface magnetic field. In surface flux transport models (see Sect. 1.3.3.2) the net effect of those motions is most commonly modelled as a horizontal diffusion process as has been introduced by [Leighton \(1964\)](#). There are however some studies that explicitly model the random motions induced by the supergranulation (e.g. [Schrijver 2001](#), [Upton and Hathaway 2014](#)). Observational studies using cross-correlation and object-tracking methods suggest a typical diffusion coefficient between  $\sim 100 - 350$  km s<sup>-1</sup> (see e.g. [Schrijver et al. 1996](#), [Schrijver and Zwaan 2000](#)).

### 1.3.3 Modelling and reconstructions of magnetic activity

As discussed in Sect. 1.2.3, space-based measurements of the solar surface magnetic field only exist since 1974. Prior to that time one has to rely on direct or indirect proxies (Sects. 1.2.3.2) to reconstruct the solar magnetic field and solar activity in general. Here we will focus on reconstructions from the sunspot number. In Sect. 1.3.3.1 we briefly describe a coarse physical model which calculates the global evolution of the total and open magnetic flux. Then in Sect. 1.3.3.2 we give a brief overview of surface flux transport models which simulate the evolution of the magnetic field on the solar surface.

#### 1.3.3.1 Coarse physical model

A simple but physical and efficient model to calculate the global solar total and open magnetic flux from the sunspot number was developed by [Solanki et al. \(2000, 2002\)](#), [Vieira and Solanki \(2010\)](#). A detailed description of the model (from hereon referred to as "ODE model") can be found in Sect. 2.4.1, so here we give just a brief summary of its basic properties. In the ODE model, a set of coupled ordinary differential equations is solved, each describing the sources and sinks of one component of the total magnetic flux (ARs, ERs and the open magnetic flux that is further split into a fast and a slowly evolving component). The input into the model (or "source") comes from the emergence rates of ARs and ERs, both of which are linked linearly to the sunspot number. Parts of the AR and ER flux are then transferred to the fast and slow open magnetic flux. Finally, all four components (ARs, ERs, fast and slow open flux) decay over time as described by their individual decay timescales.

One of the greatest strengths of the ODE model is its versatility. For example, it has been used in combination with the SATIRE-model (Spectral And Total Irradiance Reconstructions) for solar irradiance reconstructions from the sunspot number ([Krivova et al. 2007, 2010](#), [Balmaceda et al. 2007](#)) Additionally, the simple nature of the model allowed it to be inverted so that the sunspot number can be calculated from the open magnetic flux. Thus, the ODE model was used in combination with reconstructions of the open magnetic flux from the abundances of cosmogenic isotopes such as <sup>14</sup>C and <sup>10</sup>Be in natural archives (for more details see Sect. 1.2.3.2) to reconstruct the historic sunspot

number on a millennial timescale (see e.g. [Solanki et al. 2004](#), [Usoskin et al. 2004, 2016a, 2021b](#), [Vonmoos et al. 2006](#), [Delaygue and Bard 2011](#), [Vieira et al. 2011](#), [Steinhilber et al. 2012](#), [Wu et al. 2018b](#)). The reconstructed sunspot number itself could then again be used as input to the ODE model to reconstruct solar irradiance (see e.g. [Wu et al. 2018a](#)).

However, a shortcoming of the ODE model is that, due to the linear relationship between the emergence rate of ARs and ERs and the sunspot number, the magnetic flux drops to zero in periods of very low activity such as during the Maunder minimum. This stands in contradiction with reconstructions from cosmogenic isotopes that suggest a low but continued activity even during a grand solar minimum. Therefore, an update to the emergence model is urgently needed that allows flux emergence even in the absence of sunspots (see Chap. 2 of this thesis).

### 1.3.3.2 Surface flux transport models

The evolution of the magnetic field on the solar surface can be modelled with a surface flux transport model (SFTM). Originally developed by [DeVore et al. \(1984, 1985\)](#), [Wang et al. \(1989\)](#), a SFTM calculates the effects of several surface plasma flows (see Sect. 1.3.2) while adding new magnetic flux to the magnetograms, either from direct observations or from BMR records. In this section give a general overview of different SFTMs and discuss some of their applications. A more detailed description of the SFTM we use in our study is given in Sect. 3.5.1.

The evolution of the radial solar surface magnetic field  $B_r$  is described by the following equation (see e.g. the reviews by [Jiang et al. 2014b](#), [Wang 2017](#)):

$$\begin{aligned} \frac{\delta B_r}{\delta t} = & -\Omega(\theta) \frac{\delta B}{\delta \phi} - \frac{1}{R_\odot \sin(\theta)} \frac{\delta}{\delta \theta} [v(\theta) B_r \sin(\theta)] \\ & + \frac{\eta_h}{R_\odot^2} \left[ \frac{1}{\sin(\theta)} \frac{\delta}{\delta \theta} \left( \sin(\theta) \frac{\delta B_r}{\delta \theta} \right) + \frac{1}{\sin^2(\theta)} \frac{\delta^2 B_r}{\delta \phi^2} \right] + S(\theta, \phi, t), \end{aligned} \quad (1.5)$$

where  $t$  is the time,  $\theta$  and  $\phi$  are the heliocentric latitude and longitude,  $\Omega(\theta)$  is the differential rotation,  $v(\theta)$  is the meridional circulation and  $\eta_h$  is the horizontal surface diffusivity.  $S(\theta, \phi, t)$  is the "source function" that describes the emergence of new magnetic flux into the model. There are several different ways to feed the source function: The most straightforward way is to directly include observed solar magnetograms (e.g. [Yeates 2020](#)) or Ca II K spectroheliograms (e.g. [Virtanen et al. 2019](#)) into the SFTM. However, as discussed in Sect. 1.2.3.1, such observations only exist since the 1970s and cannot be used for simulations over longer timeperiodes. Another option is to model the emergence of magnetic flux in BMRs from proxies. For this, one can use the sunspot areas and locations, e.g. from the RGO/SOON record since 1874 (see Sect 1.2.3.1). The sunspot areas need to be converted to magnetic fluxes through empirical relationships and the tilt angles have to be modelled following Joy's law ([Sheeley et al. 1985](#)) or a modified, cycle-dependent version of it (e.g. [Cameron et al. 2010](#)). Alternatively one can derive the emergence of BMRs from the sunspot number to further extend the simulation back in time (up to 1610). In this case, the sizes and locations of the BMRs are calculated statistically from empirical relationships (e.g. [Jiang et al. 2011a](#)).

If the source function is fed with BMRs derived from a proxy, we need to model the initial shape in which each BMR appears in the SFTM. For this, BMRs are commonly modelled as a superposition of two opposite polarity patches with some angular separation between them. Two major approaches have been developed to describe the shape of those polarity patches: a) modelling the BMR as a point bipole made of two opposite polarity point sources (Sheeley et al. 1985, Wang et al. 1989) or b) by modelling the BMR with two Gaussian-like polarity patches with a finite area (van Ballegooijen et al. 1998). The second approach was later adopted by e.g. Mackay et al. (2002), Baumann et al. (2004), Cameron et al. (2010), Jiang et al. (2011a), Upton and Hathaway (2014), Nèmec et al. (2022) and is also used in the present study (see Chap. 3).

The ability of SFTMs to simulate the large scale-evolution of the solar magnetic field makes them applicable to many different fields of study. For example, SFTMs can simulate one half of the Babcock-Leighton dynamo loop – the generation of poloidal field from the toroidal field in the form of BMRs on the solar surface (see Sect. 1.3.1), which makes them interesting for dynamo studies (see e.g. the review by Charbonneau 2020). The simulated strength of the polar fields at solar minimum can further be used as a predictor for the strength of the next solar cycle (see e.g. the review by Petrovay 2020). Another important application is to use the magnetic flux derived from simulated magnetograms from a SFTM to reconstruct the historic solar irradiance from sunspot records (Dasi-Espuig et al. 2014, 2016, using the SFTM by Jiang et al. 2011b). However, the SFTM can only calculate the evolution of ARs, so that the contribution of the small-scale ERs is added separately from the simpler ODE model (see Sect. 1.3.3.1). It is specifically the ERs that are driving the secular variation of the magnetic flux and solar irradiance and as such ERs are crucial to constrain the solar variability in long-term studies. Therefore, we need an updated SFTM that can include ERs into the surface flux transport simulations (see Chap. 3).

## 1.4 Motivation & Outline

As described throughout this section, studying the evolution of the solar magnetic field is of great interest to various applications. Many of these require long time-series as input that are not available from direct observations and can only be reconstructed with suitable models. Such models typically require appropriate proxies as input, see Sect. 1.2.3. Unfortunately, the available data become less reliable further back in time. As the longest direct proxy, sunspot number records have been widely used for solar magnetic field and irradiance reconstructions (see e.g. Sect. 1.3.3). However, the sunspot data only capture the presence of large scale magnetic regions, while all the smaller, non-spot-bearing regions are missed. It is known from observations that the number of emerging small magnetic regions varies far less than that of ARs throughout the solar cycle, so that even at low activity with zero sunspots some amount of small-scale features emerge. Therefore, while the day-to-day solar variability is dominated by the emergence of sunspots, it is the small-scale regions that have the strongest impact on the solar secular variation. It is specifically the secular variability that is most important for long term studies of solar activity. For example, the secular variability is crucial for climate studies to assess the influence of the Sun on terrestrial climate. Therefore, a realistic model of the evolution of

the small-scale magnetic regions is urgently needed. Previously, sunspot-driven models struggled to estimate the number of small-scale regions emerging in periods of low solar activity, since no information about their emergence is found in sunspot records. For example, by assuming a linear relationship between ER emergence and the sunspot number (see e.g. Sect 1.3.3.1), no small magnetic regions are present when there are no sunspots on the solar surface. This leads to zero magnetic flux during grand solar minima such as the Maunder Minimum and stands in contrast to data from cosmogenic isotopes. In Chap. 2 of this thesis, we develop a new description of the emergence rates of solar BMRs which is linked non-linearly to the sunspot number and reconstruct the global open and total magnetic flux from a set of ordinary differential equations (see also Sect. 1.3.3.1). The emergence model is then further applied in Chap. 3 together with empirically derived emergence patterns of BMRs to simulate the evolution of the solar magnetic field with a SFTM (see Sect. 1.3.3.2) and to study the influence of small BMRs on the solar magnetic field. We summarize and discuss our results in Chap. 4.



## 2 Modelling the evolution of the Sun's open and total magnetic flux

This chapter reproduces the article by N. A. Krivova, S. K. Solanki, B. Hofer, C. J. Wu, I. G. Usoskin and R. Cameron, published in *Astronomy & Astrophysics*, 650, A70 (2021), reproduced with permission © ESO.

**Contributions to the paper:** B. Hofer took over, tested, partly revised and finalised the programming routines implementing the model. B. Hofer constrained the parameters of the model and ran the final simulations. B. Hofer also contributed to writing the manuscript.

### 2.1 Abstract

Solar activity in all its varied manifestations is driven by the magnetic field. Particularly important for many purposes are two global quantities, the Sun's total and open magnetic flux, which can be computed from sunspot number records using models. Such sunspot-driven models, however, do not take into account the presence of magnetic flux during grand minima, such as the Maunder minimum. Here we present a major update of a widely used simple model, which now takes into account the observation that the distribution of all magnetic features on the Sun follows a single power law. The exponent of the power law changes over the solar cycle. This allows for the emergence of small-scale magnetic flux even when no sunspots are present for multiple decades and leads to non-zero total and open magnetic flux also in the deepest grand minima, such as the Maunder minimum, thus overcoming a major shortcoming of the earlier models. The results of the updated model compare well with the available observations and reconstructions of the solar total and open magnetic flux. This opens up the possibility of improved reconstructions of sunspot number from time series of cosmogenic isotope production rate.

### 2.2 Introduction

The precise history of solar activity and its underlying magnetic field is of interest for a number of reasons. Firstly, records of solar activity and of the magnetic field pose an important constraint on models for the enhancement and the evolution of magnetic flux (mainly dynamo models). Secondly, such records are important for understanding the history of the Sun's influence on the Earth (either through changes in its irradiance, or through space weather effects). Thirdly, a long record of solar activity is needed to

understand how the Sun compares with other sun-like stars in its level of activity and variability (e.g., [Radick et al. 2018](#), [Reinhold et al. 2020](#)).

Solar activity, in all its diverse manifestations, is driven by its magnetic field, so that knowledge of the history of solar activity implies knowledge of its magnetic field. Two widely used quantities describing the global magnetic field of the Sun are the global open and unsigned total magnetic flux. They are, for example, used in heliospheric physics, for the reconstruction of solar irradiance, or as measures of solar activity when comparing with other stars. These quantities, being global in nature, can be reconstructed from more indirect proxies of solar activity and magnetism, such as the sunspot number and concentrations of the cosmogenic isotopes  $^{14}\text{C}$  or  $^{10}\text{Be}$  in terrestrial archives.

A first model to compute the solar open flux from the sunspot number was developed by [Solanki et al. \(2000\)](#), based on a simple differential equation describing the evolution of the open flux,  $\phi_{\text{open}}$ . In spite of its simplicity, it successfully reproduced the empirically-reconstructed evolution of the open flux by [Lockwood et al. \(1999\)](#) and the  $^{10}\text{Be}$  concentration in ice cores ([Beer et al. 1990](#)). This simple model was extended by [Solanki et al. \(2002\)](#) to cover also the total unsigned magnetic flux,  $\phi_{\text{total}}$ , but now requiring the solution of a set of coupled differential equations to describe the evolution of ephemeral regions (ERs) besides that of active regions (ARs) and of the open flux. All three components of magnetic flux contribute to the evolution of the total magnetic flux. ARs are the large bipolar structures that harbour sunspots at least part of the time, whereas ERs are smaller bipolar regions without sunspots.

The ability of this model to reproduce concentrations of cosmogenic isotopes turned out to be particularly useful (e.g., [Usoskin et al. 2002](#)). Although far more sophisticated models are in the meantime available to compute not just global magnetic quantities, but also the underlying spatial distribution of the magnetic flux and the detailed input from individual emerging ARs etc., the very simplicity of this set of models allowed them to be inverted (e.g., [Lockwood 2003](#)), so that, e.g., sunspot number could be reconstructed from measured concentrations of cosmogenic isotopes (e.g., [Usoskin et al. 2003, 2004](#), [Solanki et al. 2004](#), [Usoskin et al. 2016b](#), [Wu et al. 2018b](#)). The model of [Solanki et al. \(2002\)](#) was further extended and combined with the successful SATIRE model (Spectral And Total Irradiance REconstruction; [Fligge et al. 2000](#), [Krivova et al. 2003, 2011](#)) to compute total solar irradiance over the last 400 years ([Krivova et al. 2007, 2010](#)). [Vieira and Solanki \(2010](#), hereafter VS2010) have further refined the model by distinguishing between the short-lived and long-lived components of the open flux ([Ikhsanov and Ivanov 1999](#), [Cranmer 2002](#), [Crooker et al. 2002](#); see [Vieira and Solanki 2010](#) for details), which led to an improved reconstruction of the open flux that displayed a better agreement with observations. This model, with some tuning, has been the basis for further reconstructions of solar spectral irradiance over the telescope era ([Krivova et al. 2010](#)), as well as sunspot number and TSI over the Holocene ([Vieira et al. 2011](#), [Wu et al. 2018b,a](#)).

One shortcoming of earlier versions of the model discussed above is that the open flux during a grand minimum, such as the Maunder minimum, i.e. during a long period essentially without sunspots, invariably drops to zero. This is because in this model, the emergence rate of the magnetic field on the solar surface is linearly linked to the sunspot number, so that by design during a grand minimum no magnetic flux is allowed to emerge. This leads to a zero open and total flux during the grand minima. It has been shown, however, that signals of solar activity and variability were also present during the

Maunder minimum (Beer et al. 1998, Fligge et al. 1999, Usoskin et al. 2001, Miyahara et al. 2004, Riley et al. 2015). This was also confirmed by modelling (Owens et al. 2012) and points to a need for an improvement of the global total and open magnetic flux model.

Furthermore, more recent solar observations provided new insights into the sources, emergence and evolution of the solar magnetic flux. Thus, Thornton and Parnell (2011) have combined observations from various sources and found that the emergence rate of bipolar magnetic regions with fluxes between  $10^{16}$  Mx and  $10^{23}$  Mx follows a single power law with a slope of  $-2.69$ .

Here we present a new, strongly revised version of the VS2010 model that builds on these recent solar observational results, replacing the direct proportionality of ERs and ARs by a more up-to-date approach. It does keep the original differential equations, however, so that it is not a completely independent model. As a natural outcome of the model, ERs keep emerging even during a grand minimum when there are no sunspots for multiple decades. This means that neither the open nor the total magnetic flux drop to zero at any time.

The paper is structured as follows. The data used to constrain and test the new model are briefly introduced in Sect. 2.3. We describe our model and highlight the changes relative to the older version of the model in Sect. 2.4. The results of the model are presented in Sect. 2.5, while we summarise and discuss our findings in Sect. 2.6, where we also provide an outlook on future applications of the new model.

## 2.3 Data

The model to be detailed in Sect. 2.4 starts from a sunspot number time series and computes the total and open magnetic fluxes of the Sun therefrom. We therefore require a sunspot series as input to the model. To constrain the free parameters of the model, we compare its output to observations and independent data-based reconstructions of the total and open magnetic fluxes. Finally, to test the output of the model, we consider further independent time series of the reconstructed open magnetic flux.

As input to the model we use the following sunspot number data sets: (1) the international sunspot number v2.0, referred to hereafter as ISN2.0 (Clette and Lefèvre 2016), and (2) the group sunspot number, or GSN in short (Hoyt and Schatten 1998). The ISN2.0 data set was extended back to 1643 by adding the sunspot data during the Maunder minimum by Vaquero et al. (2015) scaled up by the factor 1.67 to match the ISN2.0 definition. Also in the GSN record, the values before 1710 were replaced by the data from Vaquero et al. (2015), without any scaling.

To constrain the output of the model we make use of observations of the total magnetic flux (see Arge et al. 2002, Wang et al. 2005, Wenzler et al. 2006) derived from synoptic charts produced by the three solar observatories with the longest running regular magnetographic measurements: Wilcox Solar Observatory (WSO), Mount Wilson solar Observatory (MWO), and National Solar Observatory at Kitt Peak (NSO/KP). These data sets have already been used to constrain earlier versions of this model and we have used the same versions as employed by Krivova et al. (2007, 2010) and Wu et al. (2018a). To constrain the free parameters of the model, we consider the average over at least two (MWO and WSO during 2002–2009) or all three (1976–2002) records for each Carrington-

ton rotation.

Furthermore, to better constrain the free parameters of the model, we also use the empirical reconstruction of the open magnetic flux from the geomagnetic aa-index covering the period from 1845 to 2010 (Lockwood et al. 2014a).

Finally, the quality of the computed open magnetic flux is tested by comparing it with two other independent data sets (without changing the free parameters of the model): (1) a compilation of spacecraft-based in-situ measurements by Owens et al. (2017) since 1998, and (2) a reconstruction by Wu et al. (2018b) from decadal INTCAL13  $^{14}\text{C}$  data covering the Holocene prior to 1900 (Reimer et al. 2013).

## 2.4 Model

### 2.4.1 Magnetic flux emergence and evolution

Following the approach by Solanki et al. (2000, 2002) and Vieira and Solanki (2010), we describe the evolution of the solar total and open magnetic flux by a system of ordinary differential equations. However, instead of distinguishing between active regions (AR) and ephemeral regions (ER) as the sources of fresh magnetic flux at the solar surface, we distinguish between ARs and what we call Small-Scale-Emergences (SSEs), i.e. all emergences with fluxes smaller than those in active regions. These therefore combine the flux emerging in the form of ephemeral regions and smaller magnetic bipoles all the way down to internetwork fields. The equations describing the evolution of the different (globally averaged) components of the magnetic flux are:

$$\frac{d\phi_{\text{AR}}}{dt} = \varepsilon_{\text{AR}} - \frac{\phi_{\text{AR}}}{\tau_{\text{AR}}^0} - \frac{\phi_{\text{AR}}}{\tau_{\text{AR}}^s} - \frac{\phi_{\text{AR}}}{\tau_{\text{AR}}^r}, \quad (2.1)$$

$$\frac{d\phi_{\text{SSE}}}{dt} = \varepsilon_{\text{SSE}} - \frac{\phi_{\text{SSE}}}{\tau_{\text{SSE}}^0} - \frac{\phi_{\text{SSE}}}{\tau_{\text{SSE}}^s}, \quad (2.2)$$

$$\frac{d\phi_{\text{open}}^r}{dt} = \frac{\phi_{\text{AR}}}{\tau_{\text{AR}}^r} - \frac{\phi_{\text{open}}^r}{\tau_{\text{open}}^r}, \quad (2.3)$$

$$\frac{d\phi_{\text{open}}^s}{dt} = \frac{\phi_{\text{AR}}}{\tau_{\text{AR}}^s} + \frac{\phi_{\text{SSE}}}{\tau_{\text{SSE}}^s} - \frac{\phi_{\text{open}}^s}{\tau_{\text{open}}^s}, \quad (2.4)$$

$$\phi_{\text{open}} = \phi_{\text{open}}^r + \phi_{\text{open}}^s, \quad (2.5)$$

$$\phi_{\text{total}} = \phi_{\text{AR}} + \phi_{\text{SSE}} + \phi_{\text{open}}. \quad (2.6)$$

Here  $\phi_{\text{AR}}$ ,  $\phi_{\text{SSE}}$ ,  $\phi_{\text{open}}$  and  $\phi_{\text{total}}$  refer to the magnetic flux in ARs and SSEs, as well as the open, and total magnetic flux (all magnetic fluxes are global, i.e. referring to their unsigned sum over the entire solar surface). The open flux is divided into rapidly ( $\phi_{\text{open}}^r$ ) and slowly ( $\phi_{\text{open}}^s$ ) evolving components.  $\tau_{\text{AR}}^0$ ,  $\tau_{\text{SSE}}^0$ ,  $\tau_{\text{open}}^r$ , and  $\tau_{\text{open}}^s$  are the decay timescales of ARs, SSEs, rapid open flux, and slow open flux, respectively. The flux transfer timescales from ARs and SSEs to slow open flux are  $\tau_{\text{AR}}^s$  and  $\tau_{\text{SSE}}^s$ , respectively, while the corresponding timescale for the transfer of AR flux to the rapid open flux is  $\tau_{\text{AR}}^r$ . See Vieira and Solanki (2010) for a discussion on the distinction between rapidly and slowly evolving open magnetic flux.

In the original model, the emergence rate of ARs at a given time  $t$ ,  $\varepsilon_{\text{AR}}(t)$ , was linked linearly to the sunspot number, SN, at that time:

$$\varepsilon_{\text{AR}}(t) = \varepsilon_{\text{AR}}^{\text{max},21} \frac{\text{SN}(t)}{\text{SN}^{\text{max},21}}, \quad (2.7)$$

where  $\varepsilon_{\text{AR}}^{\text{max},21}$  and  $\text{SN}^{\text{max},21}$  are the three-month averaged emergence rate and SN value observed during the maximum of cycle 21 (taken from [Schrijver and Harvey 1994](#)), respectively. Because at the time that the model was originally developed, large-scale studies of magnetic flux emergence and evolution could not resolve internetwork fields, the earlier model was restricted to ERs as the only magnetic bipoles smaller than ARs. The emergence rate of the ERs,  $\varepsilon_{\text{ER},n}$ , of the cycle  $n$  was not well known and was assumed to be a sinusoidal function,  $g^n$ , which was stretched such that the length of the ER cycle was longer than the respective sunspot cycle. The amplitude of the ER cycle was simply taken to be proportional to the maximum value of the emergence rate of the ARs of the cycle, so that the emergence rate of ERs over a cycle had the form:

$$\varepsilon_{\text{ER},n} = \varepsilon_{\text{AR}}^{\text{max},n} X g^n, \quad (2.8)$$

where  $X$  is an amplitude factor (a free parameter of the model; same for all cycles). Importantly, Eq. 2.8 implies a linear relationship between the emergence rate  $\varepsilon_{\text{ER},n}$  and the sunspot number. This, along with the linear relationship between  $\varepsilon_{\text{AR},n}$  and sunspot number (Eq. 2.7) results in an absence of flux emergence during extended periods of spotless days.

To overcome this shortcoming, we incorporate more recent solar observations by [Thornton and Parnell \(2011\)](#) into the model. Using high-resolution Hinode, Solar Optical Telescope/Narrow-band Filter Imager (SOT/NFI) observations and combining them with earlier published data, they found that the emergence rate of the magnetic flux on the Sun follows a power-law distribution:

$$\frac{dN}{d\phi} = \frac{n_0}{\phi_0} \left( \frac{\phi}{\phi_0} \right)^m, \quad (2.9)$$

where  $\phi_0 = 10^{16}$  Mx (the smallest flux per feature that they include in their histograms),  $n_0 = 3.14 \times 10^{-14} \text{ cm}^{-2} \text{ day}^{-1}$  and  $m = -2.69$  (see the illustration in Fig. 2.1).

We note that [Thornton and Parnell \(2011\)](#) have summarised the results from multiple studies with a wide range of solar activity levels and observing conditions. In earlier studies, [Harvey and Zwaan \(1993\)](#) and [Harvey \(1993\)](#) found that the emergence rate of ARs varied significantly more between solar activity minimum and maximum than that of ERs. Whereas roughly 8.3 times more ARs emerged during the maximum of cycle 21 than during the minimum (the factor generally grows with the size of the regions, but was on average about 8.3 for all the ARs they studied), this ratio was roughly two for ERs. The number of the smallest magnetic features, forming the internetwork magnetic fields and having fluxes of  $10^{16} - 10^{17}$  Mx, appears to be nearly invariable over an activity cycle ([Buehler et al. 2013](#), [Lites et al. 2014](#)). These features differ from the larger ones in that they are mainly brought about by a small-scale turbulent dynamo ([Voegler and Schuessler 2007](#), [Rempel 2014](#)) that produces the same amount of magnetic flux nearly independently of large-scale activity.

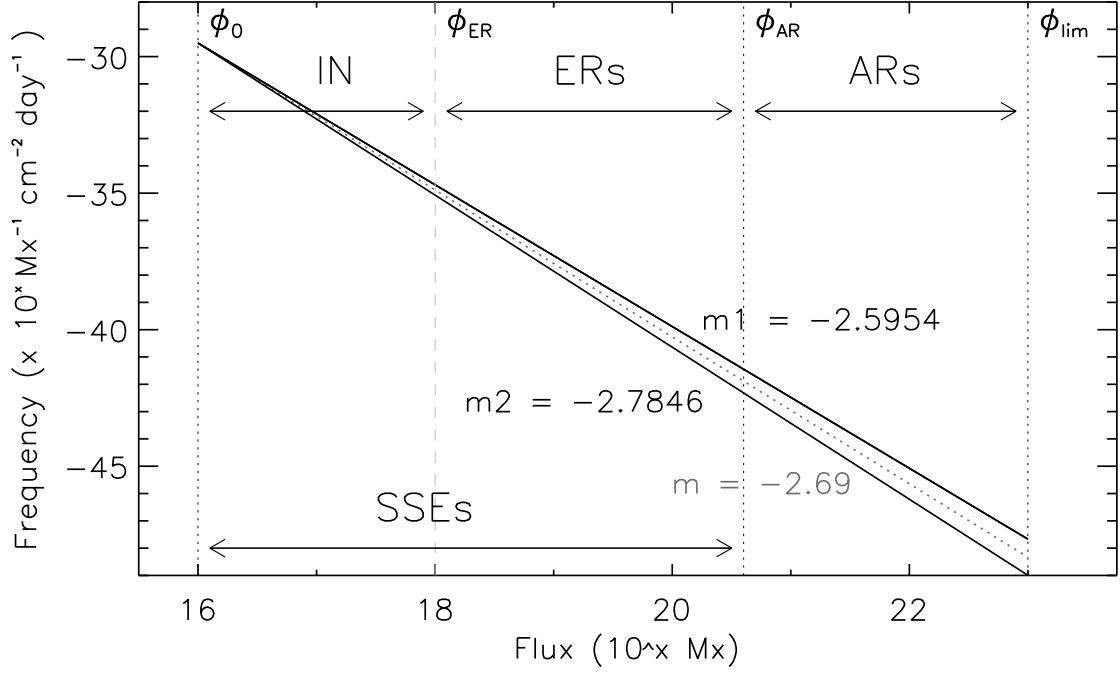


Figure 2.1: Frequency of emergence vs. the unsigned flux of an emergence event (see Eq. (2.9) following Thornton and Parnell 2011).  $\phi_0$ ,  $\phi_{ER}$ ,  $\phi_{AR}$  and  $\phi_{limit}$  represent the limit below which the local dynamo flux dominates, the minimum ephemeral region flux, the minimum active region flux, and the upper limit of the active region flux, respectively. The horizontal arrows mark the flux ranges corresponding to the internetwork (IN), ephemeral regions (ERs), active regions (ARs), and Small-Scale Emergences (SSEs). The SSE range includes IN fields and ERs. The slope  $m$  of the distribution was derived by Thornton and Parnell (2011) by fitting various observations at different activity levels. Slopes  $m_1$  and  $m_2$  represent the corresponding distributions at maximum and minimum of solar activity levels for cycle 21, respectively (see main text for details).

To satisfy these observational constraints, on the one hand, we keep the number of the smallest magnetic features considered here (with a flux per feature of  $10^{16}$  Mx) fixed at all times. On the other hand, we allow the exponent  $m$  to vary (cf. Parnell et al. 2009, Schrijver and Harvey 1989) around the empirical value  $m = -2.69$  found by Thornton and Parnell (2011) within the range  $m_1 \geq m \geq m_2$ , where  $m_1 = m + \Delta m$  and  $m_2 = m - \Delta m$ . The slopes  $m_1$  and  $m_2$  describe the distributions of emergence rates during periods when the observed sunspot numbers are  $SN_1$  and  $SN_2$  (with  $SN_1 > SN_2$ ). In our model, the slope  $m$  follows the SN,  $m(SN)$ , according to the non-linear relationship:

$$m(SN) = m_1 - (SN_1^\alpha - SN^\alpha) \frac{m_1 - m_2}{SN_1^\alpha - SN_2^\alpha}, \quad (2.10)$$

where  $\alpha$  is a free parameter, fixed by comparing the output of the model to observations and independent reconstructions (see Sect. 2.4.2).

Now, the emergence rate of magnetic flux in ARs and SSEs at any given time can be calculated as:

$$\varepsilon_{AR} = \int_{\phi_{AR}}^{\phi_{limit}} \frac{n_0}{\phi_0} \left(\frac{\phi}{\phi_0}\right)^m \phi \, d\phi = \frac{n_0}{(m+2) \phi_0^{m+1}} (\phi_{limit}^{m+2} - \phi_{AR}^{m+2}), \quad (2.11)$$

and

$$\varepsilon_{\text{SSE}} = \int_{\phi_0}^{\phi_{\text{AR}}} \frac{n_0}{\phi_0} \left(\frac{\phi}{\phi_0}\right)^m \phi \, d\phi = \frac{n_0}{(m+2)\phi_0^{m+1}} (\phi_{\text{AR}}^{m+2} - \phi_0^{m+2}). \quad (2.12)$$

Here  $\phi_{\text{AR}} = 4 \times 10^{20}$  Mx denotes the magnetic flux of the smallest bipolar regions hosting sunspots, i.e. the smallest active regions (e.g., [Zwaan 1978](#), [Schrijver and Zwaan 2000](#), [van Driel-Gesztelyi and Green 2015](#)) and  $\phi_{\text{limit}}$  is the flux of the largest considered ARs. Since such regions are extremely rare, the exact value of  $\phi_{\text{limit}}$  is not important. Following [Parnell et al. \(2009\)](#) and [Thornton and Parnell \(2011\)](#), we take  $\phi_{\text{limit}} = 10^{23}$  Mx, which is somewhat larger than the maximum flux ( $3 \times 10^{22}$  Mx) for ARs listed by [Schrijver and Zwaan \(2000\)](#) and [van Driel-Gesztelyi and Green \(2015\)](#). Tests have shown that also the exact value of  $\phi_{\text{AR}}$  adopted here plays only a minor role for the end result in the sense that although the free parameters may have slightly different values, the computed open and total magnetic flux remain almost unchanged.

To estimate how the slope  $m$  of the distribution given by Eq. (2.9) changes with activity (Eq. (3.2)) we rely on the observations by [Harvey and Zwaan \(1993\)](#) and [Harvey \(1993\)](#) for cycle 21. They found that the number of emerging ARs in cycle 21 varied between the activity maximum and minimum by a factor of roughly 8.3. The monthly-smoothed sunspot numbers corresponding to these periods (1979 – 1982 for the maximum, as well as 1975 – 1976 and 1985 – 1986 for the preceding and following minima) are then  $\text{SN}_1 = 217$  and  $\text{SN}_2 = 17$ , respectively. These values are obtained for ISN2.0. For GSN, these numbers correspond to  $\text{SN}_1 = 130$  and  $\text{SN}_2 = 10$ . By using the factor of 8.3 found for the emergence frequency of ARs between activity maximum and minimum by [Harvey \(1993\)](#) as a constraint, we obtain  $\Delta m = 0.0946$  (and thus  $m_1 = -2.5954$  and  $m_2 = -2.7846$ ).

Note that the values of  $m$  reach values higher than  $m_1$  or lower than  $m_2$  at times when the sunspot number is higher than  $\text{SN}_1$  or lower than  $\text{SN}_2$ , respectively. In particular, when the sunspot number is zero, the corresponding  $m$  values are  $m(0) = -3.952$  for ISN2.0 and  $m(0) = -3.677$  for GSN. The value of  $m(0)$  is different for ISN2.0 and GSN because the value of  $\alpha$ , the free parameter of the model (see Table 2.1, and Sect. 2.4.2) is different:  $\alpha = 0.059$  for ISN2.0 and  $\alpha = 0.075$  for GSN. The largest value of  $m$  that the direct sunspot records give is obtained for the peak of cycle 19, with  $\max(\text{SN}) = 370$  (ISN2.0) and 247 (GSN), which results in  $m(370) = -2.552$  (ISN2.0) and  $m(247) = -2.542$  (GSN). Figure 2.2a shows the daily (black) and the monthly-smoothed (red) ISN2.0, while the evolution of  $m_{\text{SN}}$  computed from the monthly-smoothed ISN for the solar cycle 21 is shown in Fig. 2.2b.

## 2.4.2 Parameters of the model

Our model, described in Sect. 2.4.1, has a number of parameters, summarised in Table 2.1. The upper part of the table lists quantities taken or deduced from the literature and kept fixed throughout the analysis, whereas the five free parameters that are allowed to vary when fitting the data sets described in Sect. 2.3 are given in the lower part. One positive feature of the new model is that it has less free parameters than the old model (the old model required two free parameters to describe the emergence of ERs; see Table 1 of [Wu et al. 2018a](#)), giving it less ‘wriggle room’ for reproducing observational data.

All parameters relevant to the emergence rates of ARs and SSEs (Eqs. 2.9–2.12) have been described in the previous section. Here we additionally comment on the decay and

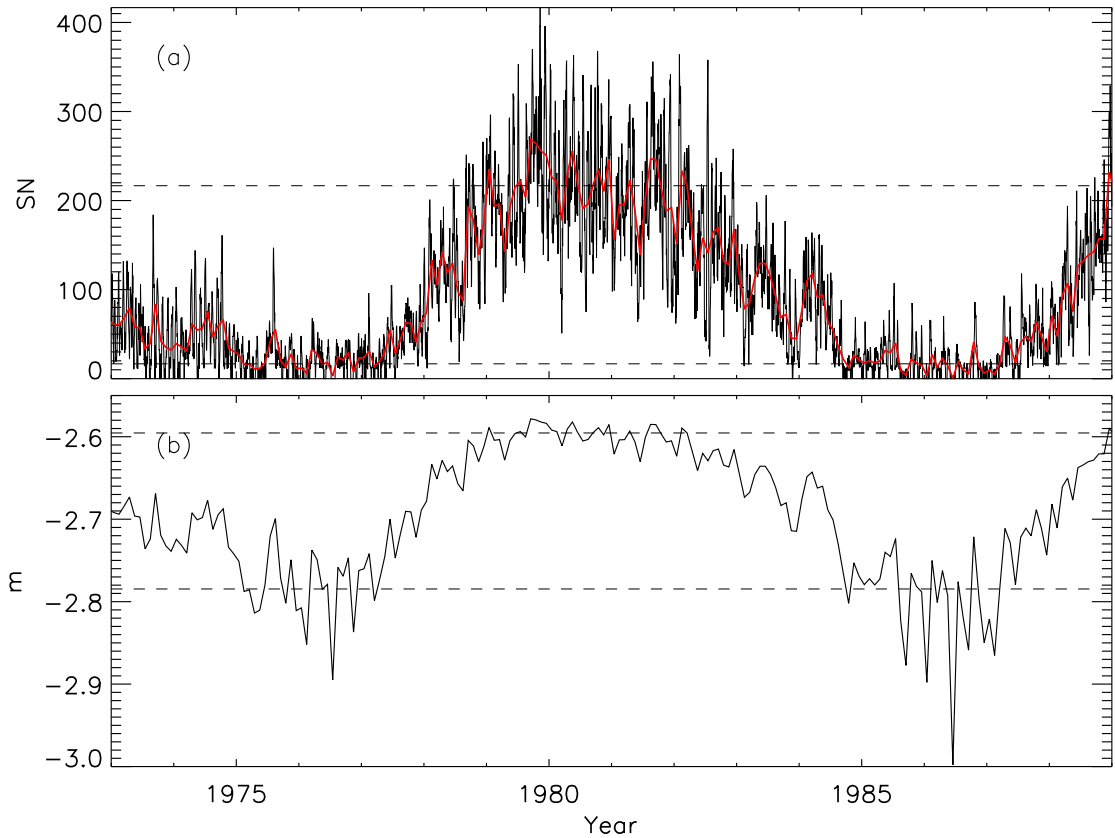


Figure 2.2: (a) Daily (black) and 30-day smoothed (red) sunspot number (ISN, v2.0) over cycle 21, including the adjacent minima. The average values during the activity maximum ( $SN_1 = 217$ ) and minimum ( $SN_2 = 17$ ) of cycle 21 are marked by the horizontal dashed lines. (b) Evolution of the monthly-smoothed power-law slope  $m$  over the same period, the horizontal dashed lines mark  $m_1 = -2.5954$  corresponding to  $SN_1 = 217$  and  $m_2 = -2.7846$  corresponding to  $SN_2 = 17$ .

transfer times of the various components of the magnetic flux used in the ordinary differential equations describing the flux evolution (Eqs. 2.1–2.6).

The decay times of the ARs and SSEs,  $\tau_{AR}^0$  and  $\tau_{SSE}^0$ , are estimated using the observations by Parnell et al. (2009) and Thornton and Parnell (2011). Whereas Thornton and Parnell (2011) have analysed the emergence rate of different features as a function of their flux, Parnell et al. (2009) analysed the magnetic flux for all (i.e. instantaneously) observed features. By dividing the total number of the features of a given flux observed at a given instance by their emergence rate, we arrive at their mean lifetime. The lifetime of the features increases with their sizes or fluxes. For our purpose we make a simplification and calculate the lifetimes of ARs and SSEs as averages over all regions with fluxes above and below  $\phi_{AR}$ , respectively, thus obtaining  $\tau_{AR}^0 \approx 10$  days and  $\tau_{SSE}^0 \approx 6$  minutes. Since the features with the smallest flux dominate the power law distribution,  $\tau_{AR}^0$  is short compared with lifetimes of large ARs and is closer to lifetimes of small ARs (e.g., Table 1 of the review by van Driel-Gesztelyi and Green 2015). For the same reason the SSE lifetime is close to that of internetwork elements, rather than of ERs. To compare better with observations of ERs, we therefore introduce  $\phi_{ER} = 10^{18}$  Mx (see Fig. 2.1), which

Table 2.1: Parameters of the model.

Parameter	ISN	GSN	W18 (ISN)
$n_0, \text{cm}^{-2} \text{day}^{-1}$	$3.14 \times 10^{-14}$		...
$\phi_0, \text{Mx}$	$10^{16}$		...
$\phi_{\text{AR}}, \text{Mx}$	$4 \times 10^{20}$		...
$\phi_{\text{limit}}, \text{Mx}$	$10^{23}$		...
$\text{SN}_1$	217	130	...
$\text{SN}_2$	17	10	...
$m$	-2.69		...
$\Delta m$	0.0946		...
$\tau_{\text{AR}}^0, \text{yrs}$	0.027		...
$\tau_{\text{SSE}}^0, \text{yrs}$	$1.1 \times 10^{-5}$		...
$\alpha$	0.059	0.075	...
$\tau_{\text{open}}^r, \text{yrs}$	0.16	0.09	0.14
$\tau_{\text{open}}^s, \text{yrs}$	3.98	3.90	3.75
$\tau_{\text{AR}}^r, \text{yrs}$	2.79	1.57	2.6
$\tau_{\text{AR}}^s, \text{yrs}$	88.15	89.81	88.3
$\tau_{\text{SSE}}^s, \text{yrs}$	10.15	10.11	20.6 *

**Notes.** The upper part of the table lists parameters that are fixed, whereas the lower part lists free parameters. For comparison, the last column (W18) lists the values of the free parameters of the old model from the most recent version by [Wu et al. \(2018a\)](#).

\* This value was obtained by [Wu et al. \(2018a\)](#) for ERs rather than SSEs.

denotes roughly the lowest magnetic flux contained within ERs. If we now consider as ERs only the regions with  $\phi_{\text{ER}} < \phi < \phi_{\text{AR}}$ , then we obtain a lifetime  $\tau_{\text{ER}}^0 \approx 2$  hours, which is comparable to the lifetimes of  $\approx$ hours to a day for regions with fluxes between  $3 \times 10^{18}$  Mx and  $10^{20}$  Mx listed by [van Driel-Gesztelyi and Green \(2015\)](#). The maximum to minimum change of the flux emerging in ERs (i.e. with fluxes  $\phi_{\text{ER}} < \phi < \phi_{\text{AR}}$ ) in our model is roughly a factor of 2.5, which is consistent with the results by [Harvey \(1993\)](#) and [Harvey and Zwaan \(1993\)](#). We stress that this distinction into ERs and internetwork fields is only used for comparison purposes. Within the model they are not distinguished (see Sect. 2.4.1).

The decay timescales of the rapid,  $\tau_{\text{open}}^r$ , and slow,  $\tau_{\text{open}}^s$ , open flux, as well as timescales for the flux transfer from ARs and SSEs to slow open flux,  $\tau_{\text{AR}}^s$  and  $\tau_{\text{SSE}}^s$ , respectively, and the timescale for the transfer of the AR flux to the rapid open flux,  $\tau_{\text{AR}}^r$ , are free parameters of the model (together with  $\alpha$  governing the change of the slope  $m$  with the SN, as described in Sect. 2.4.1). These parameters are fixed by comparing total and open magnetic flux with the corresponding observations listed in Sect. 2.3.

To do this, we use the genetic algorithm PIKAIA ([Charbonneau 1995](#)), which searches for the set of parameters minimising the difference between the modelled and the reference data sets. We minimise the sum of the reduced chi-squared values,  $\chi^2$ , taking the errors of the observations and the number of data points into account. In other words, we search for the maximum of  $1/(\chi_{\text{total}}^2 + \chi_{\text{OMF}}^2)$ ; see [Vieira and Solanki \(2010\)](#) for details and [Dasi-Espuig et al. \(2016\)](#) for a discussion of uncertainties in the parameter fitting. The

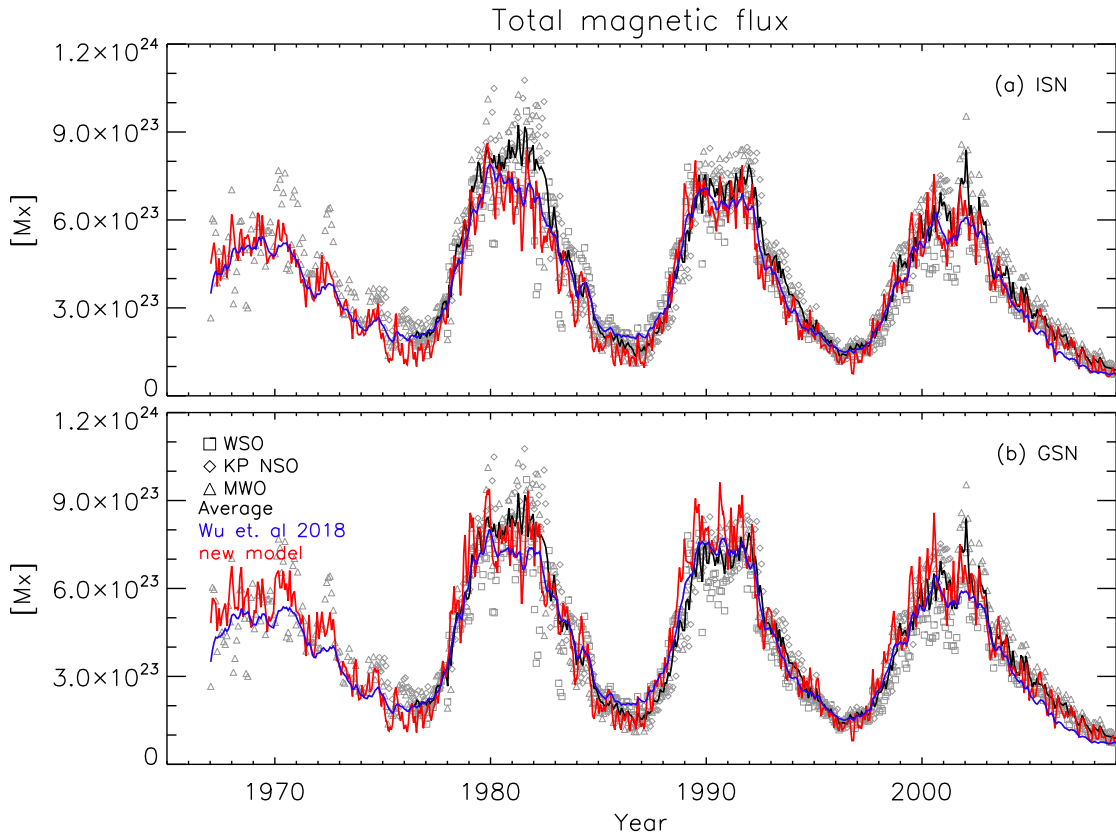


Figure 2.3: Evolution of the total magnetic flux over cycles 21–24 computed with the new (red) and old (blue) models, as well as the observed flux. For observations, symbols show individual Carrington rotations and observatories, as indicated in the legend, and black solid line shows their average. For the models, means of the daily total magnetic flux over the Carrington rotations are shown, and the contribution of the SSEs is reduced by a factor of 0.4 (see text for details). Panels (a) and (b) use ISN and GSN as input, respectively.

best-fit values of the parameters are listed in Table 2.1.

For comparison, the last column of Table 2.1 also lists the values of the five free parameters that are already present in the VS2010 model, as obtained by Wu et al. (2018a) for the most recent version of the model. This version used the same ISN2.0 input record extended back with the data from Vaquero et al. (2015) as done here. The values of the parameters are very close in the two models, except  $\tau_{\text{SSE}}^s$ , for which Wu et al. (2018a) obtained 20.6 years compared to our 10.15 years (10.11 years when using GSN). Note, however, that Wu et al. (2018a) considered ERs rather than SSEs. Interestingly, the values we obtain are close to the value of 10.08 years found to produce a best-fit by Vieira and Solanki (2010) and is within the range 10–90 years that is consistent with observation (see Vieira and Solanki 2010).

The value of about 4 years for the decay time of the slow open flux  $\tau_{\text{open}}^s$  is close to the radial decay term with a timescale of 5 years introduced into surface flux transport simulations by Schrijver et al. (2002) and Baumann et al. (2006) to act on the unipolar fields at the solar poles. This was needed to reproduce the observed polar field reversals. Similarly, the  $\tau_{\text{open}}^r$  obtained here (Table 2.1) is consistent with the estimate of the decay

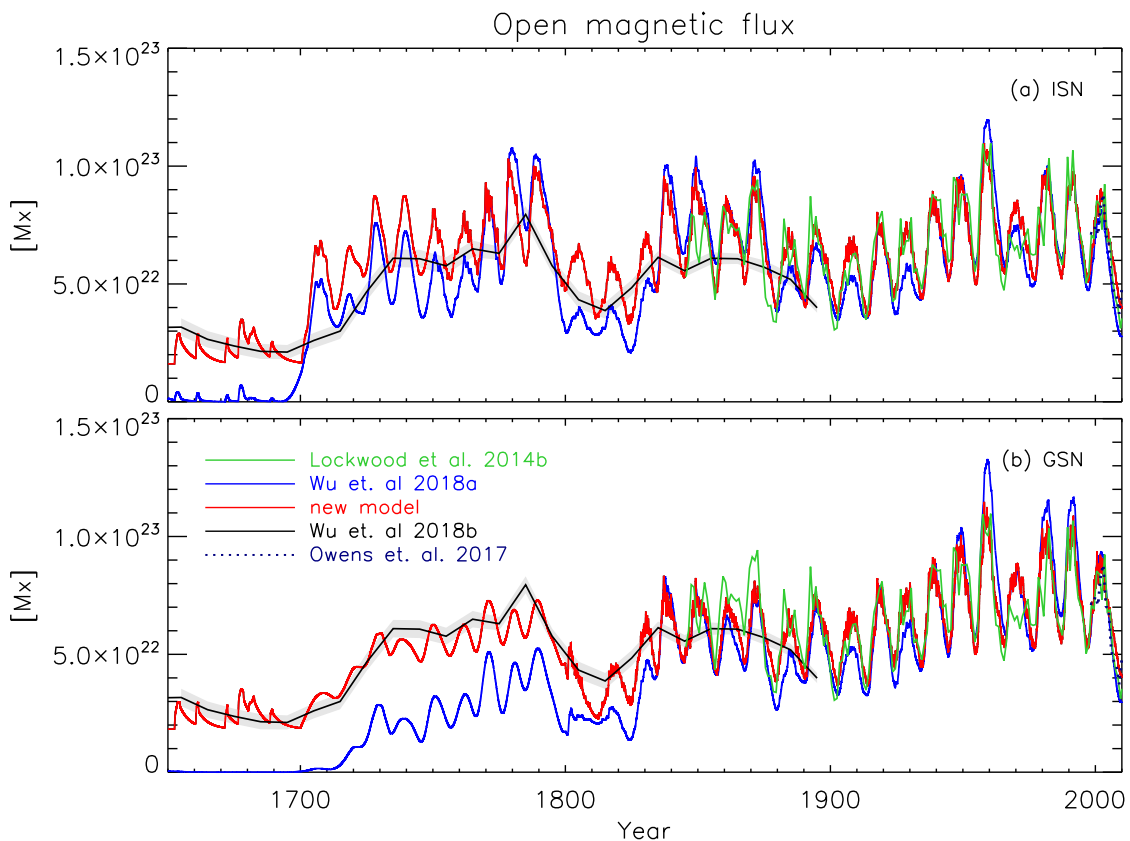


Figure 2.4: Open magnetic flux computed with the new (red) and old (blue) models, together with the empirical reconstruction from the geomagnetic aa-index (Lockwood et al. 2014a, green). Also shown are the reconstruction by Wu et al. (2018b, black solid line with shading marking the uncertainty) from the decadal INTCAL13  $^{14}\text{C}$  data (Reimer et al. 2013) and the in-situ measurements from Owens et al. (2017, dotted blue line) since 1998. Panels (a) and (b) use ISN and GSN as input, respectively.

of closed flux carried by interplanetary coronal mass ejections, between 1 and 5 AU of between 38 and 55 days by Owens and Crooker (2006).

## 2.5 Reconstruction of the total and open magnetic flux

The computed total magnetic flux from 1965 onward is plotted in Fig. 2.3. Following Krivova et al. (2007), to account for the flux undetected due to the limited spatial resolution of observations (see Krivova and Solanki 2004a), the contribution of the ER flux was multiplied by a factor of 0.4 before adding it to the contribution from the ARs and the open flux. Shown are means over the daily values for each Carrington rotation. The new and old models are depicted in red and blue, respectively. Symbols show the observations: Wilcox Solar Observatory (WSO, squares), National Solar Observatory at Kitt Peak (NSO KP, diamonds), and Mount Wilson Observatory (MWO, triangles). Each individual symbol represents the total photospheric magnetic flux over a given Carrington rotation. To compute the  $\chi^2$  value, we use the average of the three (1976–2002) or two

Table 2.2: Comparison of the modelled open and total magnetic fluxes to observations and independent reconstructions, quantified through their relative differences in means (in %) and reduced  $\chi^2$  values (listed in brackets).

Input model version	ISN		GSN	
	old	new	old	new
$F_{\text{total}}$	-7.7 (0.037)	-9.9 (0.058)	-4.1 (0.037)	0.8 (0.058)
$F_{\text{open,L14}}$	-2.2 (0.297)	0.4 (0.176)	-4.6 (0.389)	-1.6 (0.219)
$F_{\text{open,Wu18b}}^*$	-15.1 (1.718)	6.1 (0.630)	-48.5 (1.674)	-9.6 (0.230)
$F_{\text{open,O17}}$	-15.4 (0.655)	3.8 (0.236)	-3.5 (0.495)	5.8 (0.252)

**Notes.** The top part of the table lists the data sets that were used for parameter fitting (the average of the total magnetic flux measurements and the open flux reconstruction by [Lockwood et al. 2014a](#)), while the bottom part lists independent data sets that were not used for the optimisation (OF reconstruction from  $^{14}\text{C}$  data by [Wu et al. 2018b](#) and the in-situ measurements by [Owens et al. 2017](#)).

\* For decadal-averaged reconstructions. As  $^{14}\text{C}$  data used for the reconstruction by [Wu et al. \(2018b\)](#) are decadal averages, only decadal-averaged values of the OF could be reconstructed. Thus, to compute the corresponding  $\chi^2$  values, our reconstructions were re-sampled, too.

(after 2002, see Sect. 2.3) datasets indicated by the black solid line.

The computed open magnetic flux is shown in Fig. 2.4. The new model is shown in red, the old model is in blue, and the reconstruction from the geomagnetic aa-index by [Lockwood et al. \(2014a\)](#) is represented by the green line. Also shown are the in-situ measurements by [Owens et al. \(2017\)](#), dotted blue line) since 1998 and a reconstruction (black solid line with shading indicating the uncertainty) of the open flux by [Wu et al. \(2018b\)](#) from independent decadal INTCAL13  $^{14}\text{C}$  data ([Reimer et al. 2013](#)). Note that the underlying  $^{14}\text{C}$  data and thus also the OF reconstructed from them are decadal averages. The agreement between our model and the  $^{14}\text{C}$ -based reconstruction is quite good. Particularly impressive is the agreement in the level of the open flux during the Maunder minimum, which is where we expect to see the biggest improvement relative to the old model. We emphasise that this  $^{14}\text{C}$ -based record was not used to constrain our model. (Note that in the old model, the GSN record was used without the data from [Vaquero et al. \(2015\)](#) over the Maunder minimum, and the computed open flux in the old model is therefore essentially flat at the zero level.) Interestingly, over the 19th and the first half of the 18th centuries, the GSN-based reconstruction is closer to the isotope-based open flux than the reconstruction from the ISN, which lies somewhat higher.

A quantitative comparison of the total and open magnetic fluxes resulting from the old and the new models with the observations and independent reconstructions is presented in Table 2.2. The table lists the relative difference in means and the  $\chi^2$  values (in brackets) between the models and the data. For the total magnetic flux, the results are quite similar for both versions of the model. In both cases, the mean modelled total magnetic flux is somewhat closer to the observations when the GSN is used as input. The absolute difference in the means is slightly higher or lower for the new model if ISN2.0 or GSN are used, respectively. The new  $\chi^2$  values are somewhat higher than in the old model. This is,

however, primarily due to fact that, by model design, the variability of the ER component on time scales shorter than the solar cycle in the old model was essentially smoothed out (see Eqs. 2.7–2.8) resulting in weaker short-term fluctuations than in the new model (see Fig. 2.4). Thus, if we smooth the total flux from both models with a 3-months window before comparing, the  $\chi^2$  values for the old model remain almost unchanged (0.036 for both ISN2.0 and GSN), while those for the new model decrease to 0.043 for ISN2.0 and 0.047 for GSN. In all cases, the  $\chi^2$  values are quite low.

For the open flux, the new model provides a notably better fit than the old model to all three alternative datasets. In all but one case, the absolute mean differences are significantly lower for the new model. The only exception is the GSN-based reconstruction versus the in-situ data by Owens et al. (2017), for which the absolute mean difference is slightly lower for the old model. However, the results are quite close for both versions of the model in this case. Note also that these data cover only a short recent period of time, over which the two models do not differ significantly. The  $\chi^2$  values are lower for the new model in all cases. The fit is poorest for the reconstruction based on the decadal values of  $^{14}\text{C}$ . Very recently, new  $^{14}\text{C}$ -based activity measures with annual resolution were published by Brehm et al. (2021). An application of our model to the dataset of Brehm et al. (2021) will be subject of a separate publication (Usoskin et al., submitted).

## 2.6 Summary and discussion

We have revised the simple model describing the evolution of the Sun’s global total and open magnetic flux, originally proposed by Solanki et al. (2000, 2002) and improved by Vieira and Solanki (2010). The new version of the model takes into account the observation that fluxes of magnetic features follow a single power law, including internetwork fields, ERs and ARs (Parnell et al. 2009; cf. Anusha et al. 2017). It also takes into account the fact that emergence rates of magnetic bipoles with fluxes between  $10^{16}$  Mx and  $10^{23}$  Mx, i.e. from the smallest ERs (and large internetwork features) to the largest ARs, also follow a power law according to the analysis by Thornton and Parnell (2011).

We assume that the difference in emergence rates between the maximum and the minimum of solar activity is adequately described by the varying power-law exponent, affecting magnetic features with fluxes  $\phi > 10^{16}$  Mx. Thus, for the smallest features there is no change in emergence rate over the solar cycle, while the ratio of emergence rates during maximum to minimum increases steadily with increasing magnetic flux. Thus, the number of emerging ARs varies between the solar maximum and minimum of cycle 21 by a factor of 8.3, while this factor is 2.5 for ERs and close to unity for internetwork fields. These values are consistent with the respective ratios found by Harvey and Zwaan (1993) and Harvey (1993), while the fact that the flux in internetwork fields hardly changes over the cycle is in agreement with the results obtained by, e.g., Buehler et al. (2013) and Lites et al. (2014).

Using the sunspot number time series as input, the model returns time series of the open and total magnetic flux of the Sun. These resulting time series reproduce the open magnetic flux between 1845 and 2010 reconstructed by Lockwood et al. (2014a) and total magnetic flux averaged over individual Carrington rotations obtained by various observatories between 1976 and 2009.

The main novel feature of the results of the model is that, in contrast to the earlier versions of the model, the output open magnetic flux does not drop to essentially zero during the Maunder minimum when almost no sunspots were present for multiple decades, in agreement with open flux reconstructed from  $^{14}\text{C}$  data (e.g., [Wu et al. 2018b](#)). This significant improvement is a result of the model allowing for a non-zero emergence of magnetic flux in small-scale bipolar features (encompassing ERs and internetwork fields) even during extended periods when sunspots were not present, e.g. during the Maunder minimum and other, similar grand minima (e.g., [Usoskin et al. 2007](#)).

Even with this major update, the model still has some room for further improvements. Because it uses sunspot numbers as input (the only data of solar activity available prior to the middle of the 19th century), it cannot properly treat variations in solar activity that are not reflected in the number of sunspots. This is particularly evident during grand minima. During such times sunspots are only occasionally visible, whereas cosmogenic isotopes continue to display cyclic variations. This suggests that, in the context of the present model, the slope  $m$  continues to vary in a cyclical manner and can go lower than the lowest value we have obtained ( $m(0) = -3.952$  for ISN2.0 and  $m(0) = -3.677$  for GSN).

In the old version of the model the ER emergence was constructed as a smooth, sinusoidal function. In the new model, ER (and internetwork) emergence rate closely follows that of sunspots and has therefore the same temporal resolution as the input sunspot number series. As a consequence, the new model does not feature temporal lags or shifts to the corresponding sunspot cycle, as in the old model. However, it does account for the finding by [Harvey \(1994\)](#) that small-scale features (in her study ERs) belonging to a given cycle start emerging at a relatively high rate well before the sunspot cycle starts. The internetwork is independent of sunspot emergence and is, thus, not associated with a particular sunspot cycle. These regions are simply a result of the dynamo not having completely switched off even at times when there are no sunspots visible. In this way, the overlap between neighbouring solar magnetic cycles is naturally introduced. This was the main feature of the original model of [Solanki et al. \(2000\)](#) responsible for the change in the level of the Sun's open magnetic flux from one solar minimum to another, first noticed by [Lockwood et al. \(1999\)](#). At the same time, the new model allows for the dynamo to continue working and produce activity cycles during grand minima, which are sufficiently strong to modulate cosmic rays (see, e.g., [Fig. 2.4](#) for the evolution of the open flux during the Maunder minimum) and hence influence the production of cosmogenic isotopes ([Beer et al. 1998](#), [Fligge et al. 1999](#), [Usoskin et al. 2001](#)), but are too weak to produce more than occasional sunspots.

The higher level of the magnetic flux during periods of very low solar activity (e.g. during the Maunder and the Dalton minima, see [Fig. 2.4](#)) will presumably lead to a weaker secular variation of the total solar irradiance (TSI) and in particular the rise of the TSI since the Maunder minimum (cf., [Yeo et al. 2020](#)), an important parameter for understanding the influence of solar irradiance variability on long-term climate trends (e.g., [Gray et al. 2010](#), [Solanki et al. 2013](#)). The influence of the revised magnetic flux time series on TSI will be the subject of a future investigation.

Another important application of this model will be in reconstructing total magnetic flux and sunspot numbers from production rates of cosmogenic isotopes. Such an application will require the model to be inverted, as has successfully been done with the older

version of the model (e.g., [Usoskin et al. 2003](#), [2004](#), [Solanki et al. 2004](#), [Usoskin et al. 2016b](#), [Wu et al. 2018b](#)). Such work is ongoing and will be the subject of a follow-on publication.

### **Acknowledgements**

We thank Mathew Owens for the helpful comments and stimulating discussion. NAK and SKS acknowledge support by the German Federal Ministry of Education and Research (Project No. 01LG1909C). SKS received support from the Ministry of Education of Korea through the BK21 plus program of the National Research Foundation. BH was supported by the International Max-Planck Research School (IMPRS) for Solar System Science at the University of Göttingen. IU acknowledges a partial support from the Academy of Finland (Projects ESPERA no. 321882).



# 3 The influence of small bipolar magnetic regions on basic solar quantities

This chapter is based on a manuscript in preparation for submission by B. Hofer, N. A. Krivova, R. Cameron, S. K. Solanki and J. Jiang. An updated version of this chapter has been submitted for publication to *Astronomy & Astrophysics*.

**Contributions to the paper:** B. Hofer has implemented the new description of the BMR emergence rates (Chap. 2) in the SFTM code, revised and extended the statistical relationships describing the spatial and temporal BMR emergence patterns and also incorporated them into the SFTM code. B. Hofer has adapted the code and ran all simulations. B. Hofer also did the theoretical analysis of the role of small BMRs and wrote the manuscript draft.

## 3.1 Abstract

Understanding the solar magnetic field's evolution is of great importance for, e.g., heliosphere, dynamo and irradiance studies. While the contribution of the field in active regions (ARs) hosting sunspots to the Sun's large-scale field has been extensively modelled, we still lack a realistic model of the contribution of smaller-scale magnetic regions such as ephemeral active regions that do not contain any sunspots. In this work, we study the effect of small and large bipolar magnetic regions (BMRs) on the large-scale solar magnetic field. The evolution of total and open magnetic flux, the polar fields and the toroidal flux loss since 1874 is simulated with a surface flux transport model (SFTM) and the results are compared to analytical considerations. For this purpose, we derive semi-synthetic BMR records using the international sunspot number as a proxy. We calculate the emergence rate of all BMRs from a single power-law size distribution, whose exponent varies with solar activity. The spatial distribution of the BMRs is calculated from statistical relationships derived from various solar observations. We include BMRs with magnetic flux as low as  $2 \times 10^{20}$  Mx in our SFTM, corresponding to regions with lifetimes down to one day. We find a good agreement between the computed total magnetic flux and observations, even though we do not have a free parameter to adjust the simulated total flux to observations, as in earlier versions of the employed SFTM. The open flux, the polar fields and the toroidal flux loss are also consistent with observations and independent reconstructions. Small BMRs contribute about one third of the total and open flux at activity maximum, which increases to one half at activity minimum. An even greater impact is found on the polar fields and the toroidal flux loss, where small BMRs

contribute an equal amount to spot-containing ARs at all activity levels. The majority of the statistical noise in the simulation is caused by large ARs, while small BMRs have a stabilizing effect on the simulations, especially for the polar field reversals. We conclude that small BMRs play an important role in the evolution of the solar magnetic field also at large spatial scales. Their impact is largest at low solar activity, but is also substantial during activity maxima. Their inclusion in SFTM simulations will allow the secular variability in solar irradiance to be better constrained and the generation of the poloidal field in the Babcock-Leighton dynamo to be better understood.

## 3.2 Introduction

Understanding solar activity and variability is of great societal importance due to their potential to affect Earth, its climate and life on it, as well as the heliosphere (Haigh 2007, Pulkkinen 2007, Gray et al. 2010, Temmer 2021). The driver of solar activity and variability is the magnetic field of the Sun, which is the product of the dynamo acting in its interior (e.g., Charbonneau 2020).

One of the proposed dynamo models is the Babcock-Leighton dynamo (Babcock 1961, Leighton 1964). In the Babcock-Leighton dynamo model, toroidal magnetic field is generated from poloidal field by rotational shear somewhere within the solar convection zone. This toroidal field then emerges at the solar surface in the form of tilted bipolar magnetic regions (BMRs). The BMRs are subjected to a combination of surface flows, most importantly the meridional circulation which transports the magnetic field on the surface to the poles, from where it is transported radially inwards and then towards the equator where rotational shear again converts it into toroidal fields emerging as BMRs. One prominent manifestation of the dynamo is the solar magnetic activity cycle (Hathaway 2015). Thus, emergence and evolution of BMRs, as well as the evolution of the global properties of the solar magnetic field are crucial for understanding the Babcock-Leighton mechanism, the solar cycle and the dynamo action in general. This is also essential for long term reconstructions of solar activity and irradiance (see, e.g., the reviews by Solanki et al. 2013, Usoskin 2017, and references therein).

The magnetic field on the solar surface appears in form of a great variety of magnetic structures, which vary significantly both in size and the total magnetic flux content. The largest of these structures form active regions (ARs), BMRs which feature plage regions, pores and sunspots (see e.g., van Driel-Gesztelyi and Green 2015). While sunspots have been observed and documented for centuries, smaller BMRs, without sunspots, are in fact much more frequent. Small BMRs keep emerging on the solar surface even when the Sun is comparatively quiet. The smallest of them are called ephemeral regions (ERs; Harvey and Martin 1973, Harvey 1993, Hagenaar 2001, van Driel-Gesztelyi and Green 2015) due to their short lifetimes of typically just a few hours to one day. Similarly to ARs, ERs are also observed to follow a cyclic behaviour, although the amplitude of their variability over a cycle is weaker than that of ARs (Harvey 1992, 1993, Hagenaar et al. 2003). Together with the observation by Thornton and Parnell (2011) that the emergence rate of BMRs follows a single power-law distribution over nearly seven orders of magnitude in flux ( $10^{16}$ – $10^{23}$  Mx), this suggests that ERs are part of the same dynamo process that produces ARs. The emergence rate of ERs is several orders of magnitude higher than that of ARs

so that, despite their short lifetimes and sizes, they are important for the total magnetic flux budget (Parnell et al. 2009, Thornton and Parnell 2011). It has also been shown that accounting for ERs is crucial for reconstructions of the secular variability of the solar total and open magnetic flux, as well as the irradiance (Solanki et al. 2000, 2002, Vieira and Solanki 2010, Krivova et al. 2007, 2010, 2021).

Solanki et al. (2002) were first to include the ERs into their comparatively simple model of the evolution of the solar open and total magnetic flux, which was then extended to also reconstruct the solar irradiance (Krivova et al. 2007, 2010, Vieira et al. 2011). In this original model, describing the evolution of the magnetic field using a set of ordinary differential equations, the emergence rate of BMRs on the solar surface was linearly linked to the sunspot number. The disadvantage of this assumption is that during grand minima of solar activity no magnetic flux is allowed to emerge, in contrast to the evidence coming from radionuclide and magnetospheric phenomena data (e.g., Beer et al. 1998, Fligge et al. 1999, Usoskin et al. 2001, Miyahara et al. 2004, Riley et al. 2015), as well as recent simulations (Saha et al. 2022).

Another approach to model the evolution of the Sun's magnetic field is offered by the surface flux transport models (SFTM; e.g., DeVore et al. 1985, Wang et al. 1989, Baumann et al. 2004). For example, Cameron et al. (2010) used an SFTM to simulate the evolution of the open magnetic flux, as well as the reversal times of the polar fields using the observed sunspot areas, latitudes, longitudes and tilt angles as input. Jiang et al. (2011a,b) used the same model but with semi-synthetic sunspot records constructed using statistical properties of the observed sunspot records. The model was then extended by Dasi-Espuig et al. (2014, 2016) to also reconstruct the total solar irradiance back to 1700. However, using the SFTM they could only simulate the evolution of the magnetic field in active regions, while the contribution of the ERs was then added from the simple model by Solanki et al. (2002), Vieira and Solanki (2010), Krivova et al. (2010).

The inclusion of small ARs and ERs in SFTM simulations is challenging due to technical limitations, such as the spatial and temporal resolution and the sheer number of small regions. Among the few studies including ERs is Schrijver (2001) who modelled their magnetic flux by an ensemble of ER flux concentrations instead of tracking individual regions. Those ER flux concentrations are treated separately from ARs, with their own relationships that describe the interaction between the flux concentrations when they encounter each other. Modelling the evolution of small BMRs individually remains challenging, however. Thus, there are still many unknowns surrounding the effects of ERs and small ARs on the evolution of the surface magnetic flux.

Recently, Krivova et al. (2021) have included ERs into a simpler model using the disc-integrated emergence rate of all BMRs observed by Thornton and Parnell (2011). The inclusion of ERs greatly improved the reconstruction of open and total magnetic flux during the grand minima around 1700. The next step is now to include such regions into a SFTM and therefore also take the spatial distribution of small BMRs on the solar surface into account.

The aim of this work is to study the effect of small BMRs on various solar parameters describing the magnetic field on the Sun. For this, we simulate the solar surface magnetic field with a surface flux transport model (SFTM), where emergence of BMRs is described by a power-law size distribution as observed by Thornton and Parnell (2011). The simulation results are compared to independent observations or reconstructions of

these quantities, and are discussed using analytical approximations.

The structure of the paper is as follows: In Sect. 3.3 we describe the various observational datasets used in this study. We then derive semi-synthetic data records from the relationships presented in Sect. 3.4. In Sect. 3.5 we describe the SFTM. The simulation results are presented in Sect. 3.6, and the analytical approximations are discussed in Sect. 3.7. Finally, we summarize and discuss our results in Sect. 3.8 and provide an outlook to future applications.

### 3.3 Data

The SFTM, detailed in Sect. 3.5.1, describes the evolution and transport of the magnetic field emerging on the Sun. The emergence-rates and -patterns of the field need to be provided as input to the model. To construct an input record (as described in Sect. 3.4), we use the following data sets:

- the international sunspot number version 2.0 (ISN2.0), see [Clette and Lefèvre \(2016\)](#) and references therein;
- the “official” dates of solar cycle minima and maxima as listed by the Sunspot Index and Long-term Solar Observations (SILSO) webpage<sup>1</sup>.

For comparison, we also consider the sunspot group records used in previous studies with the SFTM used here ([Baumann et al. 2006](#), [Cameron et al. 2010](#), [Jiang et al. 2011b](#), [Jiang 2020](#)), including:

- the combined Royal Greenwich Observatory (RGO) and USAF/NOAA SOON record<sup>2</sup> featuring observed sunspot group areas and locations since 1874 ([Hathaway 2015](#)). Note that a newer and more consistent composite sunspot group catalog<sup>3</sup> has been developed more recently by [Mandal et al. \(2020\)](#). Since we use the sunspot group data only to compare with earlier results, we chose to employ the RGO/SOON record for consistency, as this is the same version as used in the above mentioned SFTM studies;
- the tilt angles for the RGO/SOON sunspot groups derived by [Jiang et al. \(2011a\)](#) from Mount Wilson and Kodaikanal images ([Howard et al. 1984](#), [Howard 1991](#), [Sivaraman et al. 1993](#)).

To evaluate the simulation results, we compare the model output to the following datasets:

- the observed total magnetic flux since 1967 from Wilcox Solar Observatory (WSO), National Solar Observatory at Kitt Peak (NSO KP), and Mount Wilson Observatory (MWO); see [Arge et al. \(2002\)](#), [Wenzler et al. \(2006\)](#);
- the composite of the observed total magnetic flux since 1974 by [Yeo et al. \(2014](#), extended to 2020), derived from the Kitt Peak Vacuum Telescope (KPVT, [Livingston et al. 1976](#), [Jones et al. 1992](#)), the Michelson Doppler Imager on board of Solar and Heliospheric Observatory (SoHO/MDI, [Scherrer et al. 1995](#)) and the Helioseismic and Magnetic Imager onboard the Solar Dynamics Observatory (SDO/HMI, [Schou et al. 2012](#)). The composite is on the HMI absolute scale, with the noise level of MDI being applied to all measurements. For comparison with the MWO data, we bring the composite to the

---

<sup>1</sup><https://wwbis.sidc.be/silso>

<sup>2</sup><https://solarscience.msfc.nasa.gov/greenwch.shtml>

<sup>3</sup><http://www2.mps.mpg.de/projects/sun-climate/data.html>

MWO scale through a multiplicative factor, as suggested by [Riley et al. \(2014\)](#). The best agreement with the WSO–NSO–MWO level is found with the factor 3.7, which is close to the factor of roughly 4 found by [Riley et al. \(2014\)](#);

- the open magnetic flux reconstruction from the geomagnetic *aa*-index by [Lockwood et al. \(2022\)](#) since 1845, which is an update of the earlier versions ([Lockwood et al. 1999, 2009, 2014a](#));
- the in-situ open magnetic flux measurements since 1998 from [Owens et al. \(2017\)](#);
- the line-of-sight polar field measurements from WSO<sup>4</sup> since 1976 ([Scherrer et al. 1977, Hoeksema et al. 1983](#)).

## 3.4 Emergence of magnetic regions

### 3.4.1 Emergence rate

Combining high-resolution Hinode observations with earlier studies of magnetic field emergence on the solar surface, [Thornton and Parnell \(2011\)](#) found that the emergence rate of the magnetic regions on the Sun over a broad flux range is well represented by a power-law function:

$$N_e = \int_{\phi_1}^{\phi_2} \frac{n_0}{\phi_0} \left( \frac{\phi}{\phi_0} \right)^m d\phi, \quad (3.1)$$

where  $\phi_0 = 10^{16}$  Mx,  $n_0 = 3.14 \times 10^{-14}$  cm<sup>-2</sup> day<sup>-1</sup>,  $m = -2.69$ ,  $\phi$  is the magnetic flux of the region and  $\phi_1$  and  $\phi_2$  are the upper and lower integration limits. Based on studies by [Harvey \(1993\)](#) (H93) and [Harvey and Zwaan \(1993\)](#), [Krivova et al. \(2021\)](#) have argued that the slope  $m$  of the distribution varies with solar activity. They described this change by a function of the sunspot number, SN, as follows:

$$m(\text{SN}) = m_1 - \left( \text{SN}_1^p - \text{SN}^p \right) \frac{m_1 - m_2}{\text{SN}_1^p - \text{SN}_2^p}, \quad (3.2)$$

where  $\text{SN}_1 = 217$ ,  $\text{SN}_2 = 17$ ,  $m_1 = -2.5954$ ,  $m_2 = -2.7846$  and  $p = 0.059$  for the international sunspot number ISN2.0 used here. Note that [Krivova et al. \(2021\)](#) used the notation  $\alpha$  instead of  $p$ .

In this work, we consider several populations of BMRs, depending on their sizes (or magnetic flux content), see also [Krivova et al. \(2021\)](#). [van Driel-Gesztelyi and Green \(2015\)](#) define large active regions (ARs) containing sunspots as regions with total flux higher than  $5 \times 10^{21}$  Mx, small ARs forming only pores as regions with fluxes in the range  $10^{20} - 5 \times 10^{21}$  Mx, and ephemeral regions (ERs) as regions with fluxes  $3 \times 10^{18} - 10^{20}$  Mx. These boundaries are rather approximate. H93 classify the regions based primarily on their area, with the transition from ERs to ARs lying between 2.5 and 3.5 square degrees. The latter corresponds to a magnetic flux of roughly  $\geq 4 \times 10^{20}$  Mx. The smallest ERs considered by H93 correspond to about  $3 \times 10^{18}$  Mx. We set the lower flux limit for large ARs (LMR, for Large Magnetic Regions hereafter) to  $3 \times 10^{21}$  Mx, which makes the number of emerging LMRs consistent with the number of sunspot groups in the RGO/SOON record. This allows a direct comparison of the simulation results based on the synthetic

<sup>4</sup><http://wso.stanford.edu>

sunspot records (see Sect. 3.4) and those using direct observations. Since regions with magnetic flux close to the upper limit are extremely rare, if there are any at all, the exact value is not important, and we set it to  $10^{23}$  Mx. To study the effect of smaller BMRs on the various magnetic-field observables, we include in the simulations all regions with lifetimes of  $\geq 1$  day, which is the temporal resolution of the SFTM; see Sec. 3.5.1. The corresponding lower flux limit of  $2 \times 10^{20}$  Mx is slightly lower than the AR limit in H93 and Krivova et al. (2021). We will refer to the regions with fluxes above this limit as AMR (All Magnetic Regions). Following H93 Krivova et al. (2021), we define ERs as regions with fluxes between  $3 \times 10^{18}$  Mx and  $4 \times 10^{20}$  Mx. By including the regions as small as  $2 \times 10^{20}$  Mx in this work, we consider all BMRs down to the biggest of the ERs.

We will refer to the smallest regions included in our model with fluxes between  $2 \times 10^{20}$  Mx and  $3 \times 10^{21}$  Mx as SMR (Small Magnetic Regions). Even smaller regions emerge on the solar surface, however a significant portion of their magnetic flux is believed to come from a separate small-scale dynamo and is unlikely to contribute to the Sun’s polar fields, open flux or toroidal flux loss, but it will affect the total amount of flux on the solar surface. We call the small ERs and even smaller internetwork fields not included in the model SSEs (Small-Scale Emergences). Following Parnell et al. (2009), Thornton and Parnell (2011), Krivova et al. (2021) the lower flux limit of SSEs is set to  $10 \times 10^{16}$  Mx. The observations of small ERs by H93 however are taken into account when constructing the synthetic input record as described in Sect. 3.4. The definitions of the BMR populations and the abbreviation we use for them are summarized in Tab. 3.1.

Table 3.1: Different BMR populations considered in this work.

Population	Abbreviation	Magnetic flux range [Mx]
Ephemeral regions, H93	ERs	$3 \times 10^{18} - 4 \times 10^{20}$
Active regions, H93	ARs	$4 \times 10^{20} - 1 \times 10^{23}$
All (modelled) magnetic regions	AMR	$2 \times 10^{20} - 1 \times 10^{23}$
Large magnetic regions	LMR	$3 \times 10^{21} - 1 \times 10^{23}$
Small magnetic regions	SMR	$2 \times 10^{20} - 3 \times 10^{21}$
Small scale emergences	SSEs	$1 \times 10^{16} - 2 \times 10^{20}$

**Notes.** H93 refers to the definition used by Harvey (1993), on whose observations we rely.

### 3.4.2 Emergence patterns

The distribution of the newly emerging regions on the surface of the Sun generally depends on the size of the regions, as well as on the phase and the strength of the solar cycle (Harvey 1993, Jiang et al. 2014b, Hathaway 2015, van Driel-Gesztelyi and Green 2015). We build our input record of the spatial distribution of the emerging BMRs as a function of latitude and solar activity on the statistical studies by Jiang et al. (2011a) (J11) and Jiang (2020) (J20). J11 used the RGO/SOON sunspot group data, the Mount Wilson and Kodaikanal sunspot tilt angle records and the GSN to study the mean emergence latitude and its scatter, as well as the mean tilt angles of the regions between 1874 and 1976 (cycles 12 to 20). J20 have updated the relationships by using ISN2.0 over cycles 12 to 21.

For our purpose, we partly revise and extend their relationships as described below.

### 3.4.2.1 Emergence latitudes

Using the records of sunspot observations, J11 and J20 divided each solar cycle into 30 equal phase bins between adjacent solar minima and calculated the mean emergence latitude for all cycles and phase bins. For the statistical analysis, they excluded the first and the last 3 bins to avoid distortion of the results due to an overlap between regions from two adjacent cycles emerging at high and low latitudes. They then derived a relationship between cycle phase " $i$ " of cycle " $n$ " and the mean latitude through a second order polynomial fit:

$$\lambda_{n,J11}^i [^\circ] = (26.4 - 34.2 i + 16.1 i^2) \frac{\lambda_n}{\langle \lambda_n \rangle_{12-20}}, \quad (3.3)$$

where  $0 < i < 1$  is the fraction of the solar cycle duration between adjacent minima,  $\lambda_n = 12.03 + 0.0015 S_{\max}$  is the average latitude for cycle  $n$  for ISN2.0 (J20),  $\langle \lambda_n \rangle_{12-20} = 14.6^\circ$  is the average over all cycles, and  $S_{\max}$  is the maximum of the 13-month running average of the ISN2.0. The standard deviation of the latitude distribution is calculated as:

$$\sigma_{J11}^i = (0.14 + 1.05 i - 0.78 i^2) \lambda_{J11}^i, \quad (3.4)$$

where  $\lambda_{J11}^i = 26.4 - 34.2 i + 16.1 i^2$ . Due to the removal of the bins at the beginning and the end of the cycle for the fits, the relationships by J11 and J20 do not account for the cycle overlap and thus potentially different parameters for the declining and rising phases of cycles (see Sec 3.4.3). For example, according to Eq. 3.3, the mean latitude of the declining cycle would increase again after the cycle minimum, which is in contrast to observations. We consider each cycle individually, accounting for their overlap (see Sect. 3.4.3). Hence we replace the relationship given by Eq. 3.3 with an exponential fit to it, which steadily decreases towards zero after the cycle minimum:

$$\lambda_n^i [^\circ] = (31 \cdot 0.35^i - 5) \frac{\lambda_n}{\langle \lambda_n \rangle_{12-20}}. \quad (3.5)$$

The mean latitude over one (extended) cycle described by Eq. (3.5) is shown in Fig. 3.1a, together with the original relationship from J11 and J20 for comparison.

The latitude scatter of large, spot-containing ARs from J11 and J20 (Eq. 3.4) is shown in Fig. 3.1b by the black line. While decreasing after cycle maximum, it shows an opposite behaviour at the beginning of a cycle. For small BMRs during a cycle onset at high latitudes this would lead to no scatter. Instead, to extend the relationship to earlier cycle phases, we rely on the finding by Solanki et al. (2008) that the latitude scatter of sunspots is proportional to the mean latitude:

$$\sigma_{\text{lat,ARs}} [^\circ] = 0.4 \lambda_n^i [^\circ] + 1. \quad (3.6)$$

This roughly follows the latitude scatter of J11 and J20 over the declining phase of the cycle, but keeps the scatter steadily decreasing from the cycle's dawn to its end; see the red curve in Fig. 3.1b.

The studies by J11, J20 and Solanki et al. (2008) have only considered large ARs with sunspots. However the latitude scatter also depends on the size of the regions. As has been

observed by [Harvey and Martin \(1973\)](#), [Harvey \(1993\)](#), [Hagenaar et al. \(2003\)](#) the latitude scatter of ERs is significantly larger than that of ARs. In particular, H93 found that for ERs the standard deviation of their latitude distribution was roughly  $20^\circ$  (as estimated from Fig. 5 in her Chapter 5), while it was around  $5 - 10^\circ$  for ARs. The latter is roughly consistent with the latitude distribution described by Eq. (3.6) above. We took the value of  $\langle \sigma_{\text{lat,LMR}} \rangle = 6.5^\circ$ , which is the mean returned by Eq. (3.6) over the solar cycle, as the reference for LMRs, compared to the  $20^\circ$  for ERs. We then derived a relationship for the cycle-mean latitude scatter as a function of BMR size. To be consistent with observations, the scatter should change little for LMRs, while increasing faster for smaller regions. We assumed a log-square function, which fits this purpose well. The relationship was constrained such that the mean latitude scatter of ERs and LMRs was preserved to agree with H93's observations. The function was then normalized by dividing by  $\langle \sigma_{\text{lat,LMR}} \rangle$ , which gives a factor of  $\sim 1$  for LMRs, and the best-fit was:

$$f_{\text{lat}} = 4.4 - 0.64 \ln(\phi^*) + 0.029 \ln(\phi^*)^2, \quad (3.7)$$

where  $\phi^*$  is the magnetic flux of the region in units of [ $10^{18}$  Mx]. The normalized size-dependent latitude scatter from Eq. (3.7) is shown in Fig. 3.1c. By multiplying the cycle phase-dependent latitude scatter from Eq. (3.6) with the normalized size-dependent latitude scatter from Eq. (3.7), we obtained the latitude scatter for all regions and cycle phases:

$$\sigma_{\text{lat}} [^\circ] = f_{\text{lat}} \sigma_{\text{lat,ARs}}. \quad (3.8)$$

### 3.4.2.2 Tilt angles

Following J11 and J20, we assume that the mean tilt angle ( $\alpha_m$ ) of a BMR, i.e. the angle between the line connecting the two polarities and the equator, is proportional to the square root of the latitude  $\lambda$ :

$$\alpha_m = T_n \sqrt{|\lambda|}. \quad (3.9)$$

The proportionality factor  $T_n = 1.72 - 0.0021 S_{\text{max}}$  (for ISN2.0; J20) decreases for stronger cycles, consistent with the study by [Dasi-Espuig et al. \(2010\)](#), who found that stronger solar cycles tend to have smaller average tilt angles.

The tilt angle scatter was not analysed by J11 and J20. As first shown by H93, the tilt angle scatter strongly depends on the region size, being small for large ARs and increasing for smaller BMRs. The tilt angles of smallest ERs are rather random. A number of more recent studies analysed the distribution of AR tilt angles, also using modern magnetograms (e.g., [Tlatov et al. 2010](#), [Stenflo and Kosovichev 2012](#), [Jiang et al. 2014a](#), [Wang et al. 2015](#), [Jha et al. 2020](#), [Schunker et al. 2020](#)). The tilt angle distribution of the largest ARs generally shows a standard deviation of  $10 - 15^\circ$ , which increases to  $20 - 30^\circ$  for small ARs. In particular, [Schunker et al. \(2020\)](#) studied the standard deviation of the tilt angles of a sample of 153 emerging ARs with a median magnetic flux of  $4.6 \times 10^{21}$  Mx. Four days after emergence, they found a standard deviation of  $30^\circ$  for the tilt angles of all regions below the median value,  $25^\circ$  for the entire sample and  $18^\circ$  for all regions above the median. Although the magnetic flux of the smallest regions is not specified in [Schunker et al. \(2020\)](#), from Eq. (3.1) we find that the median value  $4.6 \times 10^{21}$  Mx would roughly correspond to the magnetic flux range from  $10^{21}$  Mx to  $10^{23}$  Mx. For ERs, we rely on the

observations of H93 and [Hagenaar \(2001\)](#), who found that around 95% of ARs obeyed Hale’s polarity law while only about 60% of ERs did so. We use these numbers as a guidance for our model and assumed that the tilt scatter follows a Gaussian distribution with a variable standard deviation dependent on the region size. In this model, a BMR is considered to have an anti-Hale orientation if the tilt angle deviates by more than  $\pm 90^\circ$  from the mean. Using the results from H93 and [Hagenaar \(2001\)](#) we estimate a standard deviation of  $107^\circ$  for the tilt angles of ERs and  $46^\circ$  for ARs. Together with the constraints from [Schunker et al. \(2020\)](#), this gives us a total of five magnetic flux ranges with the corresponding estimates of the standard deviation, summarized in Tab. 3.2. Assuming a log-square relationship between the region size and the tilt angle scatter, we find the following function to fit to these constraints:

$$\sigma_{\text{tilt}}[^\circ] = 155 - 22.2 \ln(\phi^*) + 0.8 \ln(\phi^*)^2. \quad (3.10)$$

Table 3.2 lists the values of the tilt scatter in the five flux ranges derived from observations and returned by the fit, and Fig. 3.1d shows the tilt scatter for the entire flux range.

Table 3.2: The mean standard deviations of the tilt angles of the emerging BMRs in our model.

<b>Magnetic flux range [Mx]</b>	<b>Observed <math>\sigma_{\text{tilt}}</math></b>	<b>Fitted <math>\sigma_{\text{tilt}}</math></b>
$3.0 \times 10^{18} - 4.0 \times 10^{20}$	$107^\circ$ (60.0%)	$108^\circ$ (59.5%)
$4.0 \times 10^{20} - 1.0 \times 10^{23}$	$46^\circ$ (95.0%)	$37^\circ$ (98.5%)
$1.0 \times 10^{21} - 4.6 \times 10^{21}$	$30^\circ$ (99.7%)	$33^\circ$ (99.4%)
$1.0 \times 10^{21} - 1.0 \times 10^{23}$	$25^\circ$ (100%)	$28^\circ$ (99.9%)
$4.6 \times 10^{21} - 1.0 \times 10^{23}$	$18^\circ$ (100%)	$17^\circ$ (100%)

**Notes.** Listed are: the magnetic flux ranges, the approximate estimates of the standard deviation derived from observations ([Harvey 1993](#), [Schunker et al. 2020](#), see text for details) and values returned by the best-fit approximation to these values, see Eq. (3.10). The values in the brackets are the percentage of regions that obey Hale’s law.

### 3.4.2.3 Nesting

Sunspots show a tendency to emerge within the so-called activity nests, that is new magnetic regions tend to emerge in the vicinity of the existing regions more often than at random locations (see, e.g., [Bumba and Howard 1965](#), [Gaizauskas et al. 1983](#), [Castenmiller et al. 1986](#), [Bai 1988](#)). The longitude distribution of BMRs is particularly important for the reconstruction of the open magnetic flux as it has been shown to be dominated by low-order multipoles which are strongly dependent on the randomness of the longitude distribution ([Cameron et al. 2010](#)). It has further been observed ([Berdyugina and Usoskin 2003](#), [Zhang et al. 2007](#)) that activity nests preferably form in two persistent longitudes in opposite hemispheres separated by  $180^\circ$ . J11 argued that nesting can be accounted for by a linear combination of the magnetic field,  $B_{\text{com}}$ , of two separate simulation runs: one with purely random longitudes,  $B_{\text{ran}}$ , and one with all regions being ordered at  $90^\circ$  and  $270^\circ$  longitudes in the northern and southern hemisphere, respectively,

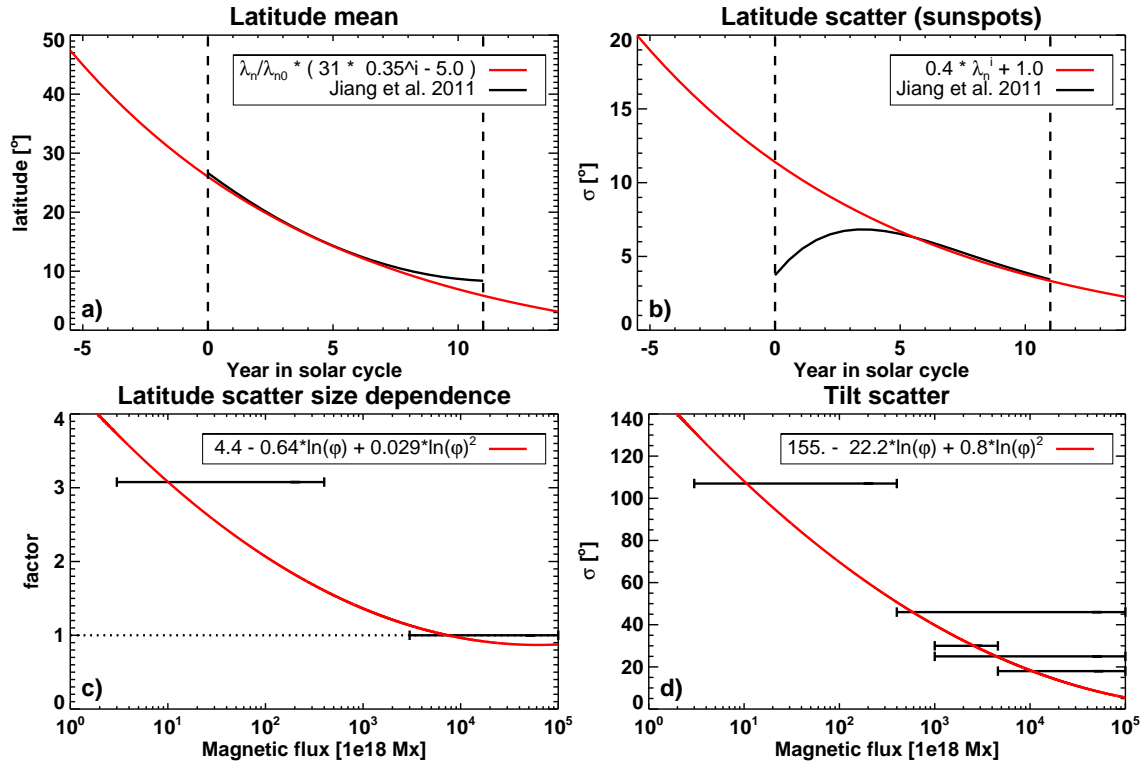


Figure 3.1: Parameters describing the spatial distribution of emerging BMRs in our model (red) and as originally derived by [Jiang et al. \(2011a\)](#) (black, only in panels a and b). (a) The mean latitude and (b) the latitude scatter of spot-containing LMRs as a function of the solar cycle phase. (c) The correction factor to the latitude scatter depending on the magnetic flux content of a BMR and (d) the tilt angle scatter as a function of the total magnetic flux enclosed by a BMR. The vertical dashed lines in panels a) and b) mark the formal beginning and the end of the solar cycle (that is cycle minima). The horizontal bars in panels c) and d) mark the magnetic flux intervals from the fit, with their y-value being the observational mean value within the flux range; see also [Table 3.2](#).

$B_{\text{ord}}$ :  $B_{\text{com}} = (1 - c)B_{\text{ran}} + cB_{\text{ord}}$ . To describe the degree of nesting required to reproduce the open magnetic flux from [Cameron et al. \(2010\)](#), they introduced the parameter  $c$ , which was found to be  $c = 0.15$ . Since we reconstruct the open magnetic flux from the magnetograms with the same model as J11 (see [Sect. 3.6.2](#)) we adopt their approach.

### 3.4.3 Cycle overlap

It is well known that the magnetic activity of a given solar cycle  $n$  starts at high latitudes ( $\sim 50^\circ$ ) several years before the end of the previous cycle  $n - 1$ , apparently soon after the polar field reversal (see, e.g., [Legrand and Simon 1981](#), [Harvey 1993](#), [Wilson et al. 1988](#), [Tlatov et al. 2010](#), [Hathaway 2015](#), and references therein). The first regions of a new cycle are typically small. The probably most complete study of BMR emergence available is that by H93, who analysed the emergence of regions as a function of their sizes, latitude and cycle phase in a systematic way. By analysing cycles 14–22, H93 noticed that the emergence onset of ERs started shortly after the polar field reversal,  $\sim 0.5 - 1.5$  years

after the maximum of the activity cycle. It is worth noting, however, that due to limited spatial and temporal resolution of observations, small BMRs at high latitudes could easily escape notice. Thus, smaller regions might start emerging even earlier, possibly right after the polar field reversal.

The first (small) ARs are observed 2 to 4 years before the solar minimum or roughly 2 years after the polar field reversal, while larger ARs with sunspots emerge another 0.5–1.5 years later (see also the review by Hathaway 2015, and references therein). BMRs associated with cycle  $n$  also continue emerging for roughly two years after the “formal” beginning of the next cycle  $n + 1$  (that is the minimum between cycles  $n$  and  $n + 1$ ) close to the equator. This overlap, between what have been called extended activity cycles (Wilson et al. 1988), has important implications for the evolution of the solar magnetic flux. For example, it has been shown that such an overlap leads to a secular variability in the solar open and total magnetic flux (Solanki et al. 2000, 2002), which also has implications for reconstructions of past irradiance variations (Krivova et al. 2007, 2010, Wu et al. 2018a).

To take the solar cycle overlap into account, we need to split the emergent BMRs between the subsequent cycles,  $n$  and  $n + 1$ . The simplest way of doing this would be to take a progressively large fraction of the total emerging regions (see Eq. 3.1) and place them at higher latitudes. However, it is important to remember that the size (or magnetic flux) distributions of the emerging regions belonging to the ongoing cycle  $n$  and the following, just starting, cycle  $n + 1$  differ. At the onset of a new cycle (here  $n + 1$ ), there are only few small regions emerging at high latitudes. At the same time, the ongoing cycle  $n$  is still close to its activity maximum and a lot of flux emerges in form of large ARs containing sunspots, see Eqs. (3.1–3.2). If we were to attribute a random sample of regions to the new cycle, we would greatly overestimate the amount of large, spot-containing, ARs at high latitudes. Therefore, we need to account for different slopes of the power law in Eq. (3.1) for the two cycles, such that the emergence rate for the new cycle matches the observed size distribution at low solar activity. To do this, we took observations by H93 as well as RGO/SOON sunspot group data as guidance and proceeded as described below, see also the illustration in Fig. 3.2.

As suggested by observations, we assumed that cycle  $n - 1$  ends 2 years after the minimum between cycles  $n - 1$  and  $n$  (in Fig. 3.2, activity minima are marked by vertical dotted lines). From this instant until the maximum of cycle  $n$  and the polar field reversal (shaded area in Fig. 3.2), only BMRs of cycle  $n$  emerge on the Sun. During this period, the exponent  $m_n$  in Eq. (3.1) is determined directly from the SN as given by Eq. (3.2). Shortly after the field reversal, cycle  $n + 1$  starts. The exponent  $m_{n+1}$  is infinitely low at this time but starts growing progressively until two years after the minimum between cycles  $n$  and  $n + 1$ , that is until the end of the *extended* cycle  $n$  (in Fig. 3.2, this period of time is left unshaded). From then until the maximum of cycle  $n + 1$  the exponent  $m_{n+1}$  is again defined by the instantaneous SN from Eq. (3.2). Thus, we need to describe the change of the exponent  $m_{n+1}$  between the maximum and the end of cycle  $n$  (that is within the shaded area). For this, we use the following observational constraints.

Firstly, at the minimum between cycles  $n$  and  $n + 1$  we split the observed SN equally between the two cycles. Secondly, by analysing emergence latitudes of sunspot groups in the RGO/SOON record (which correspond to our LMRs) over cycles 12–24, we found that first LMRs of a new cycle  $n + 1$  emerged on average about 1.5 years before its “formal” start at solar minimum  $t_{\min,n+1}$ , in good agreement with H93 and Hathaway (2015).

The most extreme cases were  $-3.3$  (cycle 21) and  $-0.3$  years (cycle 19). Within one year before a minimum on average nine regions emerged, which we consider to roughly correspond to an emergence rate of  $\sim 1/\text{month}$  or  $12/\text{year}$ . The emergence rate drops to roughly  $2/\text{year}$  and  $0.5/\text{year}$  in the time intervals between  $1 - 2$  and  $2 - 3$  years before the minimum, respectively. Thirdly, some BMRs of the new cycle,  $n + 1$ , emerge even earlier, that is more than  $2-3$  years before the minimum (e.g., H93). Normally, however, these are smaller regions, corresponding to our SMRs. To put constraints on the emergence of such regions prior to activity minimum, we relied on observations by H93, in particular her summary of the properties of 978 ARs from cycle 21 (also partly including regions from cycles 20 and 22, see Chapter 4 in H93), as well as her analysis of cycles 14–22 based on observations from various sources (her Chapter 11, see also Harvey 1992). Using these data, we estimated the emergence rate of SMRs to be about  $1/\text{year}$  to  $1/\text{month}$  roughly between 4 and 2 years prior to the minimum.

Finally, observations suggest that ERs start emerging at high latitudes shortly after the polar field reversal (Wilson et al. 1988, Harvey 1993, Tlatov et al. 2010, McIntosh et al. 2014). Being extremely difficult to observe, the emergence rate of ERs at the cycle onset is highly uncertain. Nevertheless, it is clear that the period shortly after the cycle maximum and field reversal, is dominated by regions from the ongoing cycle, and thus the fraction of BMRs of the new cycle is negligible. We set a rather arbitrary limit of one ER for the first year after the maximum. We note though that, being extremely low the exact value of the emergence rate of new ERs at this time has no effect on our results.

Table 3.3: Observational constraints on the emergence rate and the corresponding exponent  $m$  for BMRs of a newly starting cycle for different size ranges.

(1) Size	(2) Time [year] $+t_{\min,n+1}$ <sup>a</sup>	(3) Emerg. rate [year <sup>-1</sup> ]	(4) $m$
ERs	$t_{\max,n} + (1 \pm 1)$	0.3 – 12	$-5.4 \pm 0.3$
SMRs	$-(3 \pm 1)$	1 – 12	$-3.4 \pm 0.1$
LMRs	$-(2 \pm 1)$	0.5 – 2	$-3.15 \pm 0.05$
LMRs	$-(1 \pm 1)$	2 – 12	$-3.0 \pm 0.1$
all BMRs	0	SN/2	$m(\text{SN}/2)$
all BMRs	+2	SN	$m(\text{SN})$

**Notes.** Listed are: (1) type of features; (2) approximate time, relative to the activity minimum, when such regions belonging to the next cycle start appearing, given as mean value with uncertainty range; (3) maximum and minimum emergence rates observed within that time period; (4) power-law exponent given as mean value with uncertainty range.

<sup>a</sup> Except 1st row, where time is linked to the previous maximum.

Table 3.3 summarises observational constraints used by us to split the emergence rate of BMRs between two overlapping cycles,  $n$  and  $n + 1$ , as well as the derived values of the exponent  $m_{n+1}$  during the respective phases of the activity cycle. To obtain the power-law exponent of the developing cycle throughout the overlap period, we fitted an exponential function to these points. Since estimates derived from observations are rather uncertain,

we gave a higher weight to the last two points (that is the equal contribution from the two cycles at activity minimum and no “old” regions two years after the minimum). This fit was performed for each cycle separately. As an example, panels b and c of Fig. 3.2 show the fit for cycles 21 and 22.

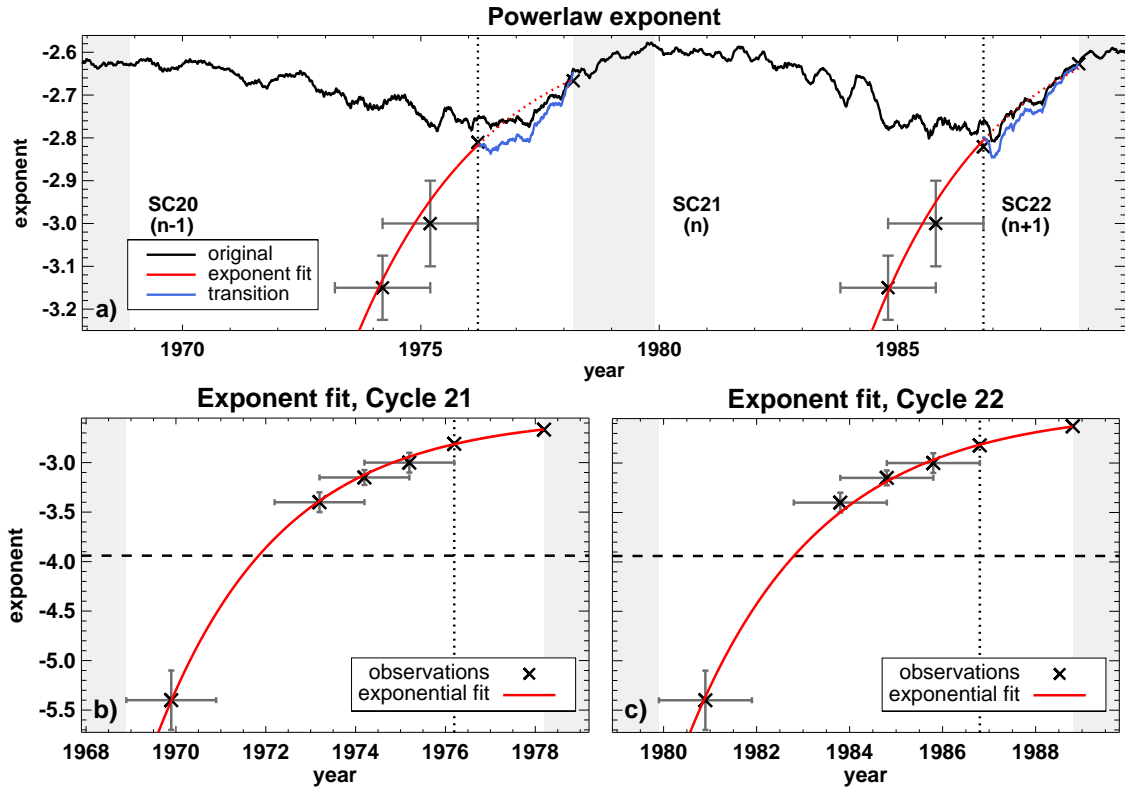


Figure 3.2: (a) The power-law exponent based on the total SN (black), and calculated from the two transition models: The exponent fit in red and the linear transition model in blue. Only the solid lines are used for the calculation, the transition between models is at solar minimum (dotted vertical line). (b) and (c) Exponential fit of the power-law exponent of Cycles 21 and 22 in the overlap period with Cycles 20 and 21, respectively. The "x" symbols are the estimated exponents from Tab. 3.3, based on the observations by Harvey (1993) and our analysis of the RGO/SOON record. The gray crosses around the points are the uncertainty ranges in x and y direction. The horizontal line is the power-law exponent  $m = -3.94$  that corresponds to a SN of zero.

The power-law exponent from the total instantaneous SN ( $m_{\text{tot}}$ , black line), as well as the exponent fit of the new cycle  $n + 1$  ( $m_{\text{exp},n+1}$ , red line) for cycles 21 and 22 are shown in Fig. 3.2a. Although the exponent fit follows the trend of the new cycle  $n + 1$  nicely, the exponent fit after minimum (red dashed) is occasionally higher than  $m_{\text{tot}}$ . To account for the fact that the emergence rate for the new cycle  $n + 1$  cannot be higher than the total emergence rate, we implemented a simple transition (blue line) from  $m_{\text{exp},n+1}$  at activity minimum to  $m_{\text{tot}}$  at the end of cycle  $n$ . For this, we calculated the ratio between  $m_{\text{exp},n+1}$  and the 13-months mean of  $m_{\text{tot}}$  at activity minimum  $n + 1$  and linearly reduced that ratio to unity, two year after the minimum. The power-law exponent of the new cycle  $n + 1$  after minimum was then obtained by multiplying  $m_{\text{tot}}$  with this factor. Just like the exponent fit,

this linear transition was calculated separately for each cycle. The emergence of the new cycle  $n + 1$  is then given by the exponent fit (solid red) before minimum and the linearly-weighted transition (solid blue) after the minimum. To ensure that the observed total emergence rate of BMRs given by Eq. (3.1) is preserved at any given time we calculated the emergence rate for the ongoing cycle  $n$  during the overlap period as the difference between the total emergence and the emergence of the new cycle.

### 3.4.4 Final synthetic input records

We used four different types of records as input to the simulations. From the ISN2.0 and the relationships derived in Sect. 3.4.2 we generated input records for AMR (all (modelled) magnetic regions), LMR (large magnetic regions) and SMR (small magnetic regions; see Table 3.1). Thereby, the LMR record is obtained by removing all smaller regions from the counterpart AMR record, thus large active regions are the same in both sets. In the same way the SMR records is obtained by removing all LMRs from the AMR record.

For each of these input types (AMR, LMR and SMR), 100 independent realisations were generated to allow an error estimate, see Sect. 3.5.4. To visualise these input records, Fig. 3.3 shows a butterfly diagram for one realisation. The colors indicate the monthly magnetic flux emergence rate within each  $2^\circ$  latitude bin; see the description in the figure caption. In addition, we use the RGO/SOON sunspot group record to compare the simulation results with those from Cameron et al. (2010). This test is needed due to the modifications we applied to their SFTM, as described in Sect. 3.5.1.

## 3.5 Model

### 3.5.1 Surface flux transport model

We simulated the evolution of the large-scale radial magnetic field on the solar surface with a surface flux transport model (SFTM, see, e.g., DeVore et al. 1984, 1985, Wang et al. 1989). An SFTM describes the evolution of the radial magnetic field  $B_r(\theta, \phi, t)$  on the solar surface with time,  $t$ , as a function of the heliocentric latitude  $\theta$  and longitude  $\phi$ . The flux emerging at the surface in the form of BMRs is represented by the source term  $S(\theta, \phi, t)$ . Upon emergence, the flux is subject to the action of the differential rotation  $\Omega(\theta)$ , the poleward meridional flow  $v(\theta)$  (Babcock 1961) and the turbulent surface diffusivity  $\eta_h$ . The surface diffusivity is a result of convective plasma flows near the solar surface, in particular the supergranulation (Leighton 1964).

The original version of the SFTM used in this study was developed by Baumann et al. (2004). The evolution of the radial component of the magnetic induction is described as:

$$\begin{aligned} \frac{\delta B_r}{\delta t} = & -\Omega(\theta) \frac{\delta B}{\delta \phi} - \frac{1}{R_\odot \sin(\theta)} \frac{\delta}{\delta \theta} \left[ v(\theta) B_r \sin(\theta) \right] \\ & + \frac{\eta_h}{R_\odot^2} \left[ \frac{1}{\sin(\theta)} \frac{\delta}{\delta \theta} \left( \sin(\theta) \frac{\delta B_r}{\delta \theta} \right) + \frac{1}{\sin^2(\theta)} \frac{\delta^2 B_r}{\delta \phi^2} \right] \\ & + S(\theta, \phi, t) - D_r(\eta_r). \end{aligned} \quad (3.11)$$

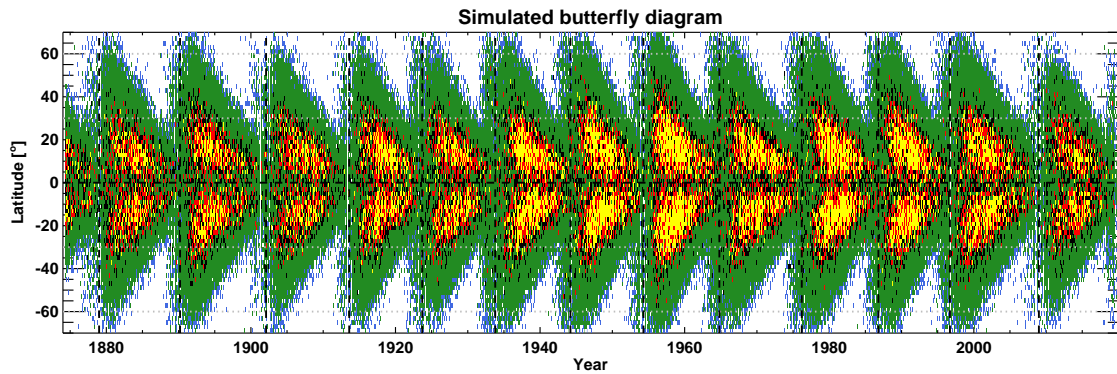


Figure 3.3: Butterfly diagram for one realisation of the synthetic BMR input record. Different colours encode magnetic flux emerging in BMRs within one-month periods over  $2^\circ$  latitude bins. Yellow, red and black are used to show only large ARs, with yellow for bins with  $> 1.5 \times 10^{22}$  Mx flux emerged in LMRs per month and latitude bin, red for bins with  $6 \times 10^{21} - 1.5 \times 10^{22}$  Mx which roughly corresponds to 2-5 small LMRs, and black for bins with  $< 6 \times 10^{21}$  Mx or 2 small LMRs. Green and blue show only SMRs, with  $> 4 \times 10^{20}$  Mx and  $< 4 \times 10^{20}$  Mx (or 2 small ARs) per month and bin, respectively. Thus, yellow, red and black roughly correspond to emergence of regions directly represented by sunspot records, such as RGO/SOON used in previous versions of the model, while green and blue mark BMRs previously not taken into account directly (that is their contribution was eventually accounted for by leveling up the model output to the observed magnetic flux, see Sect. 3.5.1). We emphasise that a lot of small ARs also emerge during more active periods but green and blue bins are hidden under yellow, red and black ones during such times. The vertical dashed lines mark cycle minima.

The additional decay term  $D_r(\eta_r)$  describes the radial decay of magnetic flux. It accounts for the 3D decay modes that cannot be captured by the 2D model and was first introduced by [Baumann et al. \(2006\)](#) to avoid a secular drift of the polar fields and obtain regular field reversals. We used the differential rotation profile introduced by [Snodgrass \(1983\)](#):

$$\Omega(\theta) = 13.38 - 2.30 \cos^2(\theta) - 1.62 \cos^4(\theta) [\text{deg day}^{-1}]. \quad (3.12)$$

The meridional flow profile was taken from [van Ballegooijen et al. \(1998\)](#):

$$v(\theta) = \begin{cases} v_0 \sin(\pi\lambda/\lambda_0) & [\text{m s}^{-1}] \quad |\lambda| \leq \lambda_0 = 75^\circ \\ 0 & \text{otherwise.} \end{cases} \quad (3.13)$$

The model parameters were taken to be the same as in [Cameron et al. \(2010\)](#) and [Jiang et al. \(2011b\)](#), with  $\eta_h = 250 \text{ km}^2 \text{ s}^{-1}$  and  $v_0 = 11 \text{ m s}^{-1}$ . Following [Jiang et al. \(2011b\)](#), we also used the value of  $\eta_r = 25 \text{ km}^2 \text{ s}^{-1}$  for the weak radial diffusion.

Following [van Ballegooijen et al. \(1998\)](#), emerging BMRs were represented by two Gaussian-like polarity patches with angular separation  $\Delta\beta$ :

$$B_r^\pm(R_\odot, \theta, \phi) = B_{\text{amp}} \exp\left\{-\frac{2[1 - \cos\beta_\pm(\theta, \phi)]}{\delta_{\text{init}}^2}\right\}, \quad (3.14)$$

where  $B_{\text{amp}}$  is the initial amplitude of the magnetic flux density of the polarity patches,  $\beta_\pm(\theta, \phi)$  are the heliocentric angles of the positive and negative polarity centres ( $\theta_\pm, \phi_\pm$ )

and  $\delta_{\text{init}} = 0.4\Delta\beta$  is the initial width of the polarity patches. This is different from the model by [Baumann et al. \(2004\)](#) and the subsequent versions by [Cameron et al. \(2010\)](#) and [Jiang et al. \(2011b\)](#), who injected the BMRs at a later stage of their development, when the polarity patches have diffused to the width of  $\delta_0 = 4^\circ$  and the initial amplitude has been reduced by the factor  $(\delta_{\text{init}}/\delta_0)^2$ . For small BMRs, this means that they were injected into the SFTM after several e-folding lifetimes and their contribution was essentially missed. This was accounted for by the (time-independent) free parameter  $B_{\text{max}}$ , which was adjusted by comparing the computed total magnetic flux with observations. Having the initial shape described by Eq. (3.14) allows a more realistic description of small ERs, where the entire decay period of each BMR regardless of its size, starting from the time of its maximum development is included in the simulations.

We fixed the amplitude factor  $B_{\text{amp}}$  by comparing the decay rate of BMRs in the SFTM with their e-folding lifetimes derived from observations. Following [Krivova et al. \(2021\)](#), we estimated the lifetimes by dividing the instantaneous magnetic flux present in BMRs on the solar surface as observed by [Parnell et al. \(2009\)](#) by the BMR flux emergence rate derived by [Thornton and Parnell \(2011\)](#). The best agreement between the decay rate in SFTM and the estimated observed lifetimes was found for the value  $B_{\text{amp}} = 1000\text{G}$ , with the magnetic flux content in BMRs of different sizes after one lifetime being within  $\pm 20\%$  of the expected value.

The initial width of the polarity patches in Eq. (3.14) is linearly related to the angular separation between them. Hence, we can obtain the relationship between  $\Delta\beta$  and the initial flux of the BMR  $\phi_{\text{BMR}}$  (which is the sum of the unsigned fluxes from both polarity patches) directly, through numerical integration:

$$\Delta\beta = 8.5 \cdot 10^{-10} \sqrt{\frac{\phi_{\text{BMR}}}{B_{\text{amp}}}}. \quad (3.15)$$

The smallest BMRs are initially too narrow to be resolved by the SFTM, which has a spatial resolution limit of  $4^\circ$ . The most straightforward approach would be to simply increase the spatial resolution. However, this is computationally very costly, as this is tied to a spherical harmonics decomposition needed to accurately calculate the effects of the radial diffusion and the meridional flow. Thus the total computing time increases exponentially with the highest order of the spherical harmonics. Fortunately, small BMRs are very compact during the initial stage of the emergence process and the effects of the meridional flow and the differential rotation are small in comparison to the turbulent diffusion which is faster for smaller regions. Assuming that the early development of small regions is dominated by the turbulent diffusion allows us to separate such regions from the primary magnetogram (and the spherical harmonics decomposition) and account for the effect of turbulent diffusion alone in a separate secondary magnetogram (without spherical harmonics), until a region has diffused to a width that can be resolved by the SFTM, whereupon it is added to the primary magnetogram. Once the regions are added to the main magnetogram, their shape and treatment are identical to the SFTM versions by [Baumann et al. \(2004\)](#), [Cameron et al. \(2010\)](#), [Jiang et al. \(2011b\)](#), except that they first appear in the main magnetogram with an up to one Carrington rotation delay (the time it would take for a point source to diffuse to a width of  $4^\circ$  in our model). At each timestep, the solar quantities are derived from the sum of the primary and the secondary

magnetograms. With this approach, the total magnetic flux of the BMRs is preserved in the simulation.

### 3.5.2 Open flux calculation / CSSS

The SFTM only calculates the magnetic field on the solar surface. To extrapolate it into the heliosphere and calculate the open magnetic flux, we employ a current sheet source surface model (CSSS) (Zhao and Hoeksema 1995a,b). This model has earlier been shown to successfully reproduce the Ulysses open flux observations (Schüssler and Baumann 2006). The CSSS model has three parameters,  $a$  describing the thickness of the current sheet in the lower corona,  $R_{\text{cusp}}$  being the radius of the cusp surface where all field lines are open and  $R_{\text{ss}}$  the radius of the source surface where the magnetic field is fully controlled by the solar wind plasma. Following the previous SFTM versions by Cameron et al. (2010) and Jiang et al. (2011b) we take  $a = 0.2 R_{\odot}$  and  $R_{\text{ss}} = 10 R_{\odot}$ , where  $R_{\odot}$  is the solar radius. For the cusp radius, we choose  $R_{\text{cusp}} = 1.4 R_{\odot}$ , slightly lower than  $1.55 R_{\odot}$  used in the previous studies, as this value returned a better match (lowest  $\chi^2$ -value) to the open magnetic flux from observations, see Sect. 3.6.2. The lower  $R_{\text{cusp}}$  compared to Cameron et al. (2010) could be related to the BMRs having smaller angular separations in the semi-synthetic records compared to the RGO/SOON record or due to the introduction of a weak radial diffusion term with  $\eta_r = 25 \text{ km}^2 \text{ s}^{-1}$ ; see Sect. 3.5.1.

### 3.5.3 Toroidal flux loss calculation

The loss of toroidal flux inside the solar convection zone is linked to the emergence of BMRs. Following Cameron and Schüssler (2020, Eq. 11) we calculated the toroidal flux loss during time interval  $\Delta t$  by adding up the contributions from all individual regions ( $i$ ):

$$\frac{d\Phi_{\text{tor}}}{dt} = \frac{\gamma \sum_i (\Delta\varphi \phi_L (\cos \lambda)^{-1})_i}{2\pi R_{\odot} \Delta t}, \quad (3.16)$$

where  $\Delta\varphi = \Delta\beta \cos(\alpha_m)$  is the absolute value of the longitudinal polarity separation,  $\phi_L$  is the magnetic flux of the loop equal to half of the total flux of the BMR,  $\lambda$  is the emergence latitude and  $\gamma$  is the fraction of magnetic flux emerging in regions following Hale's polarity law (Hale et al. 1919, Hale and Nicholson 1925) minus the fraction disobeying it:  $\gamma(\phi) = (\Phi_{\text{Hale}} - \Phi_{\text{non-Hale}}) / (\Phi_{\text{Hale}} + \Phi_{\text{non-Hale}})$ . In the SFTM, we set the time interval to one day and calculate the longitude separation  $\Delta\varphi$  by subtracting the position of the positive polarity patch from that of the negative one. Since  $\Delta\varphi$  can be positive or negative, this replaces the necessity of the factor  $\gamma$  and we can remove it from the equation. The total toroidal flux loss was calculated by summing up the absolute values for the northern and southern hemispheres:

$$\left| \frac{d\Phi_{\text{tor,hem}}}{dt} \right| = \frac{\left| \sum_i (\Delta\varphi \phi_{\text{BMR}} (\cos \lambda)^{-1})_i \right|}{4\pi R_{\odot}} \quad [\text{Mx day}^{-1}]. \quad (3.17)$$

### 3.5.4 Simulation setup

We ran the SFTM over the period from March 9 1874 to May 5 2019 (Cycles 12-24), with a spatial resolution of  $4^\circ$  ( $l_{\max} = 64$  orders of spherical harmonics) on a  $180 \times 360$  grid with a time step of one day and the model parameters as described in Sect. 3.5.1. We ran the SFTM for each of the 100 realizations of the AMR, LMR and SMR records (see Sect. 3.4.4) and used their average as the result and the standard deviation as an uncertainty estimate.

For the RGO run, we used the same angular separation, tilt angles and the value of the free parameter  $B_{\max} = 374$  G as in Cameron et al. (2010), but use Eq. (3.14) and  $B_{\text{amp}} = B_{\max}$  to calculate the polarity patches. We used  $R_{\text{cusp}} = 1.55 R_\odot$  for the open magnetic flux reconstruction of the RGO/SOON run and  $R_{\text{cusp}} = 1.4 R_\odot$  for AMR, LMR and SMR. Since in the original SFTM version, BMRs were injected not until the polarity patches had diffused to the width of  $4^\circ$ , thus missing the initial phases of the evolution of the smaller ARs, we expect a slightly higher total magnetic flux even for the RGO/SOON in our simulation compared to Cameron et al. (2010).

## 3.6 Results

In this section we present our results from the SFTM and CSSS simulations of the evolution of the total (Sect. 3.6.1), open (Sect. 3.6.2) and polar (Sect. 3.6.3) magnetic field, as well as of the toroidal flux loss (Sect. 3.5.3) and compare them to the available observations. In the next section, we will then analyse the role of the small magnetic regions on the magnetic flux budget using analytical tools.

### 3.6.1 Total magnetic flux

We first look at the total magnetic flux computed from the simulated magnetograms. Figure 3.4 shows the results of the AMR run together with the total magnetic flux from three ground-based observatories (WSO, NSO KP and MWO, black line for the average and dark gray symbols for individual measurements (the latter only in panels a and b to avoid overloading panels c and d) and the KP–MDI–HMI magnetogram composite record from Yeo et al. (2014, green), see Sect. 3.3, for comparison. The KP–MDI–HMI composite has been brought from the HMI to the MWO scale by multiplying with a constant factor of 3.7 (see Sect. 3.3). When comparing simulations to observations, we need to keep the limitations of both the model and the observations in mind. In particular, observations are affected by magnetogram noise and have limited spatial resolution (Krivova and Solanki 2004b). To account for this limited visibility, earlier studies (Solanki et al. 2002, Krivova et al. 2007, Dasi-Espuig et al. 2014, 2016, Krivova et al. 2021) reduced the modelled contribution by ERs by a factor of 0.4 when comparing to observations. At the same time, our model does not explicitly include regions smaller than  $2 \times 10^{20}$  Mx. Thus for comparison purposes, to make the modelled and observed fluxes consistent, we accounted for both these effects. To compensate for the missing flux from SSEs (regions between  $10^{16} - 2 \times 10^{20}$  Mx, see Tab. 3.1) in the SFTM, we computed their contribution using the simpler approach of Solanki et al. (2002), Vieira and Solanki (2010), Krivova et al. (2021) by solving a set of coupled ordinary differential equations. Specifically, we used

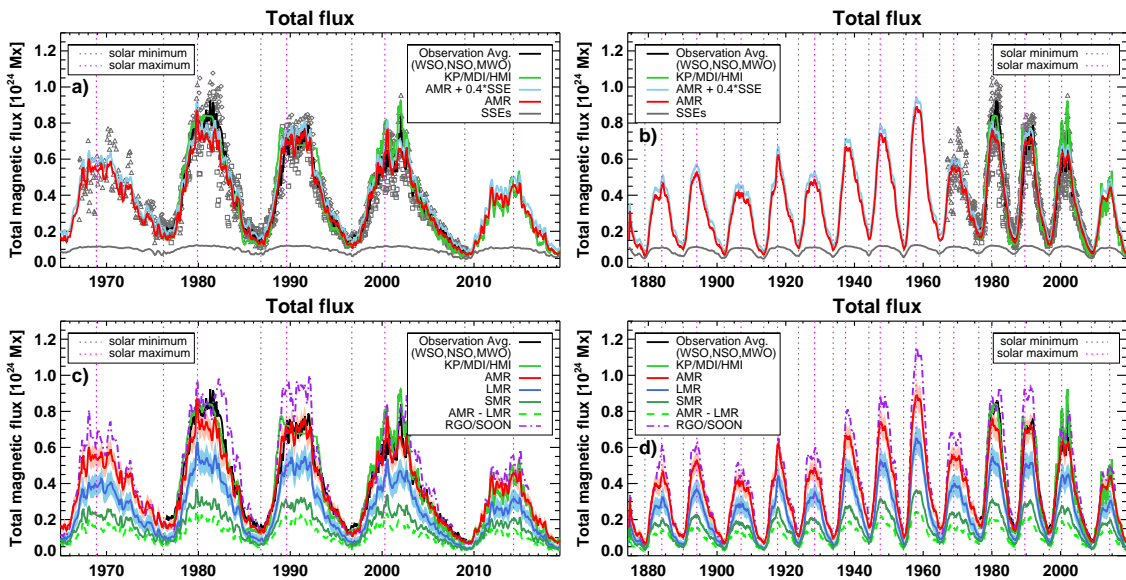


Figure 3.4: Comparison of the simulation results of the total magnetic flux with observations. (a) Evolution of the (3-months smoothed) total magnetic flux from AMRs over Cycles 20–24 and comparison with observations. (b) Same as above but over the entire modelled period from 1874 to 2020. (c) and (d) Comparison of all the simulation runs with error estimates overplotted. Plotted quantities: The light blue line in panels (a) and (b) is the mean of 100 realizations used as input to the SFTM plus 0.4 times the contribution of SSEs estimated from ordinary differential equations following Krivova et al. (2021), see the main text for details. As a comparison we plot the average (black line - all panels) and individual measurements (dark grey symbols - only panels (a) and (b)) of three ground based observatories (WSO, NSO KP, MWO). The total magnetic flux from the KP/MDI/HMI composite by Yeo et al. (2014) is shown in light green in all panels. AMR without SSEs is shown in red in panels (a) and (b) and the mean of the LMR and SMR runs in panels (c) and (d) are shown in blue and green, respectively. The difference between the AMR and LMR run is shown by the light green dashed line. The shaded areas are the standard deviations. The results from the RGO/SOON record are shown by the dash-dotted purple line.

the results from Krivova et al. (2021, grey line) as their BMR emergence model is consistent with ours, except that they only considered the disc-integrated quantities and did not account for the spatial distribution of BMRs. Since such small regions are distributed over the surface rather homogeneously, the effect of changes in their spatial distribution with activity is expected to be negligible. For comparison with observations we then added 0.4 times the SSE magnetic flux to the AMR run. This total magnetic flux is shown by the light blue line in panels a and b, whereas red and dark grey lines give the total magnetic flux from only AMRs or SSEs, respectively. We find that including all regions with lifetimes of more than one day in the AMR record accounts for most of the observed total magnetic flux. The measured flux (black and green) is only slightly higher, by roughly up to 10% at maxima, than the AMR flux (red). By adding  $0.4 \times \text{SSE}$  flux, however, we get an even better agreement with the observations.

In Figures 3.4c and d, we show all simulation runs along with the measurements: AMR (red), LMR (blue), SMR (green) and RGO/SOON (dash-dotted purple line). We notice that the total flux of SMR and LMR does not add up exactly to AMR, see the difference between the AMR and LMR run (dashed light green line). This is the result of SMRs emerging inside the polarity patches of LMRs, which results in partial cancelling of the magnetic flux, see Nèmec et al. (2022). As discussed above, already AMRs alone return a good fit to the data, both during minimum and maximum, which is improved further by adding the SSE flux not included into the model (light blue line in panels a and b). It is important to emphasise that this was obtained without adjusting the magnetic flux amplitude in Eq. (3.14) by comparing to observations, as was done in earlier SFTM versions based entirely on sunspots as input data. Due to the new SFTM setup (see Sect 3.5.1), while keeping the value of the free parameter unchanged, the RGO/SOON run is about 5% higher during solar maximum than in the previous model by Cameron et al. (2010), but almost identical during solar minimum.

Comparing the contributions by SMRs and LMRs, we see that during activity maxima about two thirds of the total magnetic flux come from LMRs, while most of the remaining flux comes from SMRs (with only small contribution of yet smaller regions, SSEs). At activity minima, both LMR and SMR contribute roughly equally. We also see that the total flux from SMRs differs very weakly among the various realizations and thus most of the “noise” comes from large ARs.

### 3.6.2 Open magnetic flux

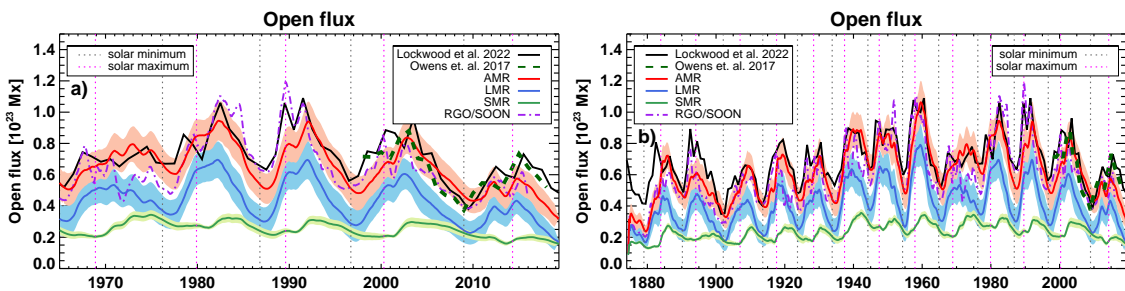


Figure 3.5: Comparison of the simulation results of the open magnetic flux with observations. The red, blue and green curves are the mean results of 100 realizations used as input to the SFTM for AMR, LMR and SMR, respectively. The shaded areas are the standard deviations. The results from the RGO/SOON record are shown by the dash-dotted purple line. (a) Reconstruction of the (1-year smoothed) open magnetic flux from the CSSS model over Cycles 20–24. The black line is the reconstruction from the geomagnetic  $aa$ -index by Lockwood et al. (2022) and the dark green dashed line shows the in-situ measurements by Owens et al. (2017). (b) Same as above but over the entire period from 1874–2020.

The modelled open magnetic flux (green, blue, red, and dot-dashed purple lines for SMRs, LMRs, AMRs and RGO, respectively) reconstructed with the CSSS extrapolation as described in Sect. 3.5.2 is compared to observations in Fig. 3.5. We compare the model

output to the open flux reconstruction by [Lockwood et al. \(2022\)](#) from the geomagnetic *aa*-index (black) and the in-situ measurements since 1998 by [Owens et al. \(2017\)](#) (dashed dark green). The computed AMR open flux agrees well with both data sets, although sometimes (e.g. in 1996) minima in the simulations are slightly (by roughly a year or two) delayed. In [Cameron et al. \(2010\)](#) it was shown that the timing of the minima in the open flux is delayed for higher  $\eta_r$ . There it was found that  $\eta_r = 0$  can reproduce the timing of the minima. In this paper a non-zero value of  $\eta_r$  is needed in the simulations to prevent a multicycle drift of the polar fields ([Schrijver et al. 2002](#)). This drift is possibly a consequence of the SFT model not being a full dynamo model and as such lacking any feedback mechanisms which might prevent such a drift.

Over the last two cycles, the AMR run is consistent with the measurements by [Owens et al. \(2017\)](#), lying within the uncertainty range for almost the entire interval. The computed open flux at maximum of cycle 24 is slightly lower than the measured flux. We recall, however, that our model does not include the contribution of the smallest regions and in contrast to the total magnetic flux, it is not straightforward to add it from another model, e.g. from [Krivova et al. \(2021\)](#), as we did for the total flux. Over the entire modelled period, the amplitude of the solar cycle variation in the open flux is in good agreement with the reconstruction by [Lockwood et al. \(2022\)](#). The computed open flux is slightly lower than the empirical reconstruction at the maxima of cycle 22 and 24. It is also slightly higher than the reconstruction from the *aa* index around the maximum of cycle 20, although within the model uncertainties, and cycle 20 might be anomalous in the *aa*-based reconstruction (see [Lockwood et al. 2022](#)). Furthermore, the computed open flux is noticeably lower than the reconstruction by [Lockwood et al. \(2022\)](#) during the first two cycles covered by simulations, for both the AMR and the RGO/SOON runs. This is because of our simple initial magnetic field configuration, taken from [van Ballegoijen et al. \(1998, see their Eq. 16\)](#), and hence the results during these first two cycles should be taken with caution.

The RGO/SOON run is also mostly consistent with [Lockwood et al. \(2022\)](#) and [Owens et al. \(2017\)](#) although for some mostly weak cycles the open flux from the RGO run is considerably weaker than in the empirical reconstruction and the AMR run, for example during cycles 15, 17 and 20. The reason could be that during weak cycles, the relative role of the smaller regions is higher than during high activity cycles. Looking at the individual contributions by LMR and SMR we find that the LMR run follows a similar shape to the AMR run, although lower in amplitude. Interestingly, the timings of the peaks and troughs are more consistent with [Lockwood et al. \(2022\)](#). The timings of the SMRs are noticeably delayed, with the troughs in the open flux being close to solar maximum and the peaks in the declining phase of the cycle. The reason for this is that the open flux is dominated by a contribution of the axial and equatorial dipole moments. In the case of the LMRs, this balance is dominated by the equatorial dipole moment, which leads to the open flux peaking in phase with the solar cycle. In the LMR case, the equatorial dipole moment is made up of comparable contributions from the LMRs emerging at random longitudes and those emerging in nests (see Section 3.2.3). In the case of the SMRs, there are so many small emergences that the contribution from the random longitudes average out, and the only substantial contribution to the equatorial dipole moment is that due to nesting. Consequently the axial dipole moment plays a larger role and the minima of the open flux are moved closer to the polar field reversals. The SMR amplitude is comparable

in amplitude to LMR during solar minimum, but only about one third of LMR during solar maximum. Similar to the total flux we find that the majority of the noise comes from large ARs, with only a small contribution by SMRs.

### 3.6.3 Polar fields

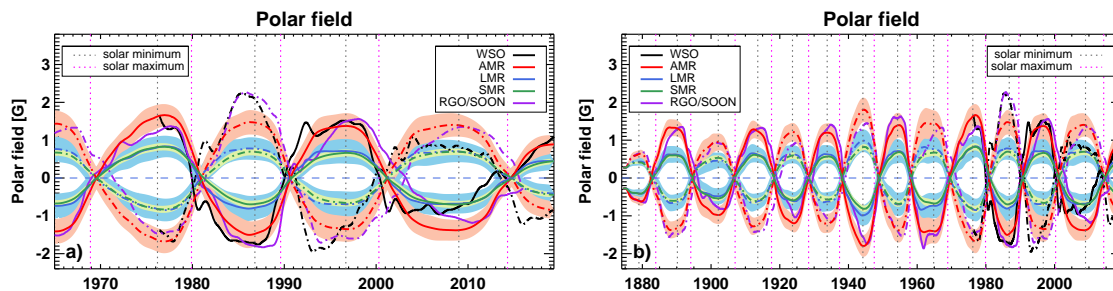


Figure 3.6: Comparison of the simulation results of the line-of-sight polar magnetic field with observations. The red, blue and green curves are the mean results of the SFTM for 100 realizations used as input for AMR, LMR and SMR, respectively. The shaded areas are the standard deviations. The results from the RGO/SOON record are shown by the dashed-dotted purple line. (a) The line-of-sight polar field above  $55^\circ$  latitude and the measurements from WSO (black) over Cycles 20–24 multiplied by a factor 1.5. The northern polar fields are given by the solid lines, and southern polar fields are dot-dashed. (b) Same as above but over the entire modelled period from 1874–2020.

In Figure 3.6, we compare the simulated line-of-sight polar field above  $55^\circ$  latitude to the line-of-sight observations by WSO (black; Scherrer et al. 1977, Hoeksema et al. 1983). To account for magnetograph saturation, the WSO data is multiplied by a constant factor of 1.5 (see also Svalgaard et al. 1978, Jiang et al. 2013). Again, we expect the AMR run to be slightly lower than observations, because we are missing the contribution by the smallest regions (SSEs, see Sect. 3.6.1). In contrast to the total magnetic flux, it is not straightforward to add this contribution separately. However, the contribution by very small ERs is expected to be rather small, due to the randomness in their tilt angles.

We find a good agreement between the AMR run (red) and WSO except for the period between maxima of Cycle 23 and 24 (2000–2014), where we overestimate the amplitude by about 30% and in the declining phases of Cycle 21 and 22 (1985 and 1994) where we underestimate the polar field in the southern hemisphere by 30% and 25%, respectively. A too high flux during Cycles 23/24 was also found for the RGO/SOON run, as well as in the study by Jiang et al. (2013) (using the RGO/SOON record as SFTM input) who found that the polar field amplitude in the declining phase of Cycle 23 (after year 2000) was too high compared to WSO. This was caused by several large ARs close to the equator disobeying Joy’s law (Jiang et al. 2015). When using the observed tilt angles instead of the statistical ones, they found a good agreement with the WSO data.

Comparing the LMR and SMR runs, we find that their amplitudes are very similar throughout the entire interval. Therefore, the contribution by small regions in the AMR run is much higher for the polar fields than for the total and open magnetic flux. The

higher importance of small BMRs for the polar fields could explain why the RGO/SOON run from our simulation has a similar amplitude to the AMR run, occasionally being even smaller than AMR, despite the total magnetic flux of RGO/SOON being consistently higher than AMR (see Fig. 3.4). The AMR, LMR and SMR runs all show regular polar reversals. However the reversals in cycles 21, 23 and 24 are delayed by about 1 year compared to the WSO measurements. The timing of the polar field (here poleward from  $\lambda| = 55^\circ$ ) reversals depends on the strength of the polar fields, the amount of flux carried past  $\lambda| = 55^\circ$ , and  $\eta_r$ . Importantly, flux of both polarities is carried, so that the polar field can change sign several times before it finally reverses. The delay in cycles 21, 23 and 24 are within one standard deviation of the expectation value. We therefore suggest that the delay in the model for these cycles might be related to the scatter in the tilt angles at high-latitudes which affects the timing of the reversal but not the long-term strength of the polar fields. As with the total and open flux, we find that the polar field noise is dominated by LMRs.

### 3.6.4 Toroidal flux loss

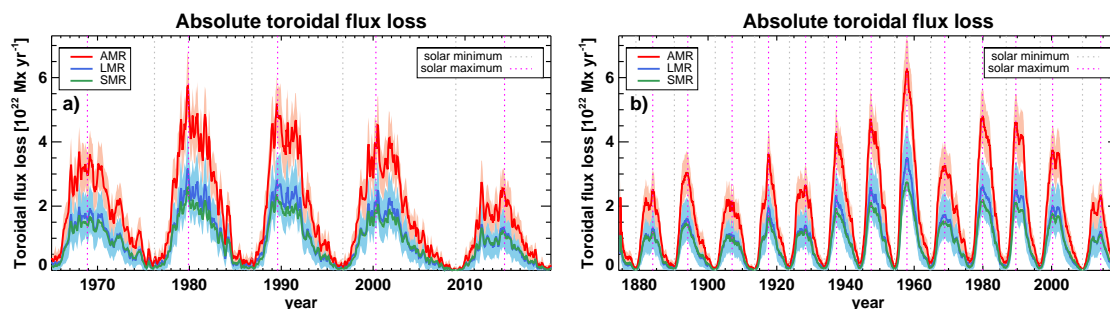


Figure 3.7: Comparison of the simulated toroidal flux loss with observations. The red, blue and green curves are the mean results of 100 realizations used as input to the SFTM for AMR, LMR and SMR, respectively. The shaded areas are the standard deviations. (a) 3-month smoothed sum of the absolute toroidal flux loss of both hemispheres over Cycles 20–24. (b) 1-year smoothed sum of the absolute toroidal flux loss of both hemispheres over the entire simulated period from 1874–2020.

The toroidal flux loss calculated from Eq. (3.17) for AMR (red) and LMR (blue) is shown in Fig. 3.7. Because the toroidal flux loss linearly depends on the magnetic flux emerging in BMRs (see Eq. 3.17), its temporal profile is quite similar to that of the total magnetic flux. During solar maxima of Cycles 21–24, we find between  $2 - 5 \times 10^{22} \text{ Mx year}^{-1}$  for the toroidal flux loss for AMRs. This is in good agreement with the recent studies that found a toroidal flux loss of  $\approx 4 \times 10^{22} \text{ Mx year}^{-1}$  in the same time period from WSO magnetograms (Jeffers et al. 2022) and the estimate by Cameron and Schüssler (2020). We find that contributions to the toroidal flux loss of both the LMR and SMR runs are similar during both activity minima and maxima, each contributing  $\approx 50\%$  to the AMR run. Thus, small regions have noticeably higher contribution to the toroidal flux loss than to the total magnetic flux. The toroidal flux loss noise is dominated by LMRs.

## 3.7 Understanding the role of small BMRs

In Sect. 3.6, we showed that the simulated total and open magnetic flux, the polar fields and the toroidal flux loss are in good agreement with observations and/or other reconstructions. To better understand the role of small ARs on basic solar quantities and simulation results, we also analyse analytically the governing equations of these solar quantities and compare the analytical results with those obtained from the simulations. This acts both as a test of our simulations and as a guideline for the importance of small-scale regions for future studies.

The open magnetic flux hereby depends on a variety of factors, such as the degree of nesting, the fragmentation rate of ARs and the equatorial dipole moment. This would require a far more detailed analysis than for the total flux, the polar fields and the toroidal flux loss that would go beyond the scope of this work, so we will limit our interpretation of the open flux to the simulation results; see Sect. 3.6.2.

### 3.7.1 Total flux

The total magnetic flux is determined by the amount and size of magnetic flux elements present on the solar surface. Using high-resolution Hinode magnetograms, [Parnell et al. \(2009\)](#) found that the number of magnetic flux elements on the solar surface per area per magnetic flux follows a power-law size distribution:

$$\frac{dN_p(\phi)}{d\phi} = N_f \phi^q [\text{Mx}^{-1} \text{cm}^{-2}], \quad (3.18)$$

where  $N_f = 3 \times 10^{-4} \text{cm}^{-2}$ ,  $\phi$  is the magnetic flux of the flux element in Mx and  $q = -1.85$  (denoted as  $\alpha$  in [Parnell et al. 2009](#)), cf. Eq. (3.1) for the emergence rate. The total magnetic flux per area of all regions between magnetic flux limits  $\phi_1$  and  $\phi_2$  is calculated by integrating the product of the magnetic flux  $\phi$  and Eq. (3.18):

$$\Phi_{\text{total}} = \int_{\phi_1}^{\phi_2} N_f \phi^q \phi \, d\phi = \frac{N_f}{(q+2)} \left[ \phi^{q+2} \right]_{\phi_1}^{\phi_2} [\text{G}]. \quad (3.19)$$

The resulting exponent  $(q+2) = 0.15$  is larger than 0, which means that the total flux should be dominated by large BMRs. This is consistent with the simulation (see Fig. 3.4), showing that the LMR run contributes about 70% to the total magnetic flux at activity maxima, while SMRs only account for about 30%. As has been shown in Sect. 3.6.1, yet smaller BMRs not accounted by our model have an almost negligible effect on the total flux. Note though that at activity minima the contribution of SMRs is comparable to that of spot-containing LMRs. The exponent  $q$  in Eq. (3.18) was derived by [Parnell et al. \(2009\)](#) from the data without accounting for the activity level. If it varies with activity similarly to the exponent  $m$  in Eq. 3.1, the exponent  $(q+2)$  is getting closer to 0 at minima, in agreement with what we see in Fig. 3.4.

Assuming that the noise is Gaussian and that the individual emergences are independent of each other, the uncertainty (or noise) of the total flux is proportional to the square root of the number of magnetic flux elements:

$$\Phi_{\text{total}}^{\text{Noise}} \sim \int_{\phi_1}^{\phi_2} \phi^{q/2} \phi \, d\phi \sim \left[ \phi^{q/2+2} \right]_{\phi_1}^{\phi_2} [\text{G}]. \quad (3.20)$$

The power-law exponent  $q/2 + 2 = 1.075$  is significantly higher than zero, hence the noise must be dominated by large regions. This agrees with our simulations, as there is almost no observable variance between the SMR realizations and the noise of LMR and AMR runs is almost identical.

### 3.7.2 Polar fields

As described by Eq. (3.14), BMRs in the SFTM emerge as bipolar polarity patches with the same amount of positive and negative magnetic flux. As the BMR evolves, the polarities eventually cancel each other out by diffusion or after they are transported to the poles by the meridional flow. However, if a BMR is close to the equator, part of the magnetic flux can cross it and move to the other hemisphere before being cancelled out. This results in a change in the polar field strength. Petrovay et al. (2020, Eq. 24) have derived this "transequatorial flux fraction"  $f_{\text{tr}}$  for small latitude separations  $\Delta\lambda$  between the polarity patches as:

$$f_{\text{tr}} \simeq \frac{\Delta\lambda}{\sqrt{2\pi} \lambda_R} \exp\left(\frac{-\lambda^2}{2\lambda_R^2}\right), \quad (3.21)$$

where  $\lambda$  is the emergence latitude and  $\lambda_R$  is the so-called dynamo effectivity range that depends on the SFTM model parameters. The latitude separation  $\Delta\lambda$  depends on the angular separation  $\Delta\beta$  and hence on the square root of the magnetic flux of the BMR (see Eq. 3.15):

$$\Delta\lambda = \Delta\beta \sin(\alpha_m) \sim \sqrt{\phi} \sin(\alpha_m). \quad (3.22)$$

The tilt angle is proportional to the square root of the emergence latitude ( $\alpha_m \sim \sqrt{\lambda}$ ) and the mean emergence latitude depends on the phase (time) in the cycle and the cycle strength, but both are independent of the BMR flux  $\phi$ . The polar field strength now depends on the number of emerging regions (Eq. 3.1) over the solar cycle times their magnetic flux times the fraction of that flux that crosses the equator (Eq. 3.21):

$$\begin{aligned} \Phi_{\text{polar}} &= \int_{t_1}^{t_2} \int_{\phi_1}^{\phi_2} \frac{dN_e(\phi)}{d\phi} \phi f_{\text{tr}} d\phi dt \\ &\sim \int_{t_1}^{t_2} f_{\text{lat}}(t) \left[ \phi^{m+\frac{5}{2}} \right]_{\phi_1}^{\phi_2} dt \\ &\sim \langle f_{\text{lat}}(t) \rangle \left[ \phi^{m+\frac{5}{2}} \right]_{\phi_1}^{\phi_2}, \end{aligned} \quad (3.23)$$

where  $f_{\text{lat}} = \sin(\alpha_m) \exp\left(-\lambda^2/(2\lambda_R^2)\right)$  is independent of  $\phi$  and  $m = -2.69$  is the power-law exponent from Thornton and Parnell (2011). The average  $\langle f_{\text{lat}} \rangle$  is calculated at an emergence latitude of  $\lambda = 15^\circ$  and the mean tilt angle of  $\alpha_m = 5^\circ$ . The exponent  $m_e + 5/2 = -0.19$  is slightly lower than zero, which means that small BMRs should contribute a similar or slightly larger amount of flux to the poles as the large BMRs. From Fig. 3.6, we find that the polar fields from small regions in the SMR record are indeed roughly as strong as in the LMR run, both during activity minima and maxima. Therefore SMRs have a much higher contribution to the polar fields than to the total magnetic flux.

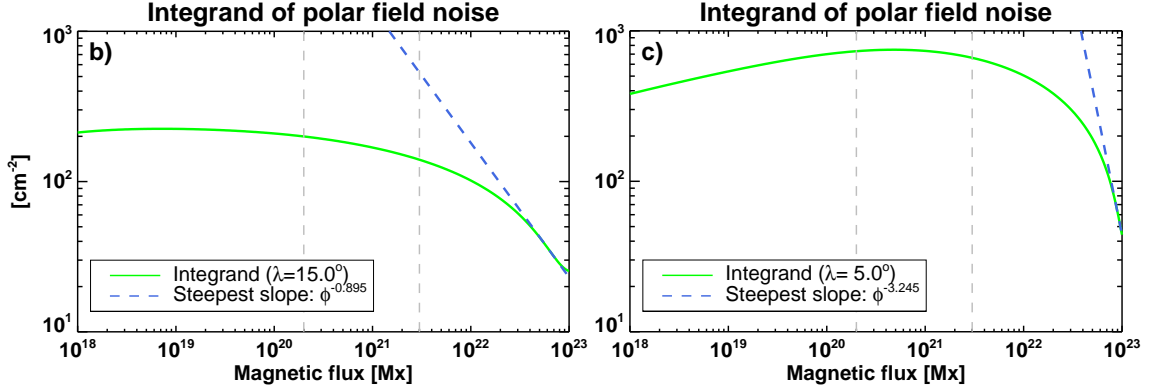


Figure 3.8: Estimating the polar field noise. Integrand of Eq. (3.28) (green solid) and the tangent power law at the steepest point (blue dashed). (a) Emergence latitude at 15°. (b) Emergence latitude at 5°. The vertical gray lines mark the lower flux limits of AMR and LMR.

Now we consider the uncertainty of the polar fields, again by taking the square root of the number of emerging BMRs:

$$\Phi_{\text{polar}}^{\text{noise}} \sim \int_{\phi_1}^{\phi_2} \text{SD} \left[ \sin(\alpha_m) \exp\left(\frac{-\lambda^2}{2\lambda_R^2}\right) \right] \phi^{(m_e+3)/2} d\phi, \quad (3.24)$$

where  $\text{SD}[\dots]$  denotes the standard deviation. As described in Sect. 3.4, the standard deviations of the tilt angle and the emergence latitude are dependent on the regions size and they need to be considered in our calculation. The standard deviation of the sinusoidal function  $A = \sin(\alpha_m)$  is calculated as:

$$\sigma_A = \sqrt{(1 - \exp(-\sigma_{\text{tilt}}^2)) (1 + \exp(-\sigma_{\text{tilt}}^2) \cos(2\alpha_m))} / 2 \quad [\text{rad}], \quad (3.25)$$

where  $\sigma_{\text{tilt}}$  is given by Eq. (3.10). The standard deviation of the exponential function  $B = \exp\left(\frac{-\lambda^2}{2\lambda_R^2}\right)$  can be estimated as:

$$\sigma_B \approx \frac{1}{2} \left[ \exp\left(-\left(\frac{\lambda - \sigma_{\text{lat}}}{\sqrt{2}\lambda_R}\right)^2\right) - \exp\left(-\left(\frac{\lambda + \sigma_{\text{lat}}}{\sqrt{2}\lambda_R}\right)^2\right) \right] \quad [\text{rad}], \quad (3.26)$$

where  $\sigma_{\text{lat}}$  is given by Eq. (3.8) and  $\lambda_R = 7.5^\circ$  for our SFTM setup. The combined standard deviation  $\sigma_{AB}$  is defined as:

$$\sigma_{AB} = \sqrt{(A \cdot \sigma_B)^2 + (\sigma_A \cdot B)^2 + (\sigma_A \cdot \sigma_B)^2}. \quad (3.27)$$

Plugging into Eq. (3.24) we find:

$$\Phi_{\text{polar}}^{\text{noise}}(\phi) \sim \int_{\phi_1}^{\phi_2} \sigma_{AB} \phi^{(m_e+3)/2} [\text{cm}^{-2}] d\phi. \quad (3.28)$$

Equation (3.28) cannot be solved analytically, so instead we discuss the result by plotting the integrand in Fig. 3.8a. We find a concave function with the steepest (negative) slope

at  $6 \times 10^{22}$  Mx. Integrating the tangent power law, we find the exponent of  $\sim 0.1$ . As this is higher than zero, and becomes even larger for smaller regions, we conclude that the uncertainty of the polar fields is dominated by large ARs. We note however, that if we choose an emergence latitude even closer to the equator ( $\lambda \leq 15^\circ$ ), the tangent power law for the largest ARs is so steep that the exponent of the tangent power law becomes slightly negative, see e.g. the example for  $\lambda = 5^\circ$  in Fig. 3.8b. While this does not change the qualitative result that small BMRs have only a small contribution, it means that the contribution of the largest ARs ( $\geq 10^{22}$  Mx) this close to the equator is lower than that by small and medium LMRs ( $\leq 10^{22}$  Mx). This can be explained by the proximity to the equator, such that for very large spots parts of both polarity patches can cross, which leads to a stronger cancellation of the magnetic flux that is transported to the poles. Comparing the analytical results to the simulation (Fig. 3.6), we find that the LMR runs show a much greater variation between individual runs than SMR, which can in some cases lead to delayed or irregular polar field reversals. So while the contribution of small BMRs has a large impact on the polar field amplitude, they actually seem to stabilize the runs and lead to less variation between different realizations and more stable polar field reversals. Therefore the uncertainty of the polar fields in the simulation is dominated by LMRs.

### 3.7.3 Toroidal flux loss

The toroidal flux loss is calculated from Eq (3.16), as described in Sect. 3.5.3. Plugging in the flux emergence rate from Eq. (3.1) we find:

$$\begin{aligned} \Phi_{\text{tor}} &= \int_{t_1}^{t_2} \int_{\phi_1}^{\phi_2} \frac{dN_e(\phi)}{d\phi} \phi \frac{\gamma(\phi) \Delta\beta \cos(\alpha_m)}{2\pi R_\odot \cos(\lambda)} d\phi dt \\ &\sim \int_{t_1}^{t_2} \frac{\cos(\alpha_m)}{\cos(\lambda)} \int_{\phi_1}^{\phi_2} \gamma(\phi) \phi^{m_e + \frac{3}{2}} [\text{cm}^{-2} \text{ s}^{-1}] d\phi dt. \end{aligned} \quad (3.29)$$

This integral over  $\phi$  cannot be solved analytically.  $\gamma(\phi)$  varies between 1 and 0 and depends on the probability of a region emerging with proper Hale-orientation  $P_{\text{Hale}}$ , which depends on the tilt angle scatter  $\sigma_{\text{tilt}}$ ; see Eq. (3.10). Using the definition of the normal distribution we calculate:

$$\begin{aligned} P_{\text{Hale}} &= \int_{-90^\circ - \alpha_m}^{90^\circ - \alpha_m} \frac{\exp\left(-\frac{x}{2\sigma_{\text{tilt}}}\right)^2}{\sqrt{2\pi} \sigma_{\text{tilt}}} dx \\ &= \frac{1}{2} \left[ \left( \frac{\alpha_m + 90^\circ}{\sqrt{2} \sigma_{\text{tilt}}} \right) - \left( \frac{\alpha_m - 90^\circ}{\sqrt{2} \sigma_{\text{tilt}}} \right) \right]. \end{aligned} \quad (3.30)$$

The probability of the region being anti-Hale oriented is  $1 - P_{\text{Hale}}$ . Hence we can rewrite  $\gamma(\sigma_{\text{tilt}})$  by calculating:

$$\begin{aligned} \gamma(\phi) &= P_{\text{Hale}} - (1 - P_{\text{Hale}}) = 2P_{\text{Hale}} - 1 \\ &= \left[ \left( \frac{\alpha_m + 90^\circ}{\sqrt{2} \sigma_{\text{tilt}}} \right) - \left( \frac{\alpha_m - 90^\circ}{\sqrt{2} \sigma_{\text{tilt}}} \right) \right] - 1. \end{aligned} \quad (3.31)$$

For the calculation we assume a typical mean tilt angle of  $\alpha_m = 5^\circ$  at  $15^\circ$  latitude. The exact choice is not important as it has no significant effect on the results. In order to

evaluate the integral we plot the integrand from the integration over  $\phi$  in Fig. 3.9a. We see that the integrand is again a concave function, so we evaluate the result by considering the tangent power laws at the steepest point at the upper flux limit of  $1 \times 10^{23}$  Mx and at the lower flux limit of AMRs. Integration of the tangent power-law exponent at the upper limit gives the exponent  $-0.19$ , which is smaller than zero. We obtain a similar result for the smallest regions in our model at the lower AMR limit with the exponent  $-0.04$ . Therefore, we expect small regions to play a large role for the toroidal flux loss, similar to or even larger than that of large BMRs. Indeed we find in the simulation (Fig. 3.7) that LMR and SMR contribute about equally to the total AMR toroidal flux loss. Hence, we conclude that the toroidal flux loss is dominated by small ARs and large ERs.

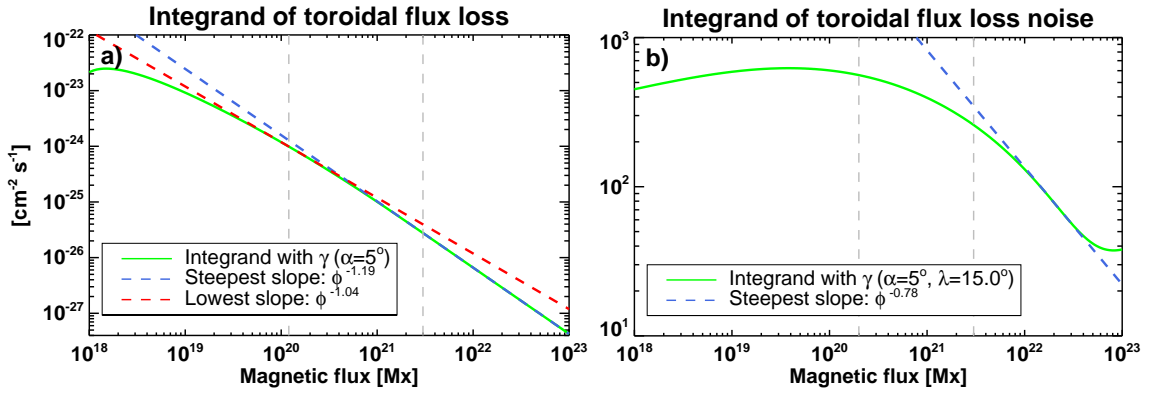


Figure 3.9: Estimating the toroidal flux loss and the toroidal flux loss noise. (a) Integrand of Eq. (3.29) (green solid) and the tangent power law at the steepest point (blue dashed). (b) Same but for the integrand of Eq. (3.32). The vertical gray lines marks the lower flux limits of AMR and LMR.

The uncertainty of the toroidal flux loss depends on the square root of the number of emerging BMRs:

$$\begin{aligned} \Phi_{\text{tor}}^{\text{noise}} &\sim \int_{\phi_1}^{\phi_2} \text{SD} \left[ \frac{\cos(\alpha_m)}{\cos(\lambda)} \right] \phi^{(m_e+3)/2} d\phi \\ &= \int_{\phi_1}^{\phi_2} \sigma_{\text{CD}} \phi^{(m_e+3)/2} [\text{cm}^{-2} \text{s}^{-1}] d\phi, \end{aligned} \quad (3.32)$$

where  $\sigma_{\text{CD}}$  is the combination of the standard deviation of the cosine function  $C = \cos(\alpha_m)$  and the standard deviation of the inverse cosine function  $D = \cos^{-1}(\lambda)$ . The standard deviation of  $C$  is calculated as:

$$\sigma_C = \sqrt{(1 - \exp(-\sigma_{\text{tilt}}^2)) (1 - \exp(-\sigma_{\text{tilt}}^2) \cos(2\alpha_m)) / 2}, \quad (3.33)$$

where we use  $\alpha_m = 5^\circ$  and  $\sigma_{\text{tilt}}$  is given by Eq. (3.10). The standard deviation of  $D$  is calculated as:

$$\sigma_D \approx \frac{1}{2} \left| \left( \cos(\lambda) + \text{SD}[\cos(\lambda)] \right)^{-1} - \left( \cos(\lambda) - \text{SD}[\cos(\lambda)] \right)^{-1} \right|, \quad (3.34)$$

where  $\sigma_{\text{lat}}$  is given by Eq. (3.8). The combined standard deviation is:

$$\sigma_{\text{CD}} = \sqrt{(C \cdot \sigma_D)^2 + (\sigma_C \cdot D)^2 + (\sigma_C \cdot \sigma_D)^2}. \quad (3.35)$$

The integrand at emergence latitude  $15^\circ$  is plotted in Fig. 3.9b. We find a similar case to the polar field noise, where we find a concave function, and the exponent of the integral over  $\phi$  of the steepest tangent power law at  $2 \times 10^{22}$  Mx is  $0.22 > 0$ . At emergence latitudes  $\leq 10^\circ$ , the tangent power-law exponent becomes lower than zero, which diminishes the contribution by very large ARs ( $\geq 10^{22}$  Mx). We conclude that the toroidal flux loss noise is dominated by LMRs at medium to high emergence latitudes, and by small and medium LMRs ( $\leq 10^{22}$  Mx) at low latitudes. Comparing the result to the simulations in (Fig. 3.7), we find that majority of the noise indeed comes from the LMRs that are included in both simulation runs.

### 3.8 Summary and conclusion

We analysed the effect of small magnetic regions on basic solar quantities, including the total and open magnetic flux, the polar fields and the toroidal flux loss. For this purpose, we simulated the Sun's large-scale magnetic field since 1874 using an SFTM (Baumann et al. 2004, Cameron et al. 2010, Jiang et al. 2011b) to describe the evolution of BMRs on the solar surface upon their emergence, and validated the results through their comparison with observations and analytical approximations. As input we used semi-synthetic BMR emergence records constructed from the international sunspot number (version2, ISN2.0). Compared to previous versions of the model (Cameron et al. 2010, Jiang et al. 2011b), we included not only large, spot-containing ARs, but also smaller BMRs with lifetimes of at least one day.

To include smaller BMRs (i.e. those not represented by the historic sunspot observations) into the model, the emergence rate of all BMRs was taken to follow a single power-law size distribution, as derived from observations by Thornton and Parnell (2011), with the exponent varying with the sunspot number, following Krivova et al. (2021). To derive the mean and the scatter of the BMR emergence latitudes, as well as the mean and the scatter of the BMR tilt angles, we started with the empirical relationships from Jiang et al. (2011a, hereinafter referred to as J11), Jiang (2020, called J20 from now on) as well as Solanki et al. (2008). We have, however, partly revised and extended them to account for the overlap between solar cycles and the dependence of the latitude and tilt scatter on the size of BMRs, based on observations by Harvey (1993, H93 from now on) and Schunker et al. (2020).

To incorporate the cycle overlap into the model, we used the observational results by H93 and the RGO/SOON sunspot group data record to roughly estimate the emergence rate of BMRs of various sizes during different cycle phases. These constraints were then used to split the emerging BMRs between every pair of overlapping cycles. Thereby, we assumed that a new cycle starts (with negligibly low emergence rate) at high latitudes soon after the polar field reversal around the maximum of the preceding cycle (Wilson et al. 1988, Harvey 1993, Tlatov et al. 2010, McIntosh et al. 2014) and it ends two years after the solar minimum following H93.

Using these emergence patterns, we synthesised a set of 100 independent realizations to estimate how the randomness of the statistical relationships affects the simulation results. We considered three types of input records, one with all modelled regions (AMR) with lifetimes  $\geq 1$  day and magnetic flux  $\geq 2 \times 10^{20}$  Mx, another one including only the larger, spot-containing regions (LMR) with flux  $\geq 3 \times 10^{21}$  Mx and a final one with only the small non-spot regions (SMR) having fluxes below  $3 \times 10^{21}$  Mx. The flux limit for LMRs was selected such as to make the LMR record consistent with the RGO/SOON sunspot group record used as input to the previous versions of the model, thus allowing a direct comparison.

To model the evolution of BMRs more realistically than in previous versions of the SFTM, we included all regions (regardless of their size) from the point of their maximum development, so that we always model the entire decay process in the SFTM. The angular separation between the emerging BMR polarity patches and the initial magnetic flux density were chosen such that the decay rate and the initial magnetic flux content of the BMRs are consistent with observations (Parnell et al. 2009, Thornton and Parnell 2011). Regions that are too narrow upon emergence to be spatially resolved in the SFTM were treated in separate, secondary magnetograms where they were only subjected to the effect of turbulent diffusion. The secondary magnetograms were then included in the total magnetic flux calculation at each time step, while the individual regions in the secondary magnetograms were added to the main magnetograms once they exceeded the resolution limit of the latter.

We compared the simulation results to various observations and reconstructions. Furthermore, to better understand the role of small BMRs on the evolution of global magnetic quantities, we analysed the governing equations of the total magnetic flux, the polar fields and the toroidal flux loss. We summarize our results as follows:

1. The simulated total magnetic flux from the AMR run (that is all modelled magnetic regions in the range  $2 \times 10^{20} - 10^{23}$  Mx) is in good agreement with ground-based observations (WSO, NSO, MWO) as well as the composite of measurements by NSO/KP, SoHO/MDI and SDO/HMI. The LMRs (large, spot-containing active regions with fluxes in the range  $3 \times 10^{21} - 10^{23}$  Mx) alone account for about two thirds of the magnetic flux during activity maxima, while during minima LMRs and SMRs (small BMRs in the range  $2 \times 10^{20} - 3 \times 10^{21}$  Mx) contribute roughly equally. Because we only included regions with lifetimes longer than one day into the simulations, the smallest BMRs with fluxes below  $2 \times 10^{20}$  Mx were not covered. We estimated their contribution to the measured magnetic flux using a simpler model by Krivova et al. (2021). Their inclusion slightly improved the agreement with the measured flux, but most of the total flux in the records we considered is well accounted by AMRs alone (that is all regions with fluxes above  $2 \times 10^{20}$  Mx).
2. The simulated open magnetic flux is in good agreement with satellite measurements (Owens et al. 2017) and the empirical reconstruction from the geomagnetic *aa* index (Lockwood et al. 2022). The simulated open flux is sometimes slightly delayed (by up to a year or two) compared to the *aa*-based reconstruction. SMRs contribute about one third to the overall open magnetic flux at maxima and  $\approx 40 - 50\%$  at minima.

3. Both the AMR and LMR simulations return regular polar field reversals near solar maxima, in good agreement with the line-of-sight polar field measurements from WSO. The AMR polar field amplitude agrees reasonably with the WSO data, although it slightly underestimates the polar field amplitude in the southern hemisphere in the declining phases of Cycles 21 and 22 while overestimating the polar field during cycle 23. The LMR and SMR runs each contributed equally to the total polar fields during both solar minimum and maximum. The addition of SMRs leads to more consistent polar field reversals of the individual runs.
4. We find a total toroidal flux loss from AMRs of  $2 - 5 \times 10^{22} \text{ Mx yr}^{-1}$  during the activity maxima of cycles 21–24. This is in good agreement with [Jeffers et al. \(2022\)](#) who found  $\sim 4 \times 10^{22} \text{ Mx yr}^{-1}$  from WSO magnetograms in the same period of time. LMRs and SMRs contributed roughly equally to the AMR toroidal flux loss, both during minima and maxima.
5. For all solar parameters (total flux, open flux, polar fields, toroidal flux loss) the noise was dominated by LMRs. This is because due to the small number and large size of LMRs, individual regions can have a significant impact on the magnetic field, while the high number of SMRs smears out the contribution of each individual region.

To summarise, we found that SMRs are especially important for the polar field strength and the toroidal flux loss, as their contribution is about equal to that of LMRs, both during activity minima and maxima. The inclusion of yet smaller ERs ( $< 2 \times 10^{20} \text{ Mx}$ ) to the model would even further increase the contribution of small regions to the polar fields and toroidal flux. This makes small BMRs interesting for dynamo studies, as the polar fields and their noise play a crucial role in the generation of the toroidal field of the next solar cycle and as such are crucial for understanding the solar dynamo ([Cameron and Schüssler 2015](#)). The same is true for the toroidal flux loss. The total and open magnetic flux at activity maxima are more strongly influenced by LMRs. At activity minima, small BMRs play a significant role in determining all solar quantities considered in this study: the total magnetic flux, open flux, polar fields and toroidal flux loss. The noise for all these quantities is, however, dominated by large ARs. Since small BMRs are numerous and are widely spread over the solar surface, the contribution of individual small regions smears out.

We have included small ARs (those that are not covered by the historic sunspot records) and large ERs into the SFTM and studied their influence on the solar magnetic field. Inclusion of yet smaller ERs ( $< 2 \times 10^{20} \text{ Mx}$ ) into the model poses additional challenges. Firstly, the temporal and spatial resolution need to be further increased to accurately model the early evolution of small BMRs. Secondly, a much higher number of total regions would lead to a significantly higher part of the initial magnetic flux in the magnetograms being cancelled by overlapping polarity patches of neighboring regions. The imposed shape of the BMRs however cannot be easily changed, as it is tied to the decay rate and a narrower shape would decrease the region lifetime. Therefore we might require a separate treatment for the smallest of ERs. Note however, that the smallest ERs have a much wider scatter in their tilt angles so that only a small fraction obeys Hale’s polarity law. It is believed that a significant amount of this flux comes from a small-scale dynamo

operating on the Sun (Cattaneo 1999, Cattaneo and Hughes 2001, Hagenaar 2001) and will not affect the open flux, polar field or toroidal flux loss.

Simulated magnetograms of the type generated here are an important input to reconstructions of the past solar irradiance. Thus, Dasi-Espuig et al. (2014, 2016) used the previous version of the model, which employed only historic sunspot observations as input, to reconstruct solar total and spectral irradiance back to 1878 and 1700, respectively. To include the contribution of the smaller regions, which is critical for an estimate of the secular irradiance variability, they had to add it separately from a simpler model (Solanki et al. 2002, Vieira and Solanki 2010, Krivova et al. 2007, 2010). The weakness of this approach lies therein that because the emergence rate of ERs was linked linearly to the emergence of active regions, the model returned zero magnetic flux at times when no sunspots emerged on the Sun for an extended period, which contradicts observations. This shortcoming is overcome by representing the BMR emergence rate by a single power-law distribution with an exponent depending on the solar activity, as used here (see also Krivova et al. 2021). The new model should thus allow a better constraint on the secular variability of solar irradiance.

#### **Acknowledgements**

We thank Kok Leng Yeo for providing the composite of total magnetic flux measurements and Mike Lockwood for providing the open magnetic flux reconstruction from the *aa*-index. BH was supported by the International Max-Planck Research School (IMPRS) for Solar System Science at the University of Göttingen.

## 4 Summary & Outlook

“Happiness can be found in the darkest of times, if one only remembers to turn on the light.”

---

*Prof. Albus Dumbledore*

‘Harry Potter and the Prisoner of Azkaban’

### 4.1 Summary

Precise knowledge of past solar activity and variability is crucial to understand the Sun’s influence on life on Earth. This requires also understanding of the solar magnetic field which drives solar activity. Direct measurements of the solar magnetic field however only exist since a few decades. On longer timescales reconstructions can be made from direct or indirect proxies of solar activity. The longest direct proxies are sunspot records which have been recorded since the early 17th century. Sunspots form in active regions (ARs), large bipolar magnetic regions (BMRs) that emerge on the solar surface throughout a roughly 11-year cycle as a result of the dynamo process which generates the solar magnetic field in its interior. The dynamo process also gives rise to a large number of smaller BMRs which emerge on the solar surface alongside ARs. They are called ephemeral regions (ERs). Although ERs are short-lived compared to their larger counterparts, they have a significant contribution to the total magnetic flux budget due to their much higher emergence rate. ERs are also thought to play an essential role in the secular variation of solar activity and the solar magnetic field. ERs are however more difficult to observe and so they are missing completely from sunspot records. Therefore, while the emergence and evolution of ARs have been extensively studied and modelled, a realistic model of individual small BMRs is still pending. Thus, the aim of this thesis is to study the evolution of small BMRs and their influence on the solar magnetic field.

As described in Chap. 2, the reconstruction of solar activity from sunspot records is particularly difficult during periods with no emerging sunspots, such as the Maunder Minimum. The fundamental problem behind this is the absence of any information on the emergence of ERs on long timescales, such that the emergence of both AR and ERs has to be derived from sunspot observations alone. In earlier models, the emergence rate ERs was directly related to that of sunspots so that zero magnetic flux emerges in the prolonged absence of sunspots. This contradicts independent reconstructions from cosmogenic isotopes which indicate low but continued activity during such grand minima periods. We

first developed a new description of the emergence rate based on two separate observations: (a) All BMRs follow a single power-law size distribution, from the largest ARs down to ERs and internetwork elements (Thornton and Parnell 2011). (b) The number of ARs diminishes by a factor of  $\sim 8$  between solar maximum and minimum, while the number of ERs changes by only a factor of  $\sim 2$  (Harvey 1993, H93). We found that both observations can be satisfied by a single power-law size distribution, where the exponent varies with the sunspot number. The updated emergence rate was then used as input to a coarse physical model describing the evolution of the solar total and open magnetic flux through a system of ordinary differential equations (Solanki et al. 2000, 2002, Vieira and Solanki 2010). The calculated magnetic flux agrees well with observations and independent reconstructions from different proxy models since 1610. Importantly, the level of the magnetic flux during the Maunder minimum agrees with cosmogenic isotope data, resolving the major shortcoming of the previous emergence model. In the study by Usoskin et al. (2021b), the updated emergence model was statistically inverted to reconstruct the sunspot number since 971 from annual  $^{14}\text{C}$  data (Brehm et al. 2021). This made it possible to resolve individual solar cycles over the last millennium for the very first time. Additionally, the emergence model was used to study the time lag between galactic cosmic ray (GCR) flux, the sunspot number and the open magnetic flux calculated from our model (Koldobskiy et al. 2022). It was confirmed that the open magnetic flux is a good index of the heliospheric GCR modulation.

In Chap. 3 we studied the role of small BMRs to the magnetic field evolution through (a) numerical simulations and (b) theoretical approximations (see Sect. 3.7). For (a), we took the emergence model developed in Chap. 2, but instead of calculating global quantities, we modelled the evolution of the solar magnetic field from a simulated magnetogram calculated by a SFTM. The SFTM has the advantage that the evolution of each individual BMR is tracked, from its initial emergence to its decay or transport to the solar poles by the surface flows. This does not only increase the accuracy of the reconstruction, but makes it possible to study additional solar quantities such as the polar field strength or the toroidal flux loss. However, the SFTM also needs more input information, namely the emergence latitude, tilt angle and size (or magnetic flux content) of each individual region. The mean emergence latitude, latitude scatter and mean tilt angle of ARs have been modelled in a statistical way from the RGO/SOON sunspot group record by Jiang et al. 2011a (J11) and Jiang (2020). We adopted their approach for all BMRs, partly revising and extending the relationships based on additional solar observations: First of all, we included a scatter of tilt angles into our study, which increased for smaller BMRs according to observations by H93 and Schunker et al. (2020). Similarly, the latitude scatter of ARs by J11 was also modified to increase for smaller BMRs. The latitude and tilt angle scatter are thereby described by Gaussian distributions around the mean. Next, we extended the relationship for the mean emergence latitude so that BMRs of a new cycle may emerge during overlap periods with neighboring cycles based on observational constraints from H93 and the RGO/SOON record. The emergence onset happens progressively later for larger BMRs. We also included the effect of activity nests, which is an increased emergence rate of new BMRs in the vicinity of already existing ARs. From the derived (statistical) relationships, we calculated multiple semi-synthetic BMRs records (100 realizations) using only the sunspot number, cycle amplitude (maximum smoothed sunspot number) and the dates of solar minima and maxima as input. Due to

computational limitations, we did not include the smallest BMRs into the simulation, but considered all regions larger than  $2 \times 10^{20}$  Mx (lifetime of 1 day or more), which is a factor of 100 more regions than present in the RGO/SOON sunspot group record. Finally we adjusted the SFTM itself. We obtained the magnetic flux of each region directly from the power-law size distribution. The width of a BMR determines the speed of decay in the SFTM and so we modelled the shape of the BMRs to match the observed e-folding lifetimes. For comparison with earlier versions, we ran the SFTM with the original setup by [Jiang et al. \(2011b\)](#). This version used the RGO/SOON data as input and calculated the shape of ARs from the sunspot area. Our simulations agree well with the total magnetic flux of ground-based observatories, thereby improving the previous model that needed a free parameter to retroactively adjust the peak magnetic field strength of the BMRs. We also find agreement between our simulation and the open magnetic flux from independent reconstructions, the observed polar field strength by WSO and the toroidal flux loss derived from WSO magnetograms ([Jeffers et al. 2022](#)). To study the influence of the newly added small BMRs, we separated the contributions of large BMRs with sunspots (more than  $3 \times 10^{21}$  Mx, LMR) from the smaller BMRs (SMR). We found that: (i) at solar minimum, the total and open magnetic flux of SMR are comparable to those of LMR, (ii) at solar maximum the contribution of LMR is about twice that of SMR, (iii) for the polar fields and toroidal flux loss the contribution of SMR is comparable to LMR at all activity levels and (iv) The noise of all four observables – described by the standard deviation between the 100 individual runs – is dominated by LMR. All of our simulation results were consistent with our theoretical estimate in Sect. 3.7. Our study highlights the importance of small BMRs during all levels of solar activity. At activity minimum, small BMRs provide a significant contribution to all the solar quantities in our study. At solar maximum, the polar fields and the toroidal flux loss are also equally contributed to by small and large BMRs. This makes our study interesting for solar dynamo studies as both the polar fields and the toroidal flux loss are crucial to understanding the generation of poloidal field from the toroidal field on the solar surface in the Babcock-Leighton dynamo (see Sect. 1.3.1). Small BMRs are further observed to have a stabilizing effect on the simulations, especially for the polar field reversals. This is due to the high number of emerging regions which smears out the effects of individual outliers.

## 4.2 Outlook

An important application of our emergence model (see Chap. 2) is the reconstruction of total solar irradiance (TSI). It has been shown by [Dasi-Espuig et al. \(2014, 2016\)](#) that the TSI can be reconstructed from the simulated magnetograms with a SFTM using historic sunspot observations. A critical part of the TSI reconstruction is the secular variation which is crucial for climate studies to estimate the solar forcing on terrestrial climate change. The secular variation is driven by small BMRs, missing from the sunspot records, so that the contribution by ERs was added separately from the simpler model by [Solanki et al. \(2000, 2002\)](#), [Vieira and Solanki \(2010\)](#) described in Sect. 2.4.1. This model linked the ER emergence rate linearly to the sunspot number which returns zero magnetic flux in the absence of sunspots, contradicting observations from cosmogenic isotopes (e.g. [Wu et al. 2018a](#)). With this improved emergence model developed in Chap. 2 we were

able to reproduce the mean level of the open magnetic flux derived from cosmogenic isotopes during the Maunder minimum, which fixes the major shortcoming of the previous model. The improved emergence model will lead to a smaller secular TSI variation during very low solar activity and allow a more reliable estimate of the rise in TSI since the Maunder minimum (1645-1715). Another improvement to the reconstruction by [Dasi-Espuig et al. \(2014, 2016\)](#) can be done with the updated version of the SFTM presented in Chap. 3, which allows the inclusion of small BMRs down to  $2 \times 10^{20}$  Mx into the model. We have shown that this SFTM can reproduce the entire total magnetic flux measured by ground based observatories. Therefore we can reconstruct the TSI solely from the simulated magnetograms, without a separate treatment of ERs. This will further increase the accuracy in the calculation of the secular variation.

Here, we have not yet included the smallest BMRs below  $2 \times 10^{20}$  Mx into the SFTM simulation. Including those smaller regions would further improve the reconstruction of the secular variation of solar activity. This requires an increase in the spatial and temporal resolution which would require significantly higher computational resources. Further, the inclusion of smaller BMRs into the SFTM would also increase the amount of flux cancellation, since many of the small BMRs would emerge within one of the polarity of a large BMRs, partly cancelling their magnetic flux, see [Nèmec et al. \(2022\)](#).

Despite the major updates to the emergence model in Chap. 2, further improvements are still possible. Reconstructions from isotopes evidence that variations in the solar activity continued even during a grand solar minimum. This indicates that the activity can actually fall below the minimum level of our emergence model at zero sunspots. Such variations are however not captured by the sunspot number which can never fall below zero. To estimate the variation in the magnetic flux during spotless periods, one could instead consider the frequency of spotless days within a certain time period (e.g. within a year). Such a "spotless day fraction" can be used to derive a formal "negative" sunspot number and thereby estimate the activity level during periods almost devoid of sunspots.

Some improvements can also be made for the empirical relationships derived in Sect. 1.2.4. For example, we have assumed that anti-Hale regions (regions that violate Hale's law, see Sect. 1.2.4) are randomly "flipped" regions due to the tilt angle scatter modelled as a Gaussian distribution. However, recent observations of ARs suggest that anti-Hale regions might actually be a separate population with preferably low tilt angles obeying Joy's law (e.g. [Li 2018](#), [Muñoz-Jaramillo et al. 2021](#)). Introducing such a separate anti-Hale population while decreasing the tilt angle scatter would increase the amount of low tilt angle anti-Hale regions and reduce the amount of high tilt angle regions. This would lead to a slight decrease in the polar field strength and a slight increase in the toroidal flux loss.

Further, we made the assumption that the emergence latitude scatter follows a symmetrical Gaussian distribution around the mean. However, studies (e.g. [Solanki et al. 2008](#)) have found that the latitude distribution of BMRs is not symmetrical around the mean, but skewed toward the equator so that there are more low latitude BMRs. This might have effect on the strength and reversal times of the polar field as well as on the toroidal flux loss.

# Bibliography

- Adelberger, E. G., García, A., Robertson, R. G. H., Snover, K. A., Balantekin, A. B., Heeger, K., Ramsey-Musolf, M. J., Bemmerer, D., Junghans, A., Bertulani, C. A., Chen, J. W., Costantini, H., Prati, P., Couder, M., Uberseder, E., Wiescher, M., Cyburt, R., Davids, B., Freedman, S. J., Gai, M., Gazit, D., Gialanella, L., Imbriani, G., Greife, U., Hass, M., Haxton, W. C., Itahashi, T., Kubodera, K., Langanke, K., Leitner, D., Leitner, M., Vetter, P., Winslow, L., Marcucci, L. E., Motobayashi, T., Mukhamedzhanov, A., Tribble, R. E., Nollett, K. M., Nunes, F. M., Park, T. S., Parker, P. D., Schiavilla, R., Simpson, E. C., Spitaleri, C., Strieder, F., Trautvetter, H. P., Suemmerer, K., Typel, S., 2011, Solar fusion cross sections. II. The pp chain and CNO cycles, *Reviews of Modern Physics*, 83, 195–246, [1004.2318](#)
- Agostini, M., Altenmüller, K., Appel, S., Atroshchenko, V., Bagdasarian, Z., Basilico, D., Bellini, G., Benziger, J., Biondi, R., Bravo, D., Caccianiga, B., Calaprice, F., Caminata, A., Cavalcante, P., Chepurinov, A., D'Angelo, D., Davini, S., Derbin, A., Di Giacinto, A., Di Marcello, V., Ding, X. F., Di Ludovico, A., Di Noto, L., Drachnev, I., Formozov, A., Franco, D., Galbiati, C., Ghiano, C., Giammarchi, M., Goretti, A., Göttel, A. S., Gromov, M., Guffanti, D., Ianni, A., Ianni, A., Jany, A., Jeschke, D., Kobychhev, V., Korga, G., Kumaran, S., Laubenstein, M., Litvinovich, E., Lombardi, P., Lomskeya, I., Ludhova, L., Lukyanchenko, G., Lukyanchenko, L., Machulin, I., Martyn, J., Meroni, E., Meyer, M., Miramonti, L., Misiaszek, M., Muratova, V., Neumair, B., Nieslony, M., Nugmanov, R., Oberauer, L., Orekhov, V., Ortica, F., Pallavicini, M., Papp, L., Pelicci, L., Penek, Ö., Pietrofaccia, L., Pilipenko, N., Pocar, A., Raikov, G., Ranalli, M. T., Ranucci, G., Razeto, A., Re, A., Redchuk, M., Romani, A., Rossi, N., Schönert, S., Semenov, D., Settanta, G., Skorokhvatov, M., Singhal, A., Smirnov, O., Sotnikov, A., Suvorov, Y., Tartaglia, R., Testera, G., Thurn, J., Unzhakov, E., Villante, F. L., Vishneva, A., Vogelaar, R. B., von Feilitzsch, F., Wojcik, M., Wurm, M., Zavatarelli, S., Zuber, K., Zuzel, G., The Borexino Collaboration, 2020, Experimental evidence of neutrinos produced in the CNO fusion cycle in the Sun, *Nature*, 587, 577–582, [2006.15115](#)
- Anders, E., Grevesse, N., 1989, Abundances of the elements: Meteoritic and solar, *Geochim. Cosmochim. Acta*, 53, 197–214
- Anusha, L. S., Solanki, S. K., Hirzberger, J., Feller, A., 2017, Statistical evolution of quiet-Sun small-scale magnetic features using Sunrise observations, *A&A*, 598, A47, [1608.08499](#)

- Arge, C. N., Hildner, E., Pizzo, V. J., Harvey, J. W., 2002, Two solar cycles of nonincreasing magnetic flux, *Journal of Geophysical Research (Space Physics)*, 107, 1319
- Asplund, M., Grevesse, N., Sauval, A. J., Scott, P., 2009, The Chemical Composition of the Sun, *ARA&A*, 47, 481–522, [0909.0948](#)
- Asplund, M., Amarsi, A. M., Grevesse, N., 2021, The chemical make-up of the Sun: A 2020 vision, *A&A*, 653, A141, [2105.01661](#)
- Babcock, H. D., 1959, The Sun's Polar Magnetic Field., *ApJ*, 130, 364
- Babcock, H. W., 1961, The Topology of the Sun's Magnetic Field and the 22-YEAR Cycle., *ApJ*, 133, 572
- Bai, T., 1988, Distribution of Flares on the Sun during 1955–1985: “Hot Spots” (Active Zones) Lasting for 30 Years, *ApJ*, 328, 860
- Balmaceda, L., Krivova, N. A., Solanki, S. K., 2007, Reconstruction of solar irradiance using the Group sunspot number, *Advances in Space Research*, 40, 986–989, [astro-ph/0703147](#)
- Balmaceda, L. A., Solanki, S. K., Krivova, N. A., Foster, S., 2009, A homogeneous database of sunspot areas covering more than 130 years, *Journal of Geophysical Research (Space Physics)*, 114, A07104, [0906.0942](#)
- Baranyi, T., 2015, Comparison of Debrecen and Mount Wilson/Kodaikanal sunspot group tilt angles and the Joy's law, *MNRAS*, 447, 1857–1865, [1412.1355](#)
- Baranyi, T., Györi, L., Ludmány, A., 2016, On-line Tools for Solar Data Compiled at the Debrecen Observatory and Their Extensions with the Greenwich Sunspot Data, *Sol. Phys.*, 291, 3081–3102, [1606.00669](#)
- Bard, E., Raisbeck, G. M., Yiou, F., Jouzel, J., 1997, Solar modulation of cosmogenic nuclide production over the last millennium: comparison between  $^{14}\text{C}$  and  $^{10}\text{Be}$  records, *Earth and Planetary Science Letters*, 150, 453–462
- Baumann, I., Schmitt, D., Schüssler, M., Solanki, S. K., 2004, Evolution of the large-scale magnetic field on the solar surface: A parameter study, *A&A*, 426, 1075–1091
- Baumann, I., Schmitt, D., Schüssler, M., 2006, A necessary extension of the surface flux transport model, *A&A*, 446, 307–314
- Beer, J., Blinov, A., Bonani, G., Finkel, R. C., Hofmann, H. J., Lehmann, B., Oeschger, H., Sigg, A., Schwander, J., Staffelbach, T., Stauffer, B., Suter, M., Wöflfi, W., 1990, Use of  $^{10}\text{Be}$  in polar ice to trace the 11-year cycle of solar activity, *Nature*, 347, 164–166
- Beer, J., Tobias, S., Weiss, N., 1998, An Active Sun Throughout the Maunder Minimum, *Sol. Phys.*, 181, 237–249
- Beer, J., McCracken, K., von Steiger, R., 2012, *Cosmogenic Radionuclides*

- Belov, A., 2000, Large Scale Modulation: View From the Earth, *Space Sci. Rev.*, 93, 79–105
- Berdyugina, S. V., Usoskin, I. G., 2003, Active longitudes in sunspot activity: Century scale persistence, *A&A*, 405, 1121–1128
- Bray, R. J., Loughhead, R. E., 1979, Sunspots.
- Brehm, N., Bayliss, A., Christl, M., Synal, H.-A., Adolphi, F., Beer, J., Kromer, B., Muscheler, R., Solanki, S. K., Usoskin, I., Bleicher, N., Bollhalder, S., Tyers, C., Wacker, L., 2021, Eleven-year solar cycles over the last millennium revealed by radiocarbon in tree rings, *Nat. Geosci.*, 14, 10–15
- Buehler, D., Lagg, A., Solanki, S. K., 2013, Quiet Sun magnetic fields observed by Hinode: Support for a local dynamo, *A&A*, 555, A33, [1307.0789](#)
- Bumba, V., Howard, R., 1965, Large-Scale Distribution of Solar Magnetic Fields., *ApJ*, 141, 1502
- Calogovic, J., Albert, C., Arnold, F., Beer, J., Desorgher, L., Flueckiger, E. O., 2010, Sudden cosmic ray decreases: No change of global cloud cover, *Geophys. Res. Lett.*, 37, L03802
- Cameron, R., Schüssler, M., 2015, The crucial role of surface magnetic fields for the solar dynamo, *Science*, 347, 1333–1335, [1503.08469](#)
- Cameron, R. H., Schüssler, M., 2020, Loss of toroidal magnetic flux by emergence of bipolar magnetic regions, *A&A*, 636, A7, [2002.05436](#)
- Cameron, R. H., Jiang, J., Schmitt, D., Schüssler, M., 2010, Surface Flux Transport Modeling for Solar Cycles 15-21: Effects of Cycle-Dependent Tilt Angles of Sunspot Groups, *ApJ*, 719, 264–270, [1006.3061](#)
- Carlsson, M., Stein, R. F., Nordlund, Å., Scharmer, G. B., 2004, Observational Manifestations of Solar Magnetoconvection: Center-to-Limb Variation, *ApJ*, 610, L137–L140, [astro-ph/0406160](#)
- Carrington, R. C., 1858, On the Distribution of the Solar Spots in Latitudes since the Beginning of the Year 1854, with a Map, *MNRAS*, 19, 1–3
- Carrington, R. C., 1859, Description of a Singular Appearance seen in the Sun on September 1, 1859, *MNRAS*, 20, 13–15
- Castenmiller, M. J. M., Zwaan, C., van der Zalm, E. B. J., 1986, Sunspot Nests - Manifestations of Sequences in Magnetic Activity, *Sol. Phys.*, 105, 237–255
- Cattaneo, F., 1999, On the Origin of Magnetic Fields in the Quiet Photosphere, *ApJ*, 515, L39–L42
- Cattaneo, F., Hughes, D. W., 2001, Solar dynamo theory : Solar dynamo theory: a new look at the origin of small-scale magnetic fields, *Astronomy and Geophysics*, 42, 3.18–3.22

- Charbonneau, P., 1995, Genetic algorithms in astronomy and astrophysics, *The Astrophysical Journal Suppl. Ser.*, 101, 309
- Charbonneau, P., 2020, Dynamo models of the solar cycle, *Living Reviews in Solar Physics*, 17, 4
- Chatzistergos, T., Usoskin, I. G., Kovaltsov, G. A., Krivova, N. A., Solanki, S. K., 2017, New reconstruction of the sunspot group numbers since 1739 using direct calibration and “backbone” methods, *A&A*, 602, A69, [1702.06183](#)
- Christensen-Dalsgaard, J., 2021, Solar structure and evolution, *Living Reviews in Solar Physics*, 18, 2, [2007.06488](#)
- Clette, F., Lefèvre, L., 2016, The New Sunspot Number: Assembling All Corrections, *Sol. Phys.*, 291, 2629–2651
- Clette, F., Berghmans, D., Vanlommel, P., Van der Linden, R. A. M., Koeckelenbergh, A., Wauters, L., 2007, From the Wolf number to the International Sunspot Index: 25 years of SIDC, *Advances in Space Research*, 40, 919–928
- Clette, F., Svalgaard, L., Vaquero, J. M., Cliver, E. W., 2014, Revisiting the Sunspot Number. A 400-Year Perspective on the Solar Cycle, *Space Sci. Rev.*, 186, 35–103, [1407.3231](#)
- Cliver, E. W., Ling, A. G., 2016, The Discontinuity Circa 1885 in the Group Sunspot Number, *Sol. Phys.*, 291, 2763–2784
- Cranmer, S. R., 2002, Coronal Holes and the High-Speed Solar Wind, *Space Sci. Rev.*, 101, 229–294
- Crooker, N. U., Gosling, J. T., Kahler, S. W., 2002, Reducing heliospheric magnetic flux from coronal mass ejections without disconnection, *Journal of Geophysical Research (Space Physics)*, 107, 1028
- Crucifix, M., Loutre, M. F., Berger, A., 2006, The Climate Response to the Astronomical Forcing, *Space Sci. Rev.*, 125, 213–226
- Damon, P. E., Lerman, J. C., Long, A., 1978, Temporal Fluctuations of Atmospheric <sup>14</sup>C: Causal Factors and Implications, *Annual Review of Earth and Planetary Sciences*, 6, 457
- Dasi-Espuig, M., Solanki, S. K., Krivova, N. A., Cameron, R., Peñuela, T., 2010, Sunspot group tilt angles and the strength of the solar cycle, *A&A*, 518, A7, [1005.1774](#)
- Dasi-Espuig, M., Jiang, J., Krivova, N. A., Solanki, S. K., 2014, Modelling total solar irradiance since 1878 from simulated magnetograms, *A&A*, 570, A23, [1409.1941](#)
- Dasi-Espuig, M., Jiang, J., Krivova, N. A., Solanki, S. K., Unruh, Y. C., Yeo, K. L., 2016, Reconstruction of spectral solar irradiance since 1700 from simulated magnetograms, *A&A*, 590, A63, [1605.02039](#)

- De Moortel, I., Browning, P., 2015, Recent advances in coronal heating, *Philosophical Transactions of the Royal Society of London Series A*, 373, 20140 269–20140 269, [1510.00977](#)
- Delaygue, G., Bard, E., 2011, An Antarctic view of Beryllium-10 and solar activity for the past millennium, *Climate Dynamics*, 36, 2201–2218
- DeVore, C. R., Boris, J. P., Sheeley, N. R., J., 1984, The concentration of the large-scale solar magnetic field by a meridional surface flow, *Sol. Phys.*, 92, 1–14
- DeVore, C. R., Boris, J. P., Young, T. R., J., Sheeley, N. R., Harvey, K. L., 1985, Numerical simulations of large-scale solar magnetic fields, *Australian Journal of Physics*, 38, 999–1007
- Dewitte, S., Crommelynck, D., Joukoff, A., 2004, Total solar irradiance observations from DIARAD/VIRGO, *Journal of Geophysical Research (Space Physics)*, 109, A02102
- Dikpati, M., Gilman, P. A., 2009, Flux-Transport Solar Dynamos, *Space Sci. Rev.*, 144, 67–75
- Dudok de Wit, T., Kopp, G., Fröhlich, C., Schöll, M., 2017, Methodology to create a new total solar irradiance record: Making a composite out of multiple data records, *Geophys. Res. Lett.*, 44, 1196–1203, [1702.02341](#)
- Dunne, E. M., Gordon, H., Kürten, A., Almeida, J., Duplissy, J., Williamson, C., Ortega, I. K., Pringle, K. J., Adamov, A., Baltensperger, U., Barmet, P., Benduhn, F., Bianchi, F., Breitenlechner, M., Clarke, A., Curtius, J., Dommen, J., Donahue, N. M., Ehrhart, S., Flagan, R. C., Franchin, A., Guida, R., Hakala, J., Hansel, A., Heinritzi, M., Jokinen, T., Kangasluoma, J., Kirkby, J., Kulmala, M., Kupc, A., Lawler, M. J., Lehtipalo, K., Makhmutov, V., Mann, G., Mathot, S., Merikanto, J., Miettinen, P., Nenes, A., Onnela, A., Rap, A., Reddington, C. L. S., Riccobono, F., Richards, N. A. D., Rissanen, M. P., Rondo, L., Sarnela, N., Schobesberger, S., Sengupta, K., Simon, M., Sipilä, M., Smith, J. N., Stozkhov, Y., Tomé, A., Tröstl, J., Wagner, P. E., Wimmer, D., Winkler, P. M., Worsnop, D. R., Carslaw, K. S., 2016, Global atmospheric particle formation from CERN CLOUD measurements, *Science*, 354, 1119–1124
- Duvall, T. L., J., 1979, Large-scale solar velocity fields., *Sol. Phys.*, 63, 3–15
- Eddy, J. A., 1976, The Maunder Minimum, *Science*, 192, 1189–1202
- Feynman, J., Ruzmaikin, A., 2014, The Centennial Gleissberg Cycle and its association with extended minima, *Journal of Geophysical Research (Space Physics)*, 119, 6027–6041
- Fligge, M., Solanki, S. K., Beer, J., 1999, Determination of solar cycle length variations using the continuous wavelet transform, *A&A*, 346, 313–321
- Fligge, M., Solanki, S. K., Unruh, Y. C., 2000, Modelling irradiance variations from the surface distribution of the solar magnetic field, *A&A*, 353, 380–388

- Floyd, L. E., Cook, J. W., Herring, L. C., Crane, P. C., 2003, SUSIM'S 11-year observational record of the solar UV irradiance, *Advances in Space Research*, 31, 2111–2120
- Fröhlich, C., 2006, Solar Irradiance Variability Since 1978. Revision of the PMOD Composite during Solar Cycle 21, *Space Sci. Rev.*, 125, 53–65
- Fröhlich, C., 2012, Total Solar Irradiance Observations, *Surveys in Geophysics*, 33, 453–473
- Gaizauskas, V., Harvey, K. L., Harvey, J. W., Zwaan, C., 1983, Large-scale patterns formed by solar active regions during the ascending phase of cycle 21, *ApJ*, 265, 1056–1065
- Garcia, A., Mouradian, Z., 1998, The Gleissberg Cycle of Minima, *Sol. Phys.*, 180, 495–498
- Gleissberg, W., 1939, A long-periodic fluctuation of the sun-spot numbers, *The Observatory*, 62, 158–159
- González Hernández, I., Kholikov, S., Hill, F., Howe, R., Komm, R., 2008, Subsurface Meridional Circulation in the Active Belts, *Sol. Phys.*, 252, 235–245, [0808.3606](#)
- Gordon, H., Kirkby, J., Baltensperger, U., Bianchi, F., Breitenlechner, M., Curtius, J., Dias, A., Dommen, J., Donahue, N. M., Dunne, E. M., Duplissy, J., Ehrhart, S., Flanagan, R. C., Frege, C., Fuchs, C., Hansel, A., Hoyle, C. R., Kulmala, M., Kürten, A., Lehtipalo, K., Makhmutov, V., Molteni, U., Rissanen, M. P., Stozkhov, Y., Tröstl, J., Tsagkogeorgas, G., Wagner, R., Williamson, C., Wimmer, D., Winkler, P. M., Yan, C., Carslaw, K. S., 2017, Causes and importance of new particle formation in the present-day and preindustrial atmospheres, *Journal of Geophysical Research (Atmospheres)*, 122, 8739–8760
- Gray, L. J., Beer, J., Geller, M., Haigh, J. D., Lockwood, M., Matthes, K., Cubasch, U., Fleitmann, D., Harrison, G., Hood, L., Luterbacher, J., Meehl, G. A., Shindell, D., van Geel, B., White, W., 2010, Solar Influences on Climate, *Reviews of Geophysics*, 48, RG4001
- Grevesse, N., Sauval, A. J., 1998, Standard Solar Composition, *Space Sci. Rev.*, 85, 161–174
- Grossmann-Doerth, U., Knoelker, M., Schuessler, M., Solanki, S. K., 1994, The deep layers of solar magnetic elements, *A&A*, 285, 648–654
- Haber, D. A., Hindman, B. W., Toomre, J., Bogart, R. S., Larsen, R. M., Hill, F., 2002, Evolving Submerged Meridional Circulation Cells within the Upper Convection Zone Revealed by Ring-Diagram Analysis, *ApJ*, 570, 855–864
- Hagenaar, H. J., 2001, Ephemeral Regions on a Sequence of Full-Disk Michelson Doppler Imager Magnetograms, *ApJ*, 555, 448–461

- Hagenaar, H. J., Schrijver, C. J., Title, A. M., 2003, The Properties of Small Magnetic Regions on the Solar Surface and the Implications for the Solar Dynamo(s), *ApJ*, 584, 1107–1119
- Haigh, J. D., 2007, The Sun and the Earth's Climate, *Living Reviews in Solar Physics*, 4, 2
- Hale, G. E., Nicholson, S. B., 1925, The Law of Sun-Spot Polarity, *ApJ*, 62, 270
- Hale, G. E., Ellerman, F., Nicholson, S. B., Joy, A. H., 1919, The Magnetic Polarity of Sun-Spots, *ApJ*, 49, 153
- Hanasoge, S. M., 2022, Surface and interior meridional circulation in the Sun, *Living Reviews in Solar Physics*, 19, 3
- Harvey, J. W., Hill, F., Hubbard, R. P., Kennedy, J. R., Leibacher, J. W., Pintar, J. A., Gilman, P. A., Noyes, R. W., Title, A. M., Toomre, J., Ulrich, R. K., Bhatnagar, A., Kennewell, J. A., Marquette, W., Patron, J., Saa, O., Yasukawa, E., 1996, The Global Oscillation Network Group (GONG) Project, *Science*, 272, 1284–1286
- Harvey, K. L., 1992, The Cyclic Behavior of Solar Activity, in *The Solar Cycle*, (Ed.) K. L. Harvey, vol. 27 of *Astronomical Society of the Pacific Conference Series*, p. 335
- Harvey, K. L., 1993, Magnetic Bipoles on the Sun, Ph.D. thesis, Univ. Utrecht
- Harvey, K. L., 1994, The solar magnetic cycle, in *Solar Surface Magnetism*, (Eds.) R. J. Rutten, C. J. Schrijver, vol. 433 of *NATO Advanced Study Institute (ASI) Series C*, p. 347
- Harvey, K. L., Martin, S. F., 1973, Ephemeral Active Regions, *Sol. Phys.*, 32, 389–402
- Harvey, K. L., Zwaan, C., 1993, Properties and emergence of bipolar active regions, *Sol. Phys.*, 148, 85–118
- Hathaway, D. H., 1996, Doppler Measurements of the Sun's Meridional Flow, *ApJ*, 460, 1027
- Hathaway, D. H., 2015, The Solar Cycle, *Living Reviews in Solar Physics*, 12, 4, [1502.07020](#)
- Hathaway, D. H., Wilson, R. M., Reichmann, E. J., 2002, Group Sunspot Numbers: Sunspot Cycle Characteristics, *Sol. Phys.*, 211, 357–370
- Herschel, W., 1801, Observations Tending to Investigate the Nature of the Sun, in Order to Find the Causes or Symptoms of Its Variable Emission of Light and Heat; With Remarks on the Use That May Possibly Be Drawn from Solar Observations, *Philosophical Transactions of the Royal Society of London Series I*, 91, 265–318
- Hickey, J. R., Stowe, L. L., Jacobowitz, H., Pellegrino, P., Maschhoff, R. H., House, F., Vonder Haar, T. H., 1980, Initial Solar Irradiance Determinations from Nimbus 7 Cavity Radiometer Measurements, *Science*, 208, 281–283

- Hoeksema, J. T., Wilcox, J. M., Scherrer, P. H., 1983, The structure of the heliospheric current sheet: 1978-1982, *J. Geophys. Res.*, 88, 9910–9918
- Howard, R., Gilman, P. I., Gilman, P. A., 1984, Rotation of the sun measured from Mount Wilson white-light images, *ApJ*, 283, 373–384
- Howard, R. F., 1991, Axial Tilt Angles of Sunspot Groups, *Sol. Phys.*, 136, 251–262
- Howard, R. F., Gupta, S. S., Sivaraman, K. R., 1999, Measurement of Kodaikanal White-Light Images - II. Rotation Comparison and Merging with Mount Wilson Data, *Sol. Phys.*, 186, 25–41
- Howe, R., 2009, Solar Interior Rotation and its Variation, *Living Reviews in Solar Physics*, 6, 1, [0902.2406](#)
- Hoyt, D. V., Schatten, K. H., 1998, Group Sunspot Numbers: A New Solar Activity Reconstruction, *Sol. Phys.*, 181, 491–512
- Ikhsanov, R. N., Ivanov, V. G., 1999, Properties of space and time distribution of solar coronal holes, *Sol. Phys.*, 188, 245–258
- Jeffers, S. V., Cameron, R. H., Marsden, S. C., Boro Saikia, S., Folsom, C. P., Jardine, M. M., Morin, J., Petit, P., See, V., Vidotto, A. A., Wolter, U., Mittag, M., 2022, The crucial role of surface magnetic fields for stellar dynamos:  $\epsilon$  Eridani, 61 Cygni A, and the Sun, *A&A*, 661, A152, [2201.07530](#)
- Jha, B. K., Karak, B. B., Mandal, S., Banerjee, D., 2020, Magnetic Field Dependence of Bipolar Magnetic Region Tilts on the Sun: Indication of Tilt Quenching, *ApJ*, 889, L19, [1912.13223](#)
- Jiang, J., 2020, Nonlinear Mechanisms that Regulate the Solar Cycle Amplitude, *ApJ*, 900, 19, [2007.07069](#)
- Jiang, J., Cameron, R. H., Schmitt, D., Schüssler, M., 2011a, The solar magnetic field since 1700. I. Characteristics of sunspot group emergence and reconstruction of the butterfly diagram, *A&A*, 528, A82, [1102.1266](#)
- Jiang, J., Cameron, R. H., Schmitt, D., Schüssler, M., 2011b, The solar magnetic field since 1700. II. Physical reconstruction of total, polar and open flux, *A&A*, 528, A83, [1102.1270](#)
- Jiang, J., Cameron, R. H., Schmitt, D., Schüssler, M., 2013, Can Surface Flux Transport Account for the Weak Polar Field in Cycle 23?, *Space Sci. Rev.*, 176, 289–298, [1104.4183](#)
- Jiang, J., Cameron, R. H., Schüssler, M., 2014a, Effects of the Scatter in Sunspot Group Tilt Angles on the Large-scale Magnetic Field at the Solar Surface, *ApJ*, 791, 5, [1406.5564](#)

- Jiang, J., Hathaway, D. H., Cameron, R. H., Solanki, S. K., Gizon, L., Upton, L., 2014b, Magnetic Flux Transport at the Solar Surface, *Space Sci. Rev.*, 186, 491–523, [1408.3186](#)
- Jiang, J., Cameron, R. H., Schüssler, M., 2015, The Cause of the Weak Solar Cycle 24, *ApJ*, 808, L28, [1507.01764](#)
- Jones, H. P., Duvall, Thomas L., J., Harvey, J. W., Mahaffey, C. T., Schwitters, J. D., Simmons, J. E., 1992, The NASA/NSO Spectromagnetograph, *Sol. Phys.*, 139, 211–232
- Jung, J., Oh, S., Yi, Y., Evenson, P., Pyle, R., Jee, G., Kim, J.-H., Lee, C., Sohn, J., 2016, Installation of Neutron Monitor at the Jang Bogo Station in Antarctica, *Journal of Astronomy and Space Sciences*, 33, 345–348
- Keller, C. U., Schüssler, M., Vögler, A., Zakharov, V., 2004, On the Origin of Solar Faculae, *ApJ*, 607, L59–L62
- Kirkby, J., Curtius, J., Almeida, J., Dunne, E., Duplissy, J., Ehrhart, S., Franchin, A., Gagné, S., Ickes, L., Kürten, A., Kupc, A., Metzger, A., Riccobono, F., Rondo, L., Schobesberger, S., Tsagkogeorgas, G., Wimmer, D., Amorim, A., Bianchi, F., Breitenlechner, M., David, A., Dommen, J., Downard, A., Ehn, M., Flagan, R. C., Haider, S., Hansel, A., Hauser, D., Jud, W., Junninen, H., Kreissl, F., Kvashin, A., Laaksonen, A., Lehtipalo, K., Lima, J., Lovejoy, E. R., Makhmutov, V., Mathot, S., Mikkilä, J., Minginette, P., Mogo, S., Nieminen, T., Onnela, A., Pereira, P., Petäjä, T., Schnitzhofer, R., Seinfeld, J. H., Sipilä, M., Stozhkov, Y., Stratmann, F., Tomé, A., Vanhanen, J., Visanen, Y., Vrtala, A., Wagner, P. E., Walther, H., Weingartner, E., Wex, H., Winkler, P. M., Carslaw, K. S., Worsnop, D. R., Baltensperger, U., Kulmala, M., 2011, Role of sulphuric acid, ammonia and galactic cosmic rays in atmospheric aerosol nucleation, *Nature*, 476, 429–433
- Knoelker, M., Schuessler, M., 1988, Model calculations of magnetic flux tubes. IV - Convective energy transport and the nature of intermediate size flux concentrations, *A&A*, 202, 275–283
- Koldobskiy, S. A., Kähkönen, R., Hofer, B., Krivova, N. A., Kovaltsov, G. A., Usoskin, I. G., 2022, Time Lag Between Cosmic-Ray and Solar Variability: Sunspot Numbers and Open Solar Magnetic Flux, *Sol. Phys.*, 297, 38
- Komm, R., González Hernández, I., Howe, R., Hill, F., 2015, Subsurface Zonal and Meridional Flow Derived from GONG and SDO/HMI: A Comparison of Systematics, *Sol. Phys.*, 290, 1081–1104
- Komm, R., Howe, R., Hill, F., 2020, Solar-Cycle Variation of the Subsurface Flows of Active- and Quiet-Region Subsets, *Sol. Phys.*, 295, 47
- Komm, R. W., Howard, R. F., Harvey, J. W., 1993, Meridional Flow of Small Photospheric Magnetic Features, *Sol. Phys.*, 147, 207–223

- Kopp, G., 2014, An assessment of the solar irradiance record for climate studies, *Journal of Space Weather and Space Climate*, 4, A14
- Kopp, G., 2016, Magnitudes and timescales of total solar irradiance variability, *Journal of Space Weather and Space Climate*, 6, A30, [1606.05258](#)
- Kopp, G., Lawrence, G., Rottman, G., 2005, The Total Irradiance Monitor (TIM): Science Results, *Sol. Phys.*, 230, 129–139
- Kren, A. C., Pilewskie, P., Coddington, O., 2017, Where does Earth's atmosphere get its energy?, *Journal of Space Weather and Space Climate*, 7, A10
- Krivova, N. A., Solanki, S. K., 2004a, Effect of spatial resolution on estimating the Sun's magnetic flux, *A&A*, 417, 1125–1132
- Krivova, N. A., Solanki, S. K., 2004b, Effect of spatial resolution on estimating the Sun's magnetic flux, *A&A*, 417, 1125–1132
- Krivova, N. A., Solanki, S. K., Fligge, M., Unruh, Y. C., 2003, Reconstruction of solar irradiance variations in cycle 23: Is solar surface magnetism the cause?, *A&A*, 399, L1–L4
- Krivova, N. A., Balmaceda, L., Solanki, S. K., 2007, Reconstruction of solar total irradiance since 1700 from the surface magnetic flux, *A&A*, 467, 335–346
- Krivova, N. A., Vieira, L. E. A., Solanki, S. K., 2010, Reconstruction of solar spectral irradiance since the Maunder minimum, *J. Geophys. Res.*, 115, A12112
- Krivova, N. A., Solanki, S. K., Unruh, Y. C., 2011, Towards a long-term record of solar total and spectral irradiance, *Journal of Atmospheric and Solar-Terrestrial Physics*, 73, 223–234
- Krivova, N. A., Solanki, S. K., Hofer, B., Wu, C. J., Usoskin, I. G., Cameron, R., 2021, Modelling the evolution of the Sun's open and total magnetic flux, *A&A*, 650, A70, [2103.15603](#)
- Kulmala, M., Riipinen, I., Nieminen, T., Hulkkonen, M., Sogacheva, L., Manninen, H. E., Paasonen, P., Petäjä, T., Dal Maso, M., Aalto, P. P., Viljanen, A., Usoskin, I., Vainio, R., Mirme, S., Mirme, A., Minikin, A., Petzold, A., Hörrak, U., Plaß-Dülmer, C., Birmili, W., Kerminen, V. M., 2010, Atmospheric data over a solar cycle: no connection between galactic cosmic rays and new particle formation, *Atmospheric Chemistry & Physics*, 10, 1885–1898
- Laken, B., Wolfendale, A., Kniveton, D., 2009, Cosmic ray decreases and changes in the liquid water cloud fraction over the oceans, *Geophys. Res. Lett.*, 36, L23803
- Laken, B. A., Čalogović, J., 2013, Composite analysis with Monte Carlo methods: an example with cosmic rays and clouds, *Journal of Space Weather and Space Climate*, 3, A29, [1310.0266](#)

- Laken, B. A., Pallé, E., Čalogović, J., Dunne, E. M., 2012, A cosmic ray-climate link and cloud observations, *Journal of Space Weather and Space Climate*, 2, A18, [1211.5245](#)
- Lal, D., Peters, B., 1967, Cosmic Ray Produced Radioactivity on the Earth, *Handbuch der Physik*, 46, 551–612
- Le Mouél, J.-L., Lopes, F., Courtillot, V., 2017, Identification of Gleissberg Cycles and a Rising Trend in a 315-Year-Long Series of Sunspot Numbers, *Sol. Phys.*, 292, 43
- Legrand, J. P., Simon, P. A., 1981, Ten Cycles of Solar and Geomagnetic Activity, *Sol. Phys.*, 70, 173–195
- Leighton, R. B., 1964, Transport of Magnetic Fields on the Sun., *ApJ*, 140, 1547
- Li, J., 2018, A Systematic Study of Hale and Anti-Hale Sunspot Physical Parameters, *ApJ*, 867, 89, [1809.08980](#)
- Lites, B. W., Centeno, R., McIntosh, S. W., 2014, The solar cycle dependence of the weak internetwork flux, *PASJ*, 66, S4
- Livingston, W., 2002, Sunspots Observed to Physically Weaken in 2000-2001, *Sol. Phys.*, 207, 41–45
- Livingston, W. C., Harvey, J., Pierce, A. K., Schrage, D., Gillespie, B., Simmons, J., Slaughter, C., 1976, Kitt Peak 60-cm vacuum telescope, *Appl. Opt.*, 15, 33–39
- Lockwood, M., 2003, Twenty-three cycles of changing open solar magnetic flux, *Journal of Geophysical Research (Space Physics)*, 108, 1128
- Lockwood, M., Stamper, R., Wild, M. N., 1999, A doubling of the Sun's coronal magnetic field during the past 100 years, *Nature*, 399, 437–439
- Lockwood, M., Owens, M., Rouillard, A. P., 2009, Excess open solar magnetic flux from satellite data: 1. Analysis of the third perihelion Ulysses pass, *Journal of Geophysical Research (Space Physics)*, 114, A11103
- Lockwood, M., Nevanlinna, H., Barnard, L., Owens, M. J., Harrison, R. G., Rouillard, A. P., Scott, C. J., 2014a, Reconstruction of geomagnetic activity and near-earth interplanetary conditions over the past 167 yr - part 4: Near-earth solar wind speed, imf, and open solar flux, *Annal. Geophys.*, 32, 383–399
- Lockwood, M., Owens, M. J., Barnard, L., 2014b, Centennial variations in sunspot number, open solar flux, and streamer belt width: 2. Comparison with the geomagnetic data, *Journal of Geophysical Research (Space Physics)*, 119, 5183–5192
- Lockwood, M., Owens, M. J., Barnard, L. A., Scott, C. J., Frost, A. M., Yu, B., Chi, Y., 2022, Application of historic datasets to understanding open solar flux and the 20th-century grand solar maximum. 1. Geomagnetic, ionospheric, and sunspot observations, *Frontiers in Astronomy and Space Sciences*, 9, 960775

- Lodders, K., 2003, Solar System Abundances and Condensation Temperatures of the Elements, *ApJ*, 591, 1220–1247
- Mackay, D. H., Priest, E. R., Lockwood, M., 2002, The Evolution of the Sun's Open Magnetic Flux - II. Full Solar Cycle Simulations, *Sol. Phys.*, 209, 287–309
- Mandal, S., Krivova, N. A., Solanki, S. K., Sinha, N., Banerjee, D., 2020, Sunspot area catalog revisited: Daily cross-calibrated areas since 1874, *A&A*, 640, A78, [2004.14618](#)
- Marsh, N. D., Svensmark, H., 2000, Low Cloud Properties Influenced by Cosmic Rays, *Phys. Rev. Lett.*, 85, 5004–5007, [physics/0005072](#)
- Mathew, S. K., Martínez Pillet, V., Solanki, S. K., Krivova, N. A., 2007, Properties of sunspots in cycle 23. I. Dependence of brightness on sunspot size and cycle phase, *A&A*, 465, 291–304, [astro-ph/0701401](#)
- Mayaud, P.-N., 1972, The aa indices: A 100-year series characterizing the magnetic activity, *J. Geophys. Res.*, 77, 6870
- McIntosh, P. S., 1981, The Physics of Sunspots, in Sacramento Peak National Observatory, (Eds.) L. E. Cram, J. H. Thomas, pp. 7–54
- McIntosh, S. W., Wang, X., Leamon, R. J., Davey, A. R., Howe, R., Krista, L. D., Malanushenko, A. V., Markel, R. S., Cirtain, J. W., Gurman, J. B., Pesnell, W. D., Thompson, M. J., 2014, Deciphering Solar Magnetic Activity. I. On the Relationship between the Sunspot Cycle and the Evolution of Small Magnetic Features, *ApJ*, 792, 12, [1403.3071](#)
- Mikhailov, A., 1955, The Pulkovo Observatory, *The Observatory*, 75, 28–32
- Miyahara, H., Masuda, K., Muraki, Y., Furuzawa, H., Menjo, H., Nakamura, T., 2004, Cyclicity of Solar Activity During the Maunder Minimum Deduced from Radiocarbon Content, *Sol. Phys.*, 224, 317–322
- Moraal, H., Stoker, P. H., 2010, Long-term neutron monitor observations and the 2009 cosmic ray maximum, *Journal of Geophysical Research (Space Physics)*, 115, A12109
- Muñoz-Jaramillo, A., Navarrete, B., Campusano, L. E., 2021, Solar Anti-Hale Bipolar Magnetic Regions: A Distinct Population with Systematic Properties, *ApJ*, 920, 31, [2203.11898](#)
- Nagovitsyn, Y. A., Makarova, V. V., Nagovitsyna, E. Y., 2007, Series of classical solar activity indices: Kislovodsk data, *Solar System Research*, 41, 81–86
- Nèmec, N. E., Shapiro, A. I., Işık, E., Sowmya, K., Solanki, S. K., Krivova, N. A., Cameron, R. H., Gizon, L., 2022, Faculae cancel out on the surfaces of active Suns, arXiv e-prints, arXiv:2207.06816, [2207.06816](#)
- Owens, M. J., Crooker, N. U., 2006, Coronal mass ejections and magnetic flux buildup in the heliosphere, *Journal of Geophysical Research (Space Physics)*, 111, A10104

- Owens, M. J., Usoskin, I., Lockwood, M., 2012, Heliospheric modulation of galactic cosmic rays during grand solar minima: Past and future variations, *Geophys. Res. Lett.*, 39, L19102
- Owens, M. J., Lockwood, M., Riley, P., Linker, J., 2017, Sunward Strahl: A Method to Unambiguously Determine Open Solar Flux from In Situ Spacecraft Measurements Using Suprathermal Electron Data, *Journal of Geophysical Research (Space Physics)*, 122, 10,980–10,989
- Paillard, D., 2001, Glacial cycles: Toward a new paradigm, *Reviews of Geophysics*, 39, 325–346
- Parker, E. N., 1955, Hydromagnetic Dynamo Models., *ApJ*, 122, 293
- Parker, E. N., 1972, Topological Dissipation and the Small-Scale Fields in Turbulent Gases, *ApJ*, 174, 499
- Parker, E. N., 1979, Sunspots and the physics of magnetic flux tubes. IX. Umbral dots and longitudinal overstability., *ApJ*, 234, 333–347
- Parker, E. N., 1983, Magnetic Neutral Sheets in Evolving Fields - Part Two - Formation of the Solar Corona, *ApJ*, 264, 642
- Parnell, C. E., DeForest, C. E., Hagenaar, H. J., Johnston, B. A., Lamb, D. A., Welsch, B. T., 2009, A power-law distribution of solar magnetic fields over more than five decades in flux, *The Astrophysical Journal*, 698, 75–82
- Petrovay, K., 2020, Solar cycle prediction, *Living Reviews in Solar Physics*, 17, 2, [1907.02107](#)
- Petrovay, K., Nagy, M., Yeates, A. R., 2020, Towards an algebraic method of solar cycle prediction. I. Calculating the ultimate dipole contributions of individual active regions, *Journal of Space Weather and Space Climate*, 10, 50, [2009.02299](#)
- Pierce, J. R., Adams, P. J., 2009, Can cosmic rays affect cloud condensation nuclei by altering new particle formation rates?, *Geophys. Res. Lett.*, 36, L09820
- Pontin, D. I., Hornig, G., 2020, The Parker problem: existence of smooth force-free fields and coronal heating, *Living Reviews in Solar Physics*, 17, 5
- Priest, E. R., 2003, Solar magnetohydrodynamics, in *Dynamic Sun*, (Eds.) B. N. Dwivedi, F. b. E. N. Parker, pp. 217–237
- Pulkkinen, T., 2007, *Space Weather: Terrestrial Perspective*, *Living Reviews in Solar Physics*, 4, 1
- Radick, R. R., Lockwood, G. W., Henry, G. W., Hall, J. C., Pevtsov, A. A., 2018, Patterns of Variation for the Sun and Sun-like Stars, *ApJ*, 855, 75

- Reimer, P. J., Bard, E., Bayliss, A., Beck, J. W., Blackwell, P. G., Ramsey, C. B., Buck, C. E., Cheng, H., Edwards, R. L., Friedrich, M., Grootes, P. M., Guilderson, T. P., Haffidason, H., Hajdas, I., Hatte, C., Heaton, T. J., Hoffmann, D. L., Hogg, A. G., Hughen, K. A., Kaiser, K. F., Kromer, B., Manning, S. W., Niu, M., Reimer, R. W., Richards, D. A., Scott, E. M., Southon, J. R., Staff, R. A., Turney, C. S. M., van der Plicht, J., 2013, Intcal13 and marine13 radiocarbon age calibration curves 0-50000 years cal bp, *Radiocarbon*, 55, 1869–1887, ISSN 0033-8222
- Reinhold, T., Shapiro, A. I., Solanki, S. K., Montet, B. T., Krivova, N. A., Cameron, R. H., Amazo-Gómez, E. M., 2020, The Sun is less active than other solar-like stars, *Science*, 368, 518–521, [2005.01401](#)
- Rempel, M., 2014, Numerical Simulations of Quiet Sun Magnetism: On the Contribution from a Small-scale Dynamo, *ApJ*, 789, 132, [1405.6814](#)
- Rightmire-Upton, L., Hathaway, D. H., Kosak, K., 2012, Measurements of the Sun's High-latitude Meridional Circulation, *ApJ*, 761, L14, [1211.0944](#)
- Riley, P., Ben-Nun, M., Linker, J. A., Mikic, Z., Svalgaard, L., Harvey, J., Bertello, L., Hoeksema, T., Liu, Y., Ulrich, R., 2014, A Multi-Observatory Inter-Comparison of Line-of-Sight Synoptic Solar Magnetograms, *Sol. Phys.*, 289, 769–792
- Riley, P., Lionello, R., Linker, J. A., Cliver, E., Balogh, A., Beer, J., Charbonneau, P., Crooker, N., DeRosa, M., Lockwood, M., Owens, M., McCracken, K., Usoskin, I., Koutchmy, S., 2015, Inferring the Structure of the Solar Corona and Inner Heliosphere During the Maunder Minimum Using Global Thermodynamic Magnetohydrodynamic Simulations, *ApJ*, 802, 105
- Rincon, F., Rieutord, M., 2018, The Sun's supergranulation, *Living Reviews in Solar Physics*, 15, 6
- Saha, C., Chandra, S., Nandy, D., 2022, Evidence of persistence of weak magnetic cycles driven by meridional plasma flows during solar grand minima phases, *MNRAS*, 517, L36–L40, [2209.14651](#)
- Schatten, K. H., Wilcox, J. M., Ness, N. F., 1969, A model of interplanetary and coronal magnetic fields, *Sol. Phys.*, 6, 442–455
- Scherrer, P. H., Wilcox, J. M., Svalgaard, L., Duvall, T. L., J., Dittmer, P. H., Gustafson, E. K., 1977, The mean magnetic field of the Sun: observations at Stanford., *Sol. Phys.*, 54, 353–361
- Scherrer, P. H., Bogart, R. S., Bush, R. I., Hoeksema, J. T., Kosovichev, A. G., Schou, J., Rosenberg, W., Springer, L., Tarbell, T. D., Title, A., Wolfson, C. J., Zayer, I., MDI Engineering Team, 1995, The Solar Oscillations Investigation - Michelson Doppler Imager, *Sol. Phys.*, 162, 129–188
- Schmutz, W., Fehlmann, A., Finsterle, W., Kopp, G., Thuillier, G., 2013, Total solar irradiance measurements with PREMOS/PICARD, in *Radiation Processes in the Atmosphere and Ocean (IRS2012)*, vol. 1531 of American Institute of Physics Conference Series, pp. 624–627

- Schou, J., Scherrer, P. H., Bush, R. I., Wachter, R., Couvidat, S., Rabello-Soares, M. C., Bogart, R. S., Hoeksema, J. T., Liu, Y., Duvall, T. L., Akin, D. J., Allard, B. A., Miles, J. W., Rairden, R., Shine, R. A., Tarbell, T. D., Title, A. M., Wolfson, C. J., Elmore, D. F., Norton, A. A., Tomczyk, S., 2012, Design and Ground Calibration of the Helioseismic and Magnetic Imager (HMI) Instrument on the Solar Dynamics Observatory (SDO), *Sol. Phys.*, 275, 229–259
- Schrijver, C. J., 2001, Simulations of the Photospheric Magnetic Activity and Outer Atmospheric Radiative Losses of Cool Stars Based on Characteristics of the Solar Magnetic Field, *ApJ*, 547, 475–490
- Schrijver, C. J., Harvey, K. L., 1989, The Distribution of Solar Magnetic Fluxes and the Nonlinearity of Stellar Flux-Flux Relations, *ApJ*, 343, 481
- Schrijver, C. J., Harvey, K. L., 1994, The Photospheric Magnetic Flux Budget, *Sol. Phys.*, 150, 1
- Schrijver, C. J., Zwaan, C., 2000, *Solar and Stellar Magnetic Activity*, Cambridge Univ. Press
- Schrijver, C. J., Shine, R. A., Hagenaar, H. J., Hurlburt, N. E., Title, A. M., Strous, L. H., Jefferies, S. M., Jones, A. R., Harvey, J. W., Duvall, Thomas L., J., 1996, Dynamics of the Chromospheric Network: Mobility, Dispersal, and Diffusion Coefficients, *ApJ*, 468, 921
- Schrijver, C. J., De Rosa, M. L., Title, A. M., 2002, What Is Missing from Our Understanding of Long-Term Solar and Heliospheric Activity?, *ApJ*, 577, 1006–1012
- Schunker, H., Baumgartner, C., Birch, A. C., Cameron, R. H., Braun, D. C., Gizon, L., 2020, Average motion of emerging solar active region polarities. II. Joy's law, *A&A*, 640, A116, [2006.05565](#)
- Schüssler, M., Baumann, I., 2006, Modeling the Sun's open magnetic flux, *A&A*, 459, 945–953
- Schwabe, H., 1844, *Sonnenbeobachtungen im Jahre 1843. Von Herrn Hofrath Schwabe in Dessau*, *Astronomische Nachrichten*, 21, 233
- Sheeley, N. R., J., DeVore, C. R., Boris, J. P., 1985, Simulations of the Mean Solar Magnetic Field during Sunspot CYCLE-21, *Sol. Phys.*, 98, 219–239
- Simpson, J. A., 2000, The Cosmic Ray Nucleonic Component: The Invention and Scientific Uses of the Neutron Monitor - (Keynote Lecture), *Space Sci. Rev.*, 93, 11–32
- Sivaraman, K. R., Gupta, S. S., Howard, R. F., 1993, Measurement of Kodiakanal White-Light Images - Part One, *Sol. Phys.*, 146, 27–47
- Snodgrass, H. B., 1983, Magnetic rotation of the solar photosphere, *ApJ*, 270, 288–299
- Sokoloff, D., 2004, The Maunder Minimum and the Solar Dynamo, *Sol. Phys.*, 224, 145–152

- Solanki, S. K., 2003, Sunspots: An overview, *A&A Rev.*, 11, 153–286
- Solanki, S. K., Schüssler, M., Fligge, M., 2000, Evolution of the Sun's large-scale magnetic field since the Maunder minimum, *Nature*, 408, 445–447
- Solanki, S. K., Schüssler, M., Fligge, M., 2002, Secular variation of the Sun's magnetic flux, *A&A*, 383, 706–712
- Solanki, S. K., Usoskin, I. G., Kromer, B., Schüssler, M., Beer, J., 2004, Unusual activity of the Sun during recent decades compared to the previous 11,000 years, *Nature*, 431, 1084–1087
- Solanki, S. K., Wenzler, T., Schmitt, D., 2008, Moments of the latitudinal dependence of the sunspot cycle: a new diagnostic of dynamo models, *A&A*, 483, 623–632
- Solanki, S. K., Krivova, N. A., Haigh, J. D., 2013, Solar Irradiance Variability and Climate, *ARA&A*, 51, 311–351, [1306.2770](#)
- Spörer, F. W. G., 1879, Beobachtung der Sonnenflecken etc., *Astronomische Nachrichten*, 96, 23
- Spruit, H. C., 1976, Pressure equilibrium and energy balance of small photospheric flux-tubes., *Sol. Phys.*, 50, 269–295
- Steinhilber, F., Abreu, J. A., Beer, J., Brunner, I., Christl, M., Fischer, H., Heikkilä, U., Kubik, P. W., Mann, M., McCracken, K. G., Miller, H., Miyahara, H., Oerter, H., Wilhelms, F., 2012, 9,400 years of cosmic radiation and solar activity from ice cores and tree rings, *Proceedings of the National Academy of Science*, 109, 5967–5971
- Stenflo, J. O., Kosovichev, A. G., 2012, Bipolar Magnetic Regions on the Sun: Global Analysis of the SOHO/MDI Data Set, *ApJ*, 745, 129, [1112.5226](#)
- Stuiver, M., Quay, P. D., 1980, Changes in Atmospheric Carbon-14 Attributed to a Variable Sun, *Science*, 207, 11–19
- Suess, H. E., 1955, Radiocarbon Concentration in Modern Wood, *Science*, 122, 415–417
- Suess, H. E., 1980, The radiocarbon record in tree rings of the last 8000 years, *Radiocarbon*, 22, 200–209
- Svalgaard, L., Schatten, K. H., 2016, Reconstruction of the Sunspot Group Number: The Backbone Method, *Sol. Phys.*, 291, 2653–2684, [1506.00755](#)
- Svalgaard, L., Duvall, T. L., Jr., Scherrer, P. H., 1978, The strength of the Sun's polar fields., *Sol. Phys.*, 58, 225–239
- Svensmark, H., Friis-Christensen, E., 1997, Variation of cosmic ray flux and global cloud coverage—a missing link in solar-climate relationships, *Journal of Atmospheric and Solar-Terrestrial Physics*, 59, 1225–1232

- Svensmark, H., Enghoff, M. B., Shaviv, N. J., Svensmark, J., 2017, Increased ionization supports growth of aerosols into cloud condensation nuclei, *Nature Communications*, 8, 2199
- Svensmark, J., Enghoff, M. B., Shaviv, N. J., Svensmark, H., 2016, The response of clouds and aerosols to cosmic ray decreases, *Journal of Geophysical Research (Space Physics)*, 121, 8152–8181
- Temmer, M., 2021, Space weather: the solar perspective, *Living Reviews in Solar Physics*, 18, 4, [2104.04261](#)
- Thornton, L. M., Parnell, C. E., 2011, Small-scale flux emergence observed using hinode/sot, *Sol. Phys.*, 269, 13–40
- Tlatov, A. G., Vasil'eva, V. V., Pevtsov, A. A., 2010, Distribution of Magnetic Bipoles on the Sun over Three Solar Cycles, *ApJ*, 717, 357–362
- Ulrich, R. K., 2010, Solar Meridional Circulation from Doppler Shifts of the Fe I Line at 5250 Å as Measured by the 150-foot Solar Tower Telescope at the Mt. Wilson Observatory, *ApJ*, 725, 658–669, [1010.0487](#)
- Upton, L., Hathaway, D. H., 2014, Predicting the Sun's Polar Magnetic Fields with a Surface Flux Transport Model, *ApJ*, 780, 5, [1311.0844](#)
- Usoskin, I., Kovaltsov, G., Kiviaho, W., 2021a, Robustness of Solar-Cycle Empirical Rules Across Different Series Including an Updated Active-Day Fraction (ADF) Sunspot Group Series, *Sol. Phys.*, 296, 13, [2012.08415](#)
- Usoskin, I. G., 2017, A history of solar activity over millennia, *Living Reviews in Solar Physics*, 14, 3
- Usoskin, I. G., Mursula, K., Kovaltsov, G. A., 2001, Heliospheric modulation of cosmic rays and solar activity during the Maunder minimum, *J. Geophys. Res.*, 106, 16039–16046
- Usoskin, I. G., Mursula, K., Solanki, S. K., Schüssler, M., Kovaltsov, G. A., 2002, A physical reconstruction of cosmic ray intensity since 1610, *J. Geophys. Res.*, 107, 1374
- Usoskin, I. G., Solanki, S. K., Schüssler, M., Mursula, K., Alanko, K., 2003, Millennium-Scale Sunspot Number Reconstruction: Evidence for an Unusually Active Sun since the 1940s, *Phys. Rev. Lett.*, 91, 211101
- Usoskin, I. G., Mursula, K., Solanki, S., Schüssler, M., Alanko, K., 2004, Reconstruction of solar activity for the last millennium using  $^{10}\text{Be}$  data, *A&A*, 413, 745–751
- Usoskin, I. G., Solanki, S. K., Kovaltsov, G. A., 2007, Grand minima and maxima of solar activity: new observational constraints, *A&A*, 471, 301–309, [0706.0385](#)
- Usoskin, I. G., Gallet, Y., Lopes, F., Kovaltsov, G. A., Hulot, G., 2016a, Solar activity during the Holocene: the Hallstatt cycle and its consequence for grand minima and maxima, *A&A*, 587, A150, [1602.02483](#)

- Usoskin, I. G., Gallet, Y., Lopes, F., Kovaltsov, G. A., Hulot, G., 2016b, Solar activity during the Holocene: the Hallstatt cycle and its consequence for grand minima and maxim, *Astron. Astrophys.*, 587, A150
- Usoskin, I. G., Kovaltsov, G. A., Lockwood, M., Mursula, K., Owens, M., Solanki, S. K., 2016c, A New Calibrated Sunspot Group Series Since 1749: Statistics of Active Day Fractions, *Sol. Phys.*, 291, 2685–2708, [1512.06421](#)
- Usoskin, I. G., Solanki, S. K., Krivova, N. A., Hofer, B., Kovaltsov, G. A., Wacker, L., Brehm, N., Kromer, B., 2021b, Solar cyclic activity over the last millennium reconstructed from annual  $^{14}\text{C}$  data, *A&A*, 649, A141, [2103.15112](#)
- Väisänen, P., Usoskin, I., Mursula, K., 2021, Seven Decades of Neutron Monitors (1951–2019): Overview and Evaluation of Data Sources, *Journal of Geophysical Research (Space Physics)*, 126, e28941
- van Ballegooijen, A. A., Cartledge, N. P., Priest, E. R., 1998, Magnetic Flux Transport and the Formation of Filament Channels on the Sun, *ApJ*, 501, 866–881
- van Ballegooijen, A. A., Asgari-Targhi, M., Cranmer, S. R., DeLuca, E. E., 2011, Heating of the Solar Chromosphere and Corona by Alfvén Wave Turbulence, *ApJ*, 736, 3, [1105.0402](#)
- Van Doorselaere, T., Srivastava, A. K., Antolin, P., Magyar, N., Vasheghani Farahani, S., Tian, H., Kolotkov, D., Ofman, L., Guo, M., Arregui, I., De Moortel, I., Pascoe, D., 2020, Coronal Heating by MHD Waves, *Space Sci. Rev.*, 216, 140, [2012.01371](#)
- van Driel-Gesztelyi, L., Green, L. M., 2015, Evolution of Active Regions, *Living Reviews in Solar Physics*, 12, 1
- Vaquero, J. M., Kovaltsov, G. A., Usoskin, I. G., Carrasco, V. M. S., Gallego, M. C., 2015, Level and length of cyclic solar activity during the Maunder minimum as deduced from the active-day statistics, *A&A*, 577, A71
- Vázquez, M., Vaquero, J. M., Gallego, M. C., Roca Cortés, T., Pallé, P. L., 2016, Long-Term Trends and Gleissberg Cycles in Aurora Borealis Records (1600 - 2015), *Sol. Phys.*, 291, 613–642
- Vernazza, J. E., Avrett, E. H., Loeser, R., 1981, Structure of the solar chromosphere. III. Models of the EUV brightness components of the quiet sun., *ApJS*, 45, 635–725
- Vieira, L. E. A., Solanki, S. K., 2010, Evolution of the solar magnetic flux on time scales of years to millenia, *A&A*, 509, A100
- Vieira, L. E. A., Solanki, S. K., Krivova, N. A., Usoskin, I., 2011, Evolution of the solar irradiance during the Holocene, *A&A*, 531, A6, [1103.4958](#)
- Virtanen, I. O. I., Virtanen, I. I., Pevtsov, A. A., Bertello, L., Yeates, A., Mursula, K., 2019, Reconstructing solar magnetic fields from historical observations. IV. Testing the reconstruction method, *A&A*, 627, A11

- Voegler, A., Schuessler, M., 2007, A solar surface dynamo, *A&A*, 465, L43–L46, [astro-ph/0702681](#)
- Vonmoos, M., Beer, J., Muscheler, R., 2006, Large variations in Holocene solar activity: Constraints from  $^{10}\text{Be}$  in the Greenland Ice Core Project ice core, *Journal of Geophysical Research (Space Physics)*, 111, A10105
- Wagner, G., Beer, J., Masarik, J., Muscheler, R., Kubik, P. W., Mende, W., Laj, C., Raisbeck, G. M., Yiou, F., 2001, Presence of the Solar de Vries Cycle ( $\sim 205$  years) during the Last Ice Age, *Geophys. Res. Lett.*, 28, 303–306
- Waldmeier, M., 1935, Neue Eigenschaften der Sonnenfleckenkurve, *Astronomische Mitteilungen der Eidgenössischen Sternwarte Zurich*, 14, 105–136
- Waldmeier, M., 1939, Die Zonenwanderung der Sonnenflecken, *Astronomische Mitteilungen der Eidgenössischen Sternwarte Zurich*, 14, 470–481
- Wang, Y. M., 2017, Surface Flux Transport and the Evolution of the Sun's Polar Fields, *Space Sci. Rev.*, 210, 351–365
- Wang, Y. M., Nash, A. G., Sheeley, N. R., J., 1989, Magnetic Flux Transport on the Sun, *Science*, 245, 712–718
- Wang, Y. M., Lean, J. L., Sheeley, N. R., J., 2005, Modeling the Sun's Magnetic Field and Irradiance since 1713, *ApJ*, 625, 522–538
- Wang, Y. M., Colaninno, R. C., Baranyi, T., Li, J., 2015, Active-region Tilt Angles: Magnetic versus White-light Determinations of Joy's Law, *ApJ*, 798, 50, [1412.2329](#)
- Wenzler, T., Solanki, S. K., Krivova, N. A., Fröhlich, C., 2006, Reconstruction of solar irradiance variations in cycles 21–23 based on surface magnetic fields, *A&A*, 460, 583–595
- Willamo, T., Usoskin, I. G., Kovaltsov, G. A., 2017, Updated sunspot group number reconstruction for 1749–1996 using the active day fraction method, *A&A*, 601, A109, [1705.05109](#)
- Willson, R. C., Mordvinov, A. V., 2003, Secular total solar irradiance trend during solar cycles 21–23, *Geophys. Res. Lett.*, 30, 1199
- Willson, R. C., Gulkis, S., Janssen, M., Hudson, H. S., Chapman, G. A., 1981, Observations of Solar Irradiance Variability, *Science*, 211, 700–702
- Wilson, P. R., Altrocki, R. C., Harvey, K. L., Martin, S. F., Snodgrass, H. B., 1988, The extended solar activity cycle, *Nature*, 333, 748–750
- Wolf, R., 1850, *Astronomische Mitteilungen der Eidgenössischen Sternwarte Zurich*, vol. 1
- Wu, C.-J., Krivova, N. A., Solanki, S. K., Usoskin, I. G., 2018a, Solar total and spectral irradiance reconstruction over the last 9000 years, *A&A*, 620, A120

- Wu, C. J., Usoskin, I. G., Krivova, N., Kovaltsov, G. A., Baroni, M., Bard, E., Solanki, S. K., 2018b, Solar activity over nine millennia: A consistent multi-proxy reconstruction, *A&A*, 615, A93
- Yeates, A. R., 2020, How Good Is the Bipolar Approximation of Active Regions for Surface Flux Transport?, *Sol. Phys.*, 295, 119, [2008.03203](#)
- Yeo, K. L., Krivova, N. A., Solanki, S. K., Glassmeier, K. H., 2014, Reconstruction of total and spectral solar irradiance from 1974 to 2013 based on KPVT, SoHO/MDI, and SDO/HMI observations, *A&A*, 570, A85, [1408.1229](#)
- Yeo, K. L., Solanki, S. K., Krivova, N. A., Rempel, M., Anusha, L. S., Shapiro, A. I., Tagirov, R. V., Witzke, V., 2020, The Dimmest State of the Sun, *Geophys. Res. Lett.*, 47, e90243
- Zacharias, P., 2014, An Independent Review of Existing Total Solar Irradiance Records, *Surveys in Geophysics*, 35, 897–912
- Zhang, L. Y., Wang, H. N., Du, Z. L., Cui, Y. M., He, H., 2007, Long-term behavior of active longitudes for solar X-ray flares, *A&A*, 471, 711–716
- Zhao, X., Hoeksema, J. T., 1995a, Predicting the heliospheric magnetic field using the current sheet-source surface model, *Advances in Space Research*, 16, 181–184
- Zhao, X., Hoeksema, J. T., 1995b, Prediction of the interplanetary magnetic field strength., *J. Geophys. Res.*, 100, 19–33
- Zwaan, C., 1978, On the Appearance of Magnetic Flux in the Solar Photosphere, *Sol. Phys.*, 60, 213–240





# Scientific contributions

## Refereed publications

- Krivova, N. A., Solanki, S. K., **Hofer, B.**, Wu, C. J., Usoskin, I. G., Cameron, R., 2021, "Modelling the evolution of the Sun's open and total magnetic flux", in *Astronomy & Astrophysics*, 650, A70
- Usoskin, I. G., Solanki, S. K., Krivova, N. A., **Hofer, B.**, Kovaltsov, G. A., Wacker, L., Brehm, N., Kromer, B., 2021, "Solar cyclic activity over the last millennium reconstructed from annual 14C data", in *Astronomy & Astrophysics*, 649, A141
- Koldobskiy, S. A., Kähkönen, R., **Hofer, B.**, Krivova, N. A., Kovaltsov, G. A., Usoskin, I. G., 2022, "Time Lag Between Cosmic-Ray and Solar Variability: Sunspot Numbers and Open Solar Magnetic Flux", in *Solar Physics*, 297, 38

## Submitted

- **Hofer, B.**, Krivova, N. A., Cameron, R., Solanki, S. K., Jiang, J., 2022, "The influence of small bipolar magnetic regions on basic solar quantities", submitted to *Astronomy & Astrophysics*

## Conference contributions

- 22nd EGU General Assembly, held online, 4-8 May 2020  
Poster: *Towards a more reliable reconstruction of the historical solar variability: a more realistic description of solar ephemeral magnetic regions*
- vEGU21 the 23rd EGU General Assembly, held online, 19-30 April 2021  
Poster: *Accounting for small bipolar magnetic regions in solar irradiance reconstructions*
- European Solar Physics Meeting 16, held online, 6 - 10 September 2021  
Poster & Talk: *Including ephemeral regions in surface flux transport simulations and solar irradiance reconstructions*
- Space Climate Symposium 8, Krakow, Poland, 19-22 September 2022  
Poster: *Influence of small magnetic regions on the solar magnetic field*



# Acknowledgements

First and foremost, I want to thank my supervisor Natalie Krivova for your guidance and support during my time here in Göttingen. Whenever I had a problem, whether it was related to my PhD or something else, you did your best to help me. Especially during the pandemic that took a toll on all of us, you kept encouraging me when I was struggling mentally and with my motivation. I am glad that I had you as my supervisor.

Many thanks go to my TAC members Sami Solanki and Stefan Dreizler for your valuable feedback to improve my work. I also want to thank Hardi Peter, Wolfram Kollatschny and Ariane Frey for being part of my examination board. Special thanks go to IMPRS coordinator Sonja Schuh, who helped me getting through all the administrative hurdles and regulations of my PhD and Robert Cameron for the many discussions and advice with the SFTM.

Of course, my time in Göttingen would not have been the same without all my old and new friends that accompanied me during my PhD and helped me keep my sanity. Firstly, I want to thank my fellow Austrians Bastian, Christian and Stephan for our engaging and often hilarious lunchtime discussions and our enjoyable board game evenings. Also, I want to thank Cosima, Aline, Tanayveer, Pablo and Paul for being part of our DnD group and for foiling all of my carefully crafted plans. Thank you Nina for all our entertaining chats and thank you Yara for turning the stressful final phase of my PhD into a bright one. Finally, I want to thank all of the other students and postdocs who helped make this institute such a lively place. I really enjoyed all the joint events and parties and I thank you for giving me such a warm welcome during the start of my PhD.

Von tiefstem Herzen möchte ich meinen Eltern Roswitha und Ernst, meinem Bruder Thomas und meiner verstorbenen Großmutter Maria danken, die mir mit ihrer Liebe und Unterstützung stets zur Seite standen und mich zu dem Menschen gemacht haben, der ich heute bin. Ich weiß, wie schwierig es für euch war, mich ziehen zu lassen und ich bin froh, dass ich dennoch so viele schöne Momente mit euch teilen konnte. Ohne euch wäre ich nie so weit gekommen.

I want to thank for the financial support by the International Max Planck Research School for Solar System Science (IMPRS) at the University of Göttingen and the Max Planck Institute for Solar System Research (MPS) during my PhD.



# Curriculum vitae

## Personal data

Name	Bernhard Hofer
Year of Birth	1992
Place of Birth	Graz, Austria
Nationality	Austria

## Education

Jan. 2019 - Nov. 2022	PhD student at the International Max Planck Research School at the University of Göttingen and the Max Planck Institute for Solar System Research, Göttingen, Germany
Thesis	<i>Modelling the evolution of small bipolar regions on the Sun</i>
Advisors	Dr. Natalie Krivova, Prof. Dr. Sami K. Solanki, Prof. Dr. Stefan Dreizler
Jan. 2016 - Oct. 2018	M.Sc. in Astrophysics at the Karl-Franzens University and the Space Research Institute of the Austrian Academy of Sciences, Graz, Austria
Thesis	<i>Electromotive force deduced from Helios observations during Coronal Mass Ejections</i>
Advisors	Doz. Dr. Yasuhito Narita, Dr. Philippe Bourdin
Jul. 2012 - Dec. 2015	B.Sc. in Astrophysics at the Karl-Franzens University, Graz, Austria
Thesis	<i>Gravitationslinseneffekt (engl.: "Gravitational lensing")</i>
Advisors	Prof. Dr. Arnold Hanslmeier